

# Correlation Function of Ultrahigh-Energy Cosmic Rays Favors Point Sources<sup>1</sup>

P. G. Tinyakov<sup>1,3</sup> and I. I. Tkachev<sup>2,3</sup>

<sup>1</sup> *Institute of Theoretical Physics, University of Lausanne, CH-1015 Lausanne, Switzerland*

<sup>2</sup> *CERN Theory Division, CH-1211 Geneva 23, Switzerland*

<sup>3</sup> *Institute for Nuclear Research, Russian Academy of Sciences, Moscow, 117312 Russia*

Received May 18, 2001

We calculate the angular two-point correlation function of ultrahigh-energy cosmic rays (UHECR) observed in the AGASA and Yakutsk experiments. In both data sets, there is a strong signal at the highest energies, which is concentrated in the first bin of size equal to the angular resolution of the experiment. For the uniform distribution of sources, the probability of chance clustering is  $4 \times 10^{-6}$ . Correlations are absent or insignificant at larger angles. This favors the models with compact sources of UHECR. © 2001 MAIK “Nauka/Interperiodica”.

PACS numbers: 98.70.Sa

1. The measurements of the flux of ultrahigh-energy cosmic rays (UHECR) at energies of order  $10^{20}$  eV [1] provide compelling evidence of the absence of the Greisen–Zatsepin–Kuzmin (GZK) cutoff [2]. The resolution of this puzzle seems to be impossible without invoking new physics or extreme astrophysics. All models suggested so far can be classified in three groups, according to the way the GZK cutoff is avoided: (i) “nearby source,” (ii) weak interaction with CMB, and (iii) bump in the injection spectrum.

The possibility (i) assumes that a substantial fraction of the observed UHECR comes from a relatively nearby source(s) and thus is not subject to the GZK cutoff. This idea may be realized in different ways, examples being the models of decaying superheavy dark matter [3] or models in which UHECR emitted by nearby source(s) propagate diffusively in the galactic [4] or extragalactic [5] magnetic fields. Although models of this type generically predict large-scale anisotropy [5, 6], they might still work.

In the option (ii), the GZK cutoff is eliminated (or shifted to higher energies) by assuming weak or non-standard interaction of primary particles with the cosmic microwave background. This may happen, for instance, if primary particles are neutrinos [7], hypothetical light SUSY hadrons [8], or if the Lorentz invariance is violated at high energies [9]. The possibility (iii) can be realized in models which involve topo-

logical defects [10] or in some models where primary particles are neutrinos [11].

Existing data hint also at another important feature of UHECR, namely, the clustering at small angles [12]. The AGASA collaboration has reported three doublets and one triplet out of 47 events with energies  $E > 4 \times 10^{19}$  eV with chance probability of less than 1% in the case of the isotropic distribution [13]. The world data set has also been analyzed; 6 doublets and 2 triplets out of 92 events with energies  $E > 4 \times 10^{19}$  eV were found [14] with the chance probability less than 1%.

If not a statistical fluctuation, what does the clustering imply for models of UHECR? There are two possible situations: either clustering is due to the existence of pointlike sources, or it is a result of variations in the flux of UHECR over the sky (the regions of higher flux are more likely to produce clusters of events [15]). In the first case, the models which involve the diffuse propagation of UHECR are excluded. This case also implies that there is no defocusing of UHECR in the magnetic fields during their propagation. Such defocusing occurs even in a regular (e.g., galactic) magnetic field, since different events in a cluster have different energies. Thus, one can put bounds on the charge of the primary particles. For the extragalactic rays, knowing that primary particles are charged would imply direct bounds on the extragalactic magnetic fields.

In the second case, the regions of higher flux may reflect higher density of sources, as in the models of superheavy dark matter, where they would correspond to dark matter clumps in the halo. Alternatively, they

<sup>1</sup> This article was submitted by the authors in English.

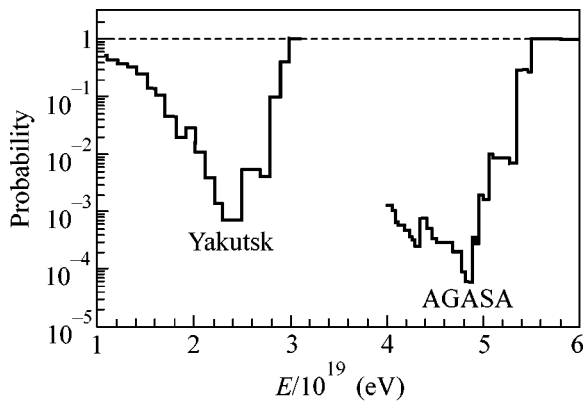


**Fig. 1.** Probability to match or exceed the observed count in the first bin vs. energy for the random distribution of arrival directions.

may be due to the effects of propagation such as defocusing in magnetic fields or magnetic lensing [16].

In order to determine which of these two cases fits the present experimental data better, it is not enough to know the probability to have a certain number of clusters. In this respect, previous analyses [12–14] are not sufficient. One has to find the angular correlation function. This is the approach we accept in this paper.

2. The two-point correlation function for a given set of events is defined as follows. For each event, we divide the sphere into concentric rings (bins) with fixed angular size (say, the angular resolution of the experiment). We count the number of events falling into each bin, sum over all events, and divide by 2 to avoid double counting, thus obtaining the numbers  $N_i$ . We repeat the same procedure for a large number (typically  $10^5$ ) of randomly generated sets and calculate the mean Monte-Carlo value  $N_i^{MC}$  and the variance  $\sigma_i^{MC}$  for each bin in a standard way. The correlation function can be defined as  $f_i = N_i/N_i^{MC} - 1$ . A deviation of  $f_i$  from zero indicates the presence of the correlations on the angular scale corresponding to the  $i$ th bin.

The correlation function  $f_i$  fluctuates. In order to see whether its deviation from zero is statistically significant, we define the ratio  $r_i = (N_i - N_i^{MC})/\sigma_i^{MC}$ , which shows the excess in the correlation function, as compared to the random distribution in the units of variance. With enough statistics, this quantity becomes a good measure of the probability of the corresponding fluctuation.

The Monte-Carlo events are generated in the horizon reference frame with the geometrical acceptance  $dn \propto \cos\theta_z \sin\theta_z d\theta_z$ , where  $\theta_z$  is the zenith angle. Coordinates of the events are then transformed into the equatorial frame assuming random arrival time. We restrict our analysis to the events with zenith angles  $\theta_z < 45^\circ$ ,

for which the experimental resolution of arrival directions is the best [14].

If clusters at the highest energies are not a statistical fluctuation, one should expect that the spectrum consists of two components, the clustered component taking over the uniform one at a certain energy. The cut at an energy at which the clustered component starts to dominate should give the most significant signal. Motivated by these arguments, we calculated the probability of chance clustering as a function of energy cut. We present here the results for the AGASA [13] and Yakutsk [17] data sets (other experiments are discussed in Section 3). For these simulations, we took the bin size equal to  $2.5^\circ$  and  $4^\circ$  for AGASA and Yakutsk, respectively, which is the quoted (see, e.g., [13, 14]) angular resolution of each experiment multiplied by

$\sqrt{2}$ . The results are summarized in Fig. 1, which shows the probability to reproduce or exceed the observed count in the first bin vs. the energy cut. AGASA curve starts at  $E = 4 \times 10^{19}$  eV because the data at smaller energies are not yet available. Yakutsk has much lower statistics. Both curves rapidly rise to unity in a similar way when the statistics becomes poor. They suggest that the optimum energy cut is higher than can be imposed at present statistics.

The difference between our results and those of [13] (cf. Fig. 1 in this paper and Fig. 12 in [13]) is due to two reasons. First, ten more events with  $E > 4 \times 10^{19}$  have been observed [18] which bring a new doublet. Second, and more important, we calculate a different probability. The difference arises when there is a triplet or higher multiplets in the data. In our approach, a triplet is equivalent to three or two doublets, depending on the relative position of the events (compact or aligned), while higher multiplicity clusters effectively have larger “weight.” In [13], the probabilities of doublets and triplets are calculated separately; the probability of doublets is defined in such a way that a triplet contributes as 3/2 of a doublet. The drawback of this method is that the probabilities of doublets and triplets are not independent, and it is not clear how to combine them. Triplets and higher multiplicity clusters are better accounted for in our method, and the probability of chance clustering, which we get, is lower than in [13].

Correlation functions calculated with the energy cuts corresponding to the lowest chance probability is shown in Fig. 2. Both AGASA and Yakutsk correlation functions have substantial excess in the first bin. The peak in AGASA curve corresponds to 6 doublets (of which 3 actually form a triplet) out of 39 events. The peak in Yakutsk curve corresponds to 8 doublets (of which 3 also come from a triplet) out of 26 events.

Since the number of events in the first bin is not large, its distribution is not well approximated by a Gaussian one, and the deviation in the units of variance is not a good measure for the probability of fluctuations. We calculated the probability directly by counting, in the Monte-Carlo simulation, the number of

occurrences with the same or larger number of events in the first bin. Probabilities in the minima are small (see Fig. 1), so we have recalculated them with  $10^6$  Monte-Carlo sets.

As the lowest probabilities were obtained by scanning over the energy, one may argue that they have to be multiplied by the number of steps in the scan. This is not, however, correct because the results at different energy cuts are not independent: the higher energy set is a subset of the lower energy one. As can be seen from Fig. 1, the chance probability for AGASA is lower than  $10^{-3}$  in the whole energy range  $(4-5) \times 10^{19}$  eV, regardless of the number of steps in the scan. There still may be a correction factor. To estimate it, we made the following numerical experiment. For  $10^3$  randomly generated sets of events, we have performed exactly the same procedure as for the real data, i.e., scanned over energies and obtained  $10^3$  different minimum probabilities. We found that the probability less than  $10^{-2}$  occurred 27 times, while the probability less than  $10^{-3}$  occurred 3 times. Thus, we conclude that the correction factor is of order three. This factor is included in the final results, which are presented in Table 1.

We now turn to the determination of the angular size of the sources. To this end, we calculate the dependence of the probability to have the observed (or larger) number of events in the first bin on the bin size. This dependence is plotted in Fig. 3. Jumps in the curves occur when a new doublet enters the first bin. Despite fluctuations, one can see that the minimum probability corresponds roughly to  $2.5^\circ$  and  $4^\circ$  for AGASA and Yakutsk, respectively. These numbers coincide with the angular resolutions of the experiments, as is expected for sources with an angular size smaller than the experimental resolution. Remarkably, there are no doublets in the AGASA set with separations between  $2.5^\circ$  and  $5^\circ$ , while for the extended source of the uniform luminosity one would expect four times more events within  $5^\circ$  than within  $2.5^\circ$ . Thus, we conclude that the data favor compact sources with angular size less than  $2.5^\circ$ .

If primary particles are charged, actual positions of sources differ from the measured arrival directions because of the deflection in the Galactic magnetic field (GMF). If the clustering is attributed to real sources, it should not disappear but improve when the correction for GMF is taken into account. We have simulated the effect of such a correction making use of the GMF models summarized in [19]. For the charge  $Z = 1$  and BSS-A model, the peak in the first bin does not change significantly; one cannot discriminate between this case and the case of neutral particles. The peak becomes small at  $Z = 2$  and disappears at larger  $Z$  for all GMF models of [19].

3. The other two UHECR experiments, Haverah Park (HP) and Volcano Ranch (VR), do not show significant clustering [20]. With the energy cut  $E > 2.4 \times 10^{19}$  eV and a bin size of  $4^\circ$ , the HP data contain 2 doublets for 1.8 expected, while the VR data contain 1 dou-

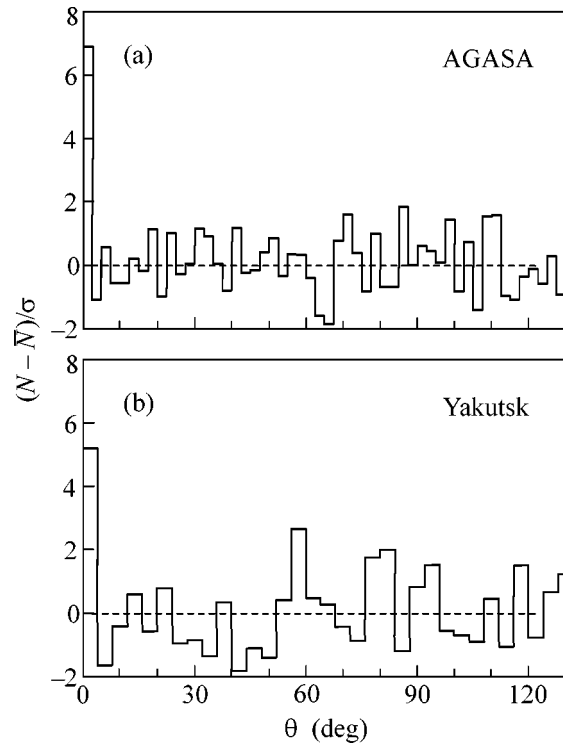


Fig. 2. Angular correlation functions of UHECR with binning angles and cuts in energy quoted in the text.

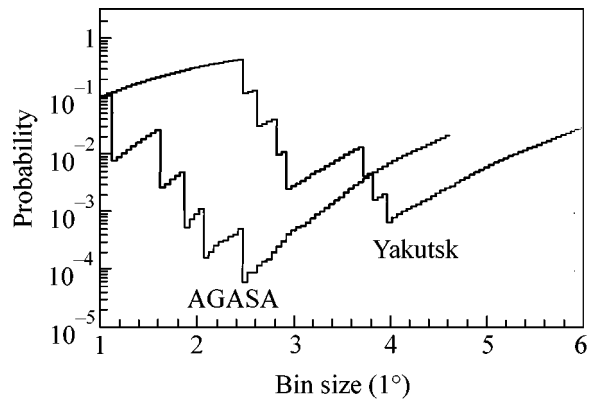


Fig. 3. Probability to have observed count in the first bin vs. the bin size. Cuts in energy correspond to minima of Fig. 1.

blet for 0.1 expected with an isotropic distribution. Let us estimate the combined probability of clustering in all experiments assuming independent Poisson distributions. The number of observed doublets in the AGASA and Yakutsk data are 6 and 8, respectively, while 0.87 and 2.2 are expected (these “effective” expected numbers of doublets are calculated from the condition that probabilities in Table 1 are reproduced, i.e., the “penalty” for the energy scan is included). Thus, 17 doublets are observed for 4.97 expected, which corresponds to the Poisson probability  $2 \times 10^{-5}$ . If HP data are

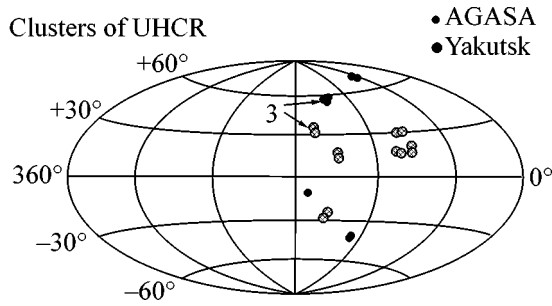


Fig. 4. Observed clusters in Galactic coordinates.

excluded, the probability becomes  $1 \times 10^{-6}$ , while with both HP and VR data excluded the probability is  $4 \times 10^{-6}$ .

It is extremely unlikely that the clustering observed by the AGASA and Yakutsk experiments is a result of a random fluctuation in an isotropic distribution. Rather, the working hypothesis should be the existence of some number of compact sources which produce the observed multiplets. Is this hypothesis consistent with HP and VR data? For a given experiment, the expected number of clusters is determined by the total number of events [21] (see also [22]); at small clustering, it scales like  $N_{\text{tot}}^{3/2}$  [21]. Taking AGASA data as a reference (6 doublets observed, 5.4 expected from sources, and 0.6 expected from chance clustering) allows one to estimate the expected number of doublets in other experiments by adding the doublets expected from sources and the doublets expected from the uniform background (calculated in the Monte-Carlo simulation). The results are summarized in Table 2 together with corresponding Poisson probabilities.

All experiments are roughly consistent with the assumption that the number of sources is such that they produce 5.4 doublets out of 39 events on average. Note that, if HP data are discarded [20], the agreement between other experiments can be made better.

Table 1

Experiment	Bin size	$E_{\text{min}}$ , eV	Chance probability
AGASA	$2.5^\circ$	$4.8 \times 10^{19}$	$3 \times 10^{-4}$
Yakutsk	$4^\circ$	$2.4 \times 10^{19}$	$2 \times 10^{-3}$

Table 2

	$N_{\text{tot}}$	Observed	Expected	Probability
AGASA	39	6	$5.0 \pm 0.6$	–
Yakutsk	26	8	$2.9 \pm 1.6$	0.09
HP	32	2	$4.0 \pm 1.8$	0.07
VR	10	1	$0.7 \pm 0.1$	0.55

According to our simulations, the mean numbers of chance doublets are 0.6 and 1.6 for AGASA and Yakutsk, respectively. Therefore, most of the clusters in the AGASA and Yakutsk data are likely due to real sources. In Fig. 4, we plot these clusters in Galactic coordinates (small and large circles correspond to the AGASA and Yakutsk events, respectively). Positions of triplets are indicated by arrows. The set of AGASA events with  $E > 4 \times 10^{19}$  eV and Yakutsk events with  $E > 2.4 \times 10^{19}$  eV is a suitable choice for the search for correlations with astrophysical objects.

To summarize, the clustering of UHECR is statistically significant and favors compact sources. This places further constraints on models which can resolve the puzzle of the GZK cutoff. Those models which involve large extragalactic magnetic fields [5], as well as models with heavy nuclei as primaries, e.g., [4], are disfavored because they assume total isotropization of the original arrival directions of UHECR. If violation of the Lorentz invariance is the solution of the GZK puzzle and primaries are protons, our results place an extremely strong limit on the extragalactic magnetic fields. Regarding the models of decaying superheavy dark matter, it is important to calculate [23] the angular correlation function predicted by these models and compare it to Fig. 2 in order to see if the clumping on subgalactic scales can be responsible for the clustering of UHECR.

We are grateful to S.I. Bityukov, S.L. Dubovsky, A.A. Mikhailov, V.A. Rubakov, M.E. Shaposhnikov, D.V. Semikoz, and M. Teshima for valuable comments and discussions. This work is supported in part by the Swiss Science Foundation (grant no. 21-58947.99) and the INTAS (grant no. 99-1065).

## REFERENCES

1. M. Takeda *et al.*, Phys. Rev. Lett. **81**, 1163 (1998); M. A. Lawrence, R. J. O. Reid, and A. A. Watson, J. Phys. G **17**, 733 (1991); B. N. Afanasiev *et al.*, in *Proceedings of the International Symposium on Extremely High Energy Cosmic Rays: Astrophysics and Future Observatories, 1996*, Ed. by Nagano, p. 32.
2. K. Greisen, Phys. Rev. Lett. **16**, 748 (1966); G. T. Zatsepin and V. A. Kuzmin, Pis'ma Zh. Éksp. Teor. Fiz. **4**, 144 (1966) [JETP Lett. **4**, 99 (1966)].
3. V. Berezhinsky, M. Kachelriess, and A. Vilenkin, Phys. Rev. Lett. **79**, 4302 (1997); V. A. Kuzmin and V. A. Rubakov, Yad. Fiz. **61**, 1122 (1998) [Phys. At. Nucl. **61**, 1028 (1998)]; V. A. Kuzmin and I. I. Tkachev, Phys. Rep. **320**, 199 (1999).
4. P. Blasi, R. I. Epstein, and A. V. Olinto, Astrophys. J. Lett. **533**, L123 (2000).
5. G. R. Farrar and T. Piran, astro-ph/0010370.
6. S. L. Dubovsky and P. G. Tinyakov, Pis'ma Zh. Éksp. Teor. Fiz. **68**, 99 (1998) [JETP Lett. **68**, 107 (1998)]; hep-ph/9802382.
7. T. J. Weiler, Phys. Rev. Lett. **49**, 234 (1982); D. Fargion, B. Mele, and A. Salis, Astrophys. J. **517**, 725 (1999).

8. D. J. H. Chung, G. R. Farrar, and E. W. Kolb, Phys. Rev. D **57**, 4606 (1998).
9. S. Coleman and S. L. Glashow, Phys. Rev. D **59**, 116008 (1999).
10. V. Berezhinsky, P. Blasi, and A. Vilenkin, Phys. Rev. D **58**, 103515 (1998).
11. G. Gelmini and A. Kusenko, Phys. Rev. Lett. **84**, 1378 (2000); hep-ph/9908276.
12. X. Chi *et al.*, J. Phys. G **18**, 539 (1992); N. N. Efimov and A. A. Mikhailov, Astropart. Phys. **2**, 329 (1994).
13. M. Takeda *et al.*, Astrophys. J. **522**, 225 (1999).
14. Y. Uchihori *et al.*, Astropart. Phys. **13**, 151 (2000).
15. G. Medina-Tanco, astro-ph/0009336.
16. M. Lemoine, G. Sigl, and P. Biermann, astro-ph/9903124.
17. *Catalogue of Highest Energy Cosmic Rays. World Data Center C2 for Cosmic Rays* (Institute of Physical and Chemical Research, Itabashi, Tokyo), Nos. 1–3.
18. N. Hayashida *et al.*, astro-ph/0008102.
19. T. Stanev, astro-ph/9607086.
20. We use the data of Ref. [17]. Unpublished events were added in the analysis of Ref. [14] and more clusters were found.
21. S. L. Dubovsky, P. G. Tinyakov, and I. I. Tkachev, Phys. Rev. Lett. **85**, 1154 (2000).
22. Z. Fodor and S. D. Katz, Phys. Rev. D **63**, 023002 (2001).
23. S. Colombi, P. Tinyakov, and I. Tkachev, in preparation.

# Ion Acceleration during Adiabatic Plasma Expansion: Renormalization Group Approach

V. F. Kovalev\*, V. Yu. Bychenkov\*\*, and V. T. Tikhonchuk\*\*

\* *Institute for Mathematical Modeling, Russian Academy of Sciences, Miusskaya pl. 4a, Moscow, 125047 Russia*

\*\* *Lebedev Institute of Physics, Russian Academy of Sciences, Leninskiĭ pr. 53, Moscow, 117924 Russia*

*e-mail: kovalev@imamod.ru*

Received May 25, 2001

The renormalization group approach is applied to derive an exact solution to self-consistent Vlasov kinetic equations for plasma particles in the quasineutral approximation. The solution obtained describes the one-dimensional adiabatic expansion into vacuum of a plasma bunch with arbitrary initial velocity distributions of the electrons and ions. The ion acceleration is investigated for both a Maxwellian two-temperature initial electron distribution and a super-Gaussian initial electron distribution. © 2001 MAIK “Nauka/Interperiodica”.

PACS numbers: 52.25.Dg; 52.38.Kd; 05.10.Cc

After the paper by Gurevich *et al.* [1] appeared, the problem of plasma expansion into vacuum has been actively studied for many years. Interest in this problem stems primarily from the need to better understand the physics of ion acceleration in the interaction of laser light with plasma and, in particular, to give a quantitative description of the ion acceleration. The study of ion acceleration is among the key problems in various applications of high-power lasers, such as laser fusion, injectors of fast particles, and radioactive sources for apparatuses used in medicine and nuclear physics. Although the process of ion acceleration in an expanding hot laser plasma was described in considerable detail by Gitomer *et al.* [2], recent experiments with nanosecond laser-produced plasmas [3, 4] revealed that the ions can be accelerated to energies higher than the maximum energies predicted in that paper.

Most studies of plasma expansion into vacuum utilized the model of a semibounded plasma with isothermal electrons and cold ions [5–9], which implies a steady source of particles, the possible existence of a quasisteady corona, and the possible onset of the regime of isothermal expansion. However, this model definitely fails to describe the expansion of small plasma bunches such as clusters [3, 4]. The expansion of such small plasma objects is essentially unsteady and is accompanied by the adiabatic cooling of plasma particles. This expansion regime is investigated using a phenomenological hydrodynamic theory [10] and by numerical modeling [11, 12]. An important step in this direction was taken by Dorozhkina and Semenov [13], who obtained an exact self-similar solution to the Vlasov equation for electrons and ions in the quasineutral

approximation. However, the kinetic solution obtained in that paper describes the expansion of a plasma bunch into vacuum in the particular case in which the electrostatic potential is quadratic in the spatial coordinate and, accordingly, the initial conditions imply the same dependence of the electron and ion distribution functions on the coordinate and velocity.

Here, we find a more general (in comparison with [13]) class of solutions to the Cauchy problem for the Vlasov equation in the quasineutral approximation. This class of solutions is derived for arbitrary initial velocity distributions of the electrons and ions by applying the renormalization group approach [14], in which the solution to the initial-value problem is found perturbatively for short time scales ( $t \rightarrow 0$ ) and is continued to longer time scales  $t$  with the help of the renormalization group symmetries (RGS). The solution obtained by Dorozhkina and Semenov [13] is a particular case of the resulting solution. In the present paper, the general renormalization group method is described for the particular case of plasma expansion in planar geometry, which can be easily generalized to the three-dimensional case. We hope that our results will provide a clearer insight into the nature of the experimentally discovered cutoff of the ion spectrum at high energies [3, 4], because the renormalization group method makes it possible to describe strongly nonequilibrium electron distribution functions like those that were observed to form in the experiments of [3, 4] as a result of the generation of accelerated electrons under the action of laser radiation.

We describe the dynamics of a plasma bunch by the following set of two kinetic equations for the electron

and ion distribution functions  $f_\alpha$  (with  $\alpha = e$  for the electrons and  $\alpha = i$  for the ions), which are assumed to depend on the time  $t$ , the coordinate  $x$ , and the velocity component  $v$  along the  $x$ -axis:

$$\partial_t f_\alpha + v \partial_x f_\alpha - (e_\alpha/m_\alpha)(\partial_x \Phi) \partial_v f_\alpha = 0. \quad (1)$$

In the quasineutral approximation used here, we set the charge and current densities in the plasma equal to zero:

$$\int d\mathbf{v} (Zf_i - f_e) = 0, \quad \int d\mathbf{v} v (Zf_i - f_e) = 0, \quad (2)$$

where  $Z = -e_i/e_e$  is the ion charge number. Accordingly, the electric potential  $\Phi$  is expressed in terms of the moments of the distribution functions:

$$e \partial_x \Phi = -m_e \int d\mathbf{v} v^2 \partial_x (Zf_i - f_e) \times \left\{ \int d\mathbf{v} \left( f_e + \frac{Z^2 m_e}{m_i} f_i \right) \right\}^{-1}. \quad (3)$$

We solve Eqs. (1) and (2) with the initial conditions that correspond to the electron and ion distribution functions specified at  $t = 0$ :  $f_e(t = 0) = f_{e0}$  and  $f_i(t = 0) = f_{i0}$ . This formulation of the problem makes it possible to model the expansion of a plasma bunch under the action of a short laser pulse whose duration is much shorter than the characteristic time scale on which the bunch evolves. In this case, there is no need to specify the process of the interaction of laser light with plasma, because this process is incorporated into our model through the particular initial particle distribution functions.

We seek the RGS for Eqs. (1) and (2) as a subgroup of the full group of allowed symmetries. Since we are dealing with the integrodifferential equations, we can calculate the renormalization symmetries by applying the regular approach that was developed by Kovalev *et al.* [15]. This approach makes it possible to calculate the desired symmetries in two steps. First, we calculate the *intermediate* symmetry group allowed by Eqs. (1). Second, we use this symmetry group to analyze the consequences of the nonlocal relationships (2). An important difference between the method proposed here to calculate the intermediate symmetry group and the corresponding method used in [15] is that, instead of treating the variable  $\Phi$  as one of the dependent variables, we consider it to be an as-yet-unknown function, which depends on the variables  $t$  and  $x$  and is calculated from the particle distribution functions obtained in advance. As a result, the group of symmetries in question is broader than the group calculated in [15]: it is an eight-parameter group of transformations defined by two operators of translation along the  $t$  and  $x$  axes, three dilatation operators, the operator of Galilean transformations, the quasineutrality operator, and an additional operator  $X = t^2 \partial_t + tx \partial_x + (x - vt) \partial_v$  of the group of con-

formal transformations. According to the narrowing procedure [14] for the eight-parameter group, it is necessary to determine whether or not each of the solutions to the initial problem that are obtained perturbatively for  $t \rightarrow 0$  will be invariant under the transformations defined by the operators of the sought-for group of renormalization symmetries. As a result, the narrowing procedure yields a set of operators, one of which has the form

$$R = (1 + 2\omega t + \Omega^2 t^2) \partial_t + (\Omega^2 t + \omega) x \partial_x + [\Omega^2 (x - vt) - \omega v] \partial_v. \quad (4)$$

The distribution functions are invariants of the group of transformations with the RGS operator (4) and are expressed in terms of the first two integrals of the first-order equation conjugate to the operator  $R$ . For  $t = 0$  and for an arbitrary dependence of the electric potential on the coordinate, the distribution functions are related to the two energy integrals  $w_{e,i}$  by

$$f_\alpha = F_\alpha(w_\alpha), \quad (5)$$

$$w_\alpha = \frac{1}{2} m_\alpha (v^2 - 2vx\omega + \Omega^2 x^2) + e_\alpha \Phi.$$

Here, the dependence of the potential  $\Phi$  on the  $x$  coordinate is to be found from the quasineutrality condition. The temporal behavior of the particle distribution functions and electric field is described by the finite transformations from the sought-for group that relate the variables  $(x', v')$  at the initial time  $t = 0$  to their values  $(x, v)$  at  $t \neq 0$ :

$$x' = \frac{x}{\sqrt{1 + 2\omega t + \Omega^2 t^2}}, \quad (6)$$

$$(v' - x'\omega)^2 = v^2 - 2\omega v(x - vt) + \Omega^2 (x - vt)^2 - (x')^2 (\Omega^2 - \omega^2).$$

Hence, identifying the variables  $x$  and  $v$  in relationships (5) with the variables  $x'$  and  $v'$  in relationships (6), we arrive at an explicit time dependence of the distribution functions.

We illustrate the solution by using the following two examples for  $\omega = 0$ .

*Example 1.* We assume that, at the initial time  $t = 0$ , the ions obey a Maxwellian velocity distribution function with density  $n_{i0}$  and temperature  $T_i$  and the electrons obey a two-temperature Maxwellian distribution function in which the density and temperature of the hot component are  $n_{h0}$  and  $T_h$  and those of the cold component are  $n_{c0}$  and  $T_e$ , where  $Zn_{i0} = n_{c0} + n_{h0}$  and  $\rho = n_{h0}/Zn_{i0}$ . This example may serve as a model for the expansion of a plasma bunch (e.g., a cluster whose radius is larger than the Debye radius) that is rapidly

and isotropically preheated by a laser field, so that there is a population of hot electrons. Under the quasineutrality conditions (2), the above initial electron and ion distribution functions yield the following dependence of the plasma potential on the variables  $x$  and  $t$ :

$e\Phi(1 + \Omega^2 t^2) = m_e \zeta^2 / 2 - T_e \Psi$ , where  $\zeta = x\Omega / \sqrt{1 + \Omega^2 t^2}$  and the auxiliary function  $\Psi(\zeta)$  is implicitly defined by the equation

$$\zeta^2 = \frac{2}{m_i + Zm_e} [(T_i + ZT_e)\Psi - T_i \ln(1 - \rho + \rho e^{(1 - T_e/T_h)\Psi})]. \quad (7)$$

For the same velocity dependence of the electron and ion distribution functions, e.g., for one-temperature Maxwellian velocity distribution functions without fast electrons ( $\rho = 0$ ), the quasineutrality condition implies that the electrostatic potential  $\Phi$  is quadratic in the  $x$  coordinate; this quadratic dependence was discussed by Dorozhkina and Semenov [13].

The corresponding solutions for the particle distribution functions have the form

$$f_e = (1 - \rho) \frac{Zn_{i0}\sqrt{m_e}}{\sqrt{2\pi T_e}} \times \exp\left[-\Psi - \frac{m_e}{2T_e}(1 + \Omega^2 t^2)(v - u)^2\right] + \rho \frac{Zn_{i0}\sqrt{m_e}}{\sqrt{2\pi T_h}} \exp\left[-\Psi \frac{T_e}{T_h} - \frac{m_e}{2T_h}(1 + \Omega^2 t^2)(v - u)^2\right], \quad (8)$$

$$f_i = \frac{n_{i0}\sqrt{m_i}}{\sqrt{2\pi T_i}} \exp\left[-\Psi - \frac{m_i}{2T_i}(1 + \Omega^2 t^2)(v - u)^2\right] \times (1 - \rho + \rho e^{(1 - T_e/T_h)\Psi}),$$

where  $u = xt\Omega^2/(1 + \Omega^2 t^2)$  is the local plasma flow velocity.

*Example 2.* We assume that, at the initial time  $t = 0$ , the ions obey a Maxwellian velocity distribution function and the electrons obey a super-Gaussian distribution function

$$f_{e0} = \frac{aZn_{i0}\sqrt{m_e}}{\sqrt{T_e}} \exp[-2(w_e/T_e)^2], \quad (9)$$

where  $a = 2^{3/4}/\Gamma(1/4) \approx 0.46$ . This example may serve as a model for the expansion of a plasma bunch that is rapidly preheated by a moderate-intensity laser field via inverse bremsstrahlung absorption, in which case the electrons may relax to a distribution function that is proportional to  $\exp(-v^m)$ , where  $2 \leq m \leq 5$  (see [16] for details). Substituting the electron distribution function (9) into the quasineutrality conditions (2) yields the

following dependence of the auxiliary function  $\Psi$  on the self-similar variable:

$$\zeta^2 = \frac{2}{m_i + Zm_e} \quad (10)$$

$$\times [T_i \Psi^2 + ZT_e \Psi - T_i \ln(a\sqrt{\Psi} K_{1/4}(\Psi^2))],$$

in which case the evolution of the electron and ion distribution functions is described by the formulas

$$f_e = \frac{aZn_{i0}\sqrt{m_e}}{\sqrt{T_e}} \times \exp\left\{-2\left[\Psi + \frac{m_e}{2T_e}(1 + \Omega^2 t^2)(v - u)^2\right]^2\right\}, \quad (11)$$

$$f_i = \frac{an_{i0}\sqrt{m_i}\Psi}{\sqrt{2\pi T_i}} K_{1/4}(\Psi^2) \times \exp\left[-\Psi^2 - \frac{m_i}{2T_i}(1 + \Omega^2 t^2)(v - u)^2\right].$$

In both of these examples, the plasma dynamics is essentially the same. The parameter  $\Omega$ , which characterizes the plasma cooling time, is equal to the reciprocal of the transit time of the rarefaction wave through the plasma,  $\Omega \sim C_s/L$ , where  $L$  is the initial dimension of the plasma bunch and  $C_s = \sqrt{(T_i + ZT_e)/(m_i + Zm_e)}$  is the speed of sound in terms of the initial electron and ion temperatures. On time scales  $\Omega t \gg 1$ , the plasma expansion becomes self-similar: the electron and ion temperatures rapidly decrease as  $1/t^2$ , the local plasma flow velocity approaches the value  $u = x/t$ , and the local

plasma density  $n_i(x, t) = n_{i0}N(\zeta)/\sqrt{1 + \Omega^2 t^2}$  relaxes to the dependence  $n_i(x, t) = n_{i0}N(u)/\Omega t$ . Here,  $N$  is a universal function dependent on the initial electron distribution function. In example 1, this function is  $N = \exp(-\Psi)\{1 - \rho + \rho \exp[(1 - T_e/T_h)\Psi]\}$ , whereas, in example 2, we have  $N = a\sqrt{\Psi} K_{1/4}(\Psi^2)\exp(-\Psi^2)$ . The results obtained are illustrated by Fig. 1, which shows the plots of the ‘‘universal’’ ion density  $N(\zeta)$  as a function of the self-similarity parameter  $\zeta/C_s$  for the following plasma parameters:  $T_e/T_i = 10$ ,  $m_i/m_e = 1836$ , and  $Z = 1$ . In the case of a two-temperature electron distribution function, the plasma density profile has a tail, which is stretched out over a distance of about  $L\sqrt{T_h/T_e}$  from the bunch center. It is precisely the tail ions that are accelerated to high energies on time scales  $\Omega t \gg 1$ , so that the number of ions whose energies are higher than  $ZT_h$  is about  $\rho$ . On the contrary, in the case of a super-Gaussian electron distribution function, the number of ions with energies above  $ZT_e$  is insignifi-

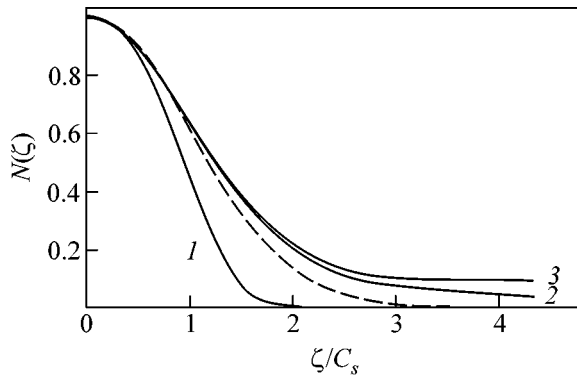


**Fig. 1.** Plasma density  $N = \sqrt{1 + \Omega^2 t^2} (n_i(x, t)/n_{i0})$  as a function of the self-similarity parameter  $\zeta/C_s$  for the relative density  $\rho = 0.1$  and different initial electron distribution functions: (1) a super-Gaussian distribution and a Maxwellian two-temperature distribution with  $T_h/T_c =$  (2) 10 and (3) 100. The dashed curve corresponds to the initial Maxwellian electron distribution function.

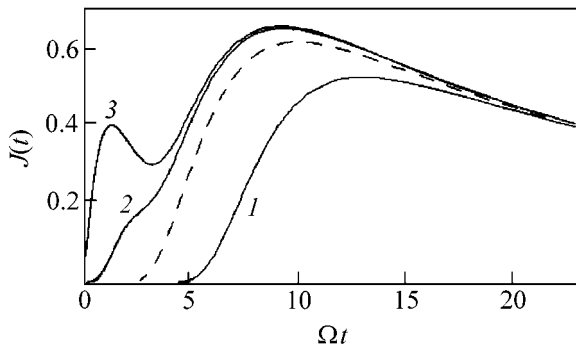


**Fig. 2.** Dependence of the ion current  $J(t)$  in units of  $C_s n_{i0}$  on the time variable  $\Omega t$  at the distance  $x_0 = 10C_s/\Omega$  from the bunch center for the profiles of Fig. 1.

cantly smaller than that in the case of a Maxwellian distribution.

The ion energy distribution is also determined by the function  $N$ , because, for  $\Omega t \gg 1$ , the self-similar variable  $\zeta$  corresponds to the ion velocity  $u$ . It is the function  $N(u)$  that determines the number density of ions with energy  $m_i u^2/2$ . The ion flux that is usually measured by detectors positioned at a distance  $x_0$  from the plasma is described by the function  $J(t) = u(x_0, t) n_{i0} N(\zeta[x_0, t]) / \sqrt{1 + \Omega^2 t^2}$ . The profiles of the relevant signals are shown in Fig. 2 for the same parameters as in Fig. 1 and for the detector position  $x_0 = 10C_s/\Omega$ . On time scales such that  $C_s t < x_0$  ( $\Omega t < 10$ ), the front of the current pulse is formed by fast ions, whose

number and energy increase with the number and energy of the hot electrons.

In conclusion, we note that the renormalization group approach allowed us to derive an exact solution to the kinetic equations for the electrons and ions in the quasineutral collisionless approximation. This solution describes the one-dimensional nonisothermal expansion of a plasma bunch with arbitrary initial velocity distributions of the electrons and ions. In particular, the solution obtained implies that the plasma expansion is accompanied by the adiabatic cooling of plasma particles. As a result, the ions are accelerated to a certain finite energy. The corresponding analysis of the ion spectrum has been carried out for a two-temperature Maxwellian initial electron distribution (with hot and cold electron components) and for a super-Gaussian initial electron distribution. We have shown that the ion spectrum is determined by the initial electron distribution. For this reason, measurements of the ion spectrum can serve as the basis for diagnosing the electron distributions that form in the interaction of ultrashort laser pulses with short-lived (nanosecond) plasmas, e.g., cluster plasmas. In such plasmas, the particle mean free paths are, as a rule, much larger than the characteristic plasma dimensions, so that the collisionless plasma approximation is well satisfied.

Our analysis shows that the method used to obtain the solution imposes certain restrictions on the initial plasma density profile. In particular, the ion acceleration is efficient when there is a tenuous halo around the central plasma region. In the absence of a halo, the quasineutral approximation may fail to hold, in which case the number of ions accelerated to high energies is expected to be smaller. In a future study, we are going to extend our theory to include nonquasineutral plasmas.

This study was supported in part by the Russian Foundation for Basic Research, project nos. 99-01-00232, 00-15-96691, 99-02-17267, and 00-02-16063.

## REFERENCES

1. A. V. Gurevich, L. V. Pariiskaya, and L. P. Pitaevskii, Zh. Éksp. Teor. Fiz. **49**, 649 (1965).
2. S. J. Gitomer, R. D. Jones, F. Begay, *et al.*, Phys. Fluids **29**, 2679 (1986).
3. J. Zweiback, R. A. Smith, T. E. Cowan, *et al.*, Phys. Rev. Lett. **84**, 2634 (2000).
4. E. Springate, N. Hay, J. W. G. Tisch, *et al.*, Phys. Rev. A **61**, 063201 (1999).
5. L. M. Wickens, J. E. Allen, and P. T. Rumsby, Phys. Rev. Lett. **41**, 243 (1978).
6. B. Bezzerides, D. W. Forslund, and E. L. Lindman, Phys. Fluids **21**, 2179 (1978).
7. P. Mora and R. Pellat, Phys. Fluids **22**, 2300 (1979).

8. A. Gurevich, D. Anderson, and H. Wilhelmsson, *Phys. Rev. Lett.* **42**, 769 (1979).
9. A. V. Gurevich and A. P. Meshcherkin, *Zh. Éksp. Teor. Fiz.* **80**, 1810 (1981) [*Sov. Phys. JETP* **53**, 937 (1981)].
10. Ch. Sack and H. Shamel, *Phys. Rep.* **156**, 311 (1987).
11. G. Manfredi, S. Mola, and M. R. Feix, *Phys. Fluids B* **5**, 388 (1993).
12. L. G. Garcia, J. Goedert, H. Figua, *et al.*, *Phys. Plasmas* **4**, 4240 (1997).
13. D. S. Dorozhkina and V. E. Semenov, *Phys. Rev. Lett.* **81**, 2691 (1998); *Pis'ma Zh. Éksp. Teor. Fiz.* **67**, 543 (1998) [*JETP Lett.* **67**, 573 (1998)].
14. V. F. Kovalev, V. V. Pustovalov, and D. V. Shirkov, *J. Math. Phys.* **39**, 1170 (1998).
15. V. F. Kovalev, S. V. Krivenko, and V. V. Pustovalov, *Diff. Uravn.* **29**, 1804 (1993); **29**, 1971 (1993); *Pis'ma Zh. Éksp. Teor. Fiz.* **55**, 256 (1992) [*JETP Lett.* **55**, 253 (1992)].
16. A. B. Langdon, *Phys. Rev. Lett.* **44**, 575 (1980); J. P. Matte, M. Lamoureux, C. Moller, *et al.*, *Plasma Phys. Controlled Fusion* **30**, 1665 (1988).

*Translated by O. Khadin*

# On the Nonphonon Superconductivity of Silver–Oxygen Chains

R. O. Zaitsev

Russian Research Centre, Kurchatov Institute, pl. Kurchatova 1, Moscow, 123182 Russia

e-mail: zaitsev@mbslab.kiae.ru

Received May 3, 2001

It is established on the basis of a concept of strong coupling in a single unit cell that the Cooper instability can occur in a system with hopping between the cations and anions of transition and main-group elements. A phase diagram is constructed for the ferromagnetic ordering in the coordinates  $(h_d, h_p)$  of the degrees of underfilling of, respectively, the  $4d^{10}$  and  $2p^6$  shells of transition and main-group elements. © 2001 MAIK “Nauka/Interperiodica”.

PACS numbers: 74.20.Mn; 74.25.Dw

The oxygen  $2p$  states of the  $C^{4+}O_2$  and  $Pb^{2+}O$  complexes in  $Ag_xPb_6OCO_{9+\beta} = Ag_xO_{1+\beta}CO_2(PbO)_6$  are filled, whereas the lead  $6p$  shells and the carbon  $2sp$  shells are empty [1]. Accordingly, the mean number  $h_d$  of holes in the silver  $4d^{10}$  shell is related to the number  $h_p$  of holes in the remaining oxygen  $2p^6$  shells by the electroneutrality relation

$$(1 + \beta)h_p + xh_d = 2(1 + \beta) - x, \quad (1)$$

$$0 \leq x \leq 1, \quad 0 \leq \beta \leq 1.$$

It is not difficult to consider the case of alternating atoms (Ag–O–Ag–O–...), where  $\beta = 0$  and  $x = 1$ . However, one can show that the respective electroneutrality curve nowhere intersects the Cooper instability region.

Let us consider the case (Ag–O–O–Ag–...), for which  $\beta = 1$  and  $x = 1$ . It will be shown that the electroneutrality line  $2h_p + h_d = 3$  not only intersects the superconducting region but, under certain conditions, passes in the region of maximal density of states that corresponds to the one-dimensional motion along the chain.

Let us use a simple model that takes into account only the transitions ( $t_p$ ) between the nearest lying oxygen anions and ( $t_{pd}$ ) between the silver cations and oxygen anions in one-dimensional O–Ag–O–O–Ag–chains. The consideration is carried out within the framework of the generalized Hubbard–Emery model with infinite Hubbard energy of both  $p$  and  $d$  electrons.

Inasmuch as the system has hexagonal symmetry, the energetically highest underfilled levels are  $(3z^2 - r^2)$

in the silver  $4d$  shell and  $p_z$  in the oxygen  $2p$  shell. Accordingly, the mean occupation numbers of holes  $h_p$  and  $h_d$  change from zero to two, which corresponds to the filling of the upper and lower Hubbard hole subbands.

The equations of state relate the energy difference  $r = \epsilon_p - \epsilon_d$  and the chemical potential  $\mu = -(\epsilon_p + \epsilon_d)/2$  to the mean occupation numbers  $h_p$  and  $h_d$ .

It is pointed out in [1] that the  $Ag_xPb_6OCO_{9+\beta}$  system consists of alternating hexagonal layers, with oxygen layers situated on each side of every layer containing silver cations. Since the separation between the nearest lying silver cations exceeds the separation between the nearest lying oxygens, it is sufficient to take into account for each chain only hopping between the nearest lying oxygen layers ( $t_p$ ) and between the silver cations and oxygen anions ( $t_{pd}$ ).

The energy of elementary excitations are found from the poles of a one-particle Green's function that is defined through the corresponding inverse matrix:

$$(\hat{G}_{(i\omega)}(\alpha))^{-1} \quad (2)$$

$$= \begin{pmatrix} i\omega + \mu + r/2; & -f_d t_{pd}; & -f_d t_{pd} \\ -f_p t_{pd}; & i\omega + \mu - r/2; & -f_p t_p \exp(i\alpha) \\ -f_p t_{pd}; & -f_p t_p \exp(-i\alpha); & i\omega + \mu - r/2 \end{pmatrix}.$$

Here, the so-called end multipliers  $f_p$  and  $f_d$  are introduced. In the zero-loop (“Hubbard I”) approximation,

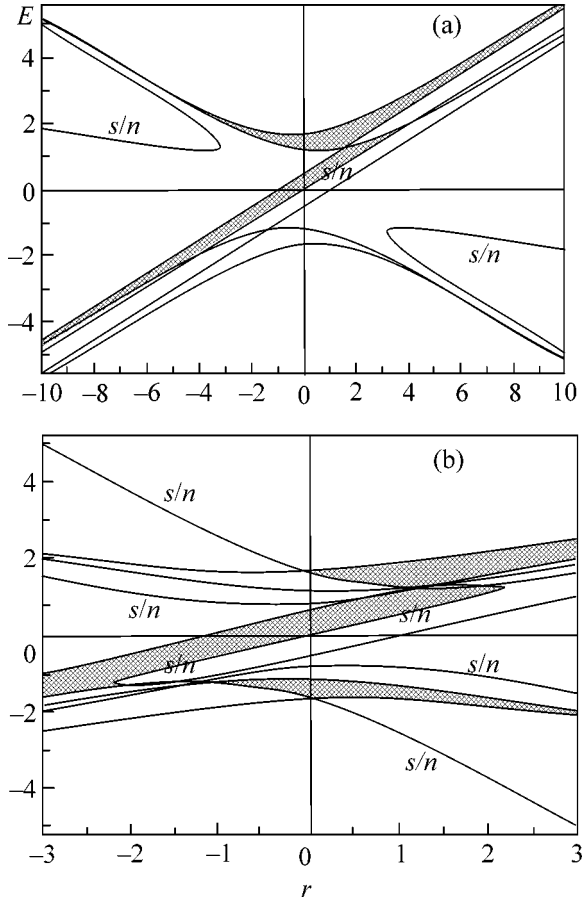


**Fig. 1.** Phase diagram of the  $\text{AgO}_2$  compound at  $T = 0$ . The superconducting regions are crosshatched. (a)  $0 < n_p < 1$ ,  $n_d < 1$  and (b)  $0 < n_p < 1$ ,  $1 < n_d < 2$ .

they are linear functions of the mean number of holes:

$$f_k = 1 - \frac{h_k}{2}, \quad 0 < h_k < 1; \quad (3)$$

$$f_k = \frac{h_k}{2}, \quad 1 < h_k < 2, \quad k = p \text{ or } d.$$

It is convenient to normalize all energy quantities to the multiplier  $(2f_p^2 f_d^2 t_{pd}^2 t_p)^{1/3}$  and introduce the parameter  $v = (2f_d^2 t_{pd}^2 / f_p^2 t_p^2)^{1/3}$ ; then, the three branches  $\xi_\alpha^{(\lambda)}$  =  $\epsilon_\alpha^\lambda - \mu$  of the elementary excitation spectrum are determined from the following equation:

$$\epsilon_d(\alpha)(\epsilon_p(\alpha))^2 - \epsilon_p(\alpha)v - \epsilon_d(\alpha)\frac{1}{v^2} = \cos(\alpha). \quad (4)$$

In this equation,  $\epsilon_p(\alpha) = \epsilon_\alpha - r/2$  and  $\epsilon_d(\alpha) = \epsilon_\alpha + r/2$ , where  $\alpha$  is the dimensionless quasimomentum.

Below, the equations of state are written in the self-consistent form corresponding to the one-loop (Hub-

bard I) approximation [2, 3]. In this case, if the filling occurs in the lower subband, i.e., if  $0 < h_{p,d} < 1$ , one has

$$h_k = \frac{2K_k}{1 + K_k}, \quad f_k = \frac{1}{1 + K_k}, \quad k = p, d, \quad (5a)$$

$$v = \left[ \frac{2t_{pd}^2(1 + K_p)}{t_p^2(1 + K_d)} \right]^{1/3};$$

$$K_k = \sum_{\lambda=1}^3 \int A_k^{(\lambda)}(\alpha) n_F(\epsilon_\alpha^{(\lambda)} - \mu) \frac{d\alpha}{\pi}.$$

If the filling occurs in the upper subband, i.e., if  $1 < h_d < 2$ , then the functions  $h_p, f_p$ , and  $K_{p,d}$  retain their form in the  $0 < h_p < 1$  region. For the remaining quantities, one has

$$h_d = \frac{2}{2 - K_d}; \quad f_d = \frac{1}{2 - K_d}; \quad (5b)$$

$$v = \left[ \frac{2t_{pd}^2(1 + K_p)}{t_p^2(2 - K_d)} \right]^{1/3}.$$

In Eq. (5a), the functions  $A_{p,d}^{(\lambda)}(\alpha)$  are the normal coordinates defined through the quantities  $R_p(\epsilon, r, v) = \epsilon_p^{(\lambda)}(\alpha)\epsilon_d^{(\lambda)}(\alpha) - v/2$  and  $R_d(\epsilon, r, v) = (\epsilon_p^{(\lambda)}(\alpha))^2 - 1/v^2$  as

$$A_p^{(\lambda)} = \frac{R_p(\epsilon, r, v)}{2R_p(\epsilon, r, v) + R_d(\epsilon, r, v)}, \quad (6)$$

$$A_d^{(\lambda)} = \frac{R_d(\epsilon, r, v)}{2R_p(\epsilon, r, v) + R_d(\epsilon, r, v)}.$$

Here, the index  $\lambda$  stands for the three branches of energy spectrum (4).

In the particular calculations at  $T = 0$ , it is convenient to pass to the integration with respect to energy variable  $\epsilon$ . Differentiating Eq. (4), one obtains the equations of state in terms of the new normal coordinates

$$K_k(E) = \int_{-\infty}^E a_k(\epsilon) \frac{d\epsilon}{\pi}, \quad k = (p, d), \quad (7)$$

$$a_k^{(\lambda)} = \text{sgn}(2R_p(\epsilon, r, v) + R_d(\epsilon, r, v)) \times \frac{R_k(\epsilon, r, v)}{\sqrt{1 - \cos^2(\alpha(\epsilon))}}.$$

In Eq. (7), the integration goes over three energy regions where the radicand is positive. Making use of

the explicit form of  $\cos(\alpha)$ , one finds the following boundary values of energy variable:

$$E_{A0} = \frac{r}{2} - \frac{1}{v}, \quad (8)$$

$$E_A^\pm = \frac{1}{2v} (+1 \pm \sqrt{1 + v^2 r^2 + 2vr + 4v^3}),$$

$$E_{B0} = \frac{r}{2} + \frac{1}{v}, \quad (9)$$

$$E_B^\pm = \frac{1}{2v} (-1 \pm \sqrt{1 + v^2 r^2 - 2vr + 4v^3}).$$

Finally,

$$\begin{aligned} Q(\epsilon, r, v) &= 1 - \cos^2(\alpha(\epsilon)) = -\left[\left(\epsilon - \frac{r}{2}\right)^2 - \frac{1}{v^2}\right] \\ &\times \left[\left(\epsilon - \frac{1}{2v}\right)^2 - \frac{1 + v^2 + 2rv + 4v^3}{4v^2}\right] \\ &\times \left[\left(\epsilon + \frac{1}{2v}\right)^2 - \frac{1 + v^2 - 2rv + 4v^3}{4v^2}\right]. \end{aligned} \quad (10)$$

Equations (8)–(10) determine three pairs of boundary values between the allowed and forbidden bands.

The curves  $E_B^+$  and  $E_{B0}$  intersect at the point  $r = v^2/2 - 1/v$ ,  $E = v^2/4 + 1/2v$ . The curves  $E_A^-$  and  $E_{A0}$  intersect at the symmetric point  $r = -v^2/2 + 1/v$ ,  $E = -v^2/4 - 1/2v$ .

Strong correlation of electronic states at  $U_{p,d} = \infty$  gives rise to the  $d$ - $d$  and  $p$ - $p$  scattering. The superconducting state arises if a two-particle vertex function, calculated at zero total momentum and spin, has a singularity. In the ladder approximation, the condition for the appearance of this singularity can be formulated as a condition for the solvability of the corresponding system of homogeneous equations.

The two-particle scattering amplitudes  $\Gamma_{\alpha,\beta;\lambda,v}^0(\mathbf{p})$  are defined as coefficients of the operator products  $\hat{X}_\lambda \hat{X}_v$  obtained as a result of evaluating the double permutation relations  $\{\hat{X}_\alpha, [\hat{X}_\beta, \hat{H}]\}$  for the Hubbard  $X$  operators, where  $\hat{H}$  is the Hamiltonian expressed through the  $X$  operators. The condition for the solvability can eventually be represented in the form of the BCS expression  $T_c \approx t^* \exp(-1/\Lambda\rho)$ , where  $\rho$  is the density of

states at the Fermi surface and  $\Lambda$  is a function of  $\epsilon_p$ ,  $\epsilon_d$ ,  $h_p$ , and  $h_d$  [4–6]:

$$\begin{aligned} (\Lambda\rho)_{(\lambda)} &= \int_0^\pi \left\{ 2 \frac{\epsilon_p(\epsilon^{(\lambda)}(\alpha)) |A_p^\lambda|^2}{f_p} \pm \frac{\epsilon_d(\epsilon^{(\lambda)}(\alpha)) |A_d^\lambda|^2}{f_d} \right\} \\ &\times \delta(\epsilon_\alpha^{(\lambda)} - \mu) \frac{d\alpha}{\pi}. \end{aligned} \quad (11)$$

Here,  $A_{p,d}^\lambda$  are normal coordinates (6) entering into equations of state (5).

Let us pass on to the energy variable and integrate in Eq. (11), to get

$$\begin{aligned} \Lambda\rho(\epsilon = E) &= \left\{ \frac{2}{f_p} \epsilon_p(E) R_p^2(E, r, v) \pm \frac{1}{f_d} \epsilon_d(E) R_d^2(E, r, v) \right\} \\ &\times \frac{1}{|2R_p(E, r, v) + R_d(E, r, v)| \sqrt{Q(E, r, v)}}. \end{aligned} \quad (12)$$

This expression with the upper sign relates to the region  $0 < n_d < 1$ ,  $0 < n_p < 1$ . With the lower sign, it relates to the region  $1 < n_d < 2$ ,  $0 < n_p < 1$ .

To construct the phase diagram in the region  $1 < n_p < 2$ , it is sufficient to perform the particle-hole symmetry transformation  $n_p \rightarrow 2 - n_p$ ,  $n_d \rightarrow 2 - n_d$ .

Setting  $\Lambda = 0$ , one obtains the equation for the boundary between the superconducting and normal phases at  $T = 0$ . In conjunction with the equations of state, this condition determines the region of existence of superconductivity in  $(h_p, h_d)$  coordinates.

For the particular calculations, it is necessary to specify the ratio  $t_{pd}/t_p$  of hopping integrals.

Since the wave functions of the oxygen  $2p$  states drop with distance much more rapidly than the wave functions of the silver  $4d$  states, it is assumed in the calculations that  $t_{pd} = 2t_p$ . Therefore, if the filling occurs in the lower  $p$  subband, then

$$v \approx 2 \left( \frac{1 + K_p}{1 + K_d} \right)^{1/3} \quad \text{for } 0 < n_d < 1; \quad (13)$$

$$v \approx 2 \left( \frac{1 + K_p}{2 - K_d} \right)^{1/3} \quad \text{for } 1 < n_d < 2. \quad (14)$$

One can verify that the electroneutrality line  $2h_p + h_d = 3$  corresponding to the O–Ag–O–O–Ag–O... chains intersects the superconducting region.

Let us first consider the limiting case  $r \rightarrow \pm\infty$ . In this limit, the following expansion in powers of  $1/r$  holds true:

$$E(\alpha)^{(\pm)} \approx \frac{r}{2} \pm \frac{1}{v} + \frac{v}{2r} (1 \pm \cos(\alpha)). \quad (15)$$

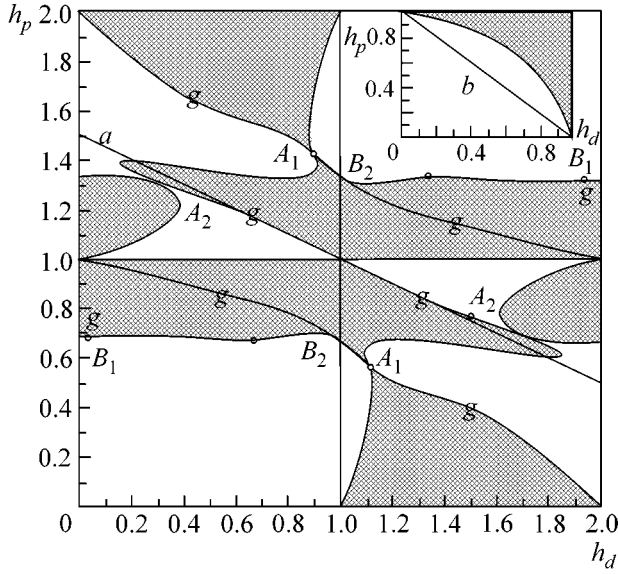


**Fig. 2.** Phase diagram of the  $\text{AgO}_2$  compound at  $T = 0$  and  $t_{pd} = 2t_p$ ; (a) the electroneutrality line  $2n_p + n_d = 3$ . Inset: (b) the electroneutrality line  $n_p + n_d = 1$ .

A similar expansion for the normal coordinates reads

$$A_p^{(\pm)} = \frac{1}{2} \left[ 1 - \frac{v}{2r^2} (1 \pm \cos \alpha) \right], \quad (16)$$

$$A_d = \frac{v}{2r^2} (1 \pm \cos \alpha).$$

Thus, at  $r < 0$ , the  $d$  subbands are empty and the filling occurs only in the two  $p$  subbands. Accordingly, the equations of state for the  $p$  holes has the form

$$h_p = \frac{2K_p}{1 + K_p}, \quad (17)$$

$$K_p = \frac{1}{2\pi} \sum_{\lambda = \pm 0} \int_{-\pi}^{\pi} n_F(E(\alpha)^{(\lambda)} - \mu) d\alpha.$$

One can see that at  $r < -6$  the boundary of the superconducting region passes within the narrow hybridized gap, where  $E^-(\alpha) < \mu < E^+(\alpha)$ . For this reason, the superconductivity arises when the lower subband is completely filled, while the energetically next subband is  $E^+(\alpha)$ . It then follows that the superconductivity at  $h_d = 0$  arises when  $K_p = 1/2$ . In other words, the superconductivity at  $h_d = 0$  arises when  $h_p \geq 2/3$ .

At large positive values of parameter  $r$ , the  $d$  subband is filled first as the energy increases. However, under these conditions, the superconductivity arises at none of the  $h_d$  values.

If the energy is high to an extent that the  $p$ -hole subbands start to fill, then one again can use the expansion in powers of  $1/r$ .

At high  $r > 6$ , the condition for the occurrence of superconductivity is met only for the highest  $p$  subband. Because of this, all relationships in Eqs. (15) and (16), which are valid for  $r$  values negative and large in magnitude, prove to be valid for large positive  $r$  as well. At  $h_d = 1$ , the superconductivity arises when  $K_p = 1/2$ . In other words, the superconductivity at  $h_d = 1$  occurs under the condition that  $h_p \geq 2/3$ .

The same result holds in the region  $1 < h_d < 2$ , so that the phase curve passes through three points, each situated at a "height"  $h_p = 2/3$  for three integer values  $h_d = 0, 1$ , and  $2$ .

The symmetric point  $r = 0, E = 0$  corresponds to the half-filling  $K_p = K_d = 1/2$ . At this point,

$$n_{po} = \frac{2}{3}, \quad n_{do} = \frac{2}{3} \quad \text{for } (0 < n_p < 1, 0 < n_d < 1); \quad (18)$$

$$n_{po} = \frac{2}{3}, \quad n_{do} = \frac{4}{3} \quad \text{for } (0 < n_p < 1, 1 < n_d < 2).$$

For a qualitative analysis, it is sufficient to assume that the end multipliers  $f_{p,d}$  are of the same order of magnitude. In other words, it can be assumed that the  $v$  value is fixed, while the  $f_{p,d}$  multipliers drop out from Eq. (14).

Setting, for definiteness,  $v = 2$  in Eqs. (11)–(14), one obtains the phase diagram in  $(E, r)$  coordinates (Fig. 1).

An important feature of the phase diagrams is that they contain four-critical points at the intersections of the boundary curves of superconducting and semiconductor (normal) phases. To determine the coordinates of these points, it is sufficient to demand that the right-hand and left-hand sides of the condition for the appearance of superconductivity  $\Lambda = 0$  [see Eq. (12)] independently turn to zero:

$$R_p(E, r, v) = 0, \quad R_d(E, r, v) = 0$$

or

$$r = \pm \left( -\frac{1}{v} + \frac{v^2}{2} \right), \quad E = \pm \frac{1}{2} \left( \frac{1}{v} + \frac{v^2}{2} \right). \quad (19)$$

The coordinates of these points coincide with the coordinates of the points where the hybridized gaps  $E_{A0}$ ,  $E_A^-$ , and  $E_{B0}$ ,  $E_B^+$  collapse.

Thus, one can state that these points are six-critical, because, when moving around each of them, one successively intersects the boundaries between the superconducting and normal metallic, normal metallic and normal semiconductor, and normal semiconductor and superconducting phases.

Let us consider the behavior of the phase diagram for integer  $h_p$  values. In the  $0 < h_d < 1$  region, the situation is quite simple. At small  $h_p$ , the superconductivity is absent, while at  $h_p \leq 1$  it occurs for all  $0 < h_d < 1$ .

The situation is reversed in the region  $1 < h_d < 2$  (Fig. 2). At small  $h_p$ , the superconductivity occurs for all  $1 < h_d < 2$ , and it is absent at  $h_p \leq 1$  for all  $0 < h_d < 1$ .

The final form of the phase diagram is depicted in Fig. 2. The AgO electroneutrality line nowhere intersects the Cooper instability region (straight line  $b$  in the inset in Fig. 2). The AgO<sub>2</sub> electroneutrality line passes near the edge energy of the upper hybridized subband. In this region, the density of states has a root singularity, so that the superconducting transition temperature can be expected to be maximal just in this region. Formally, the right-hand side of the BCS expression becomes infinite at this boundary. In fact, this implies the crossover to the power-law dependence of the superconducting transition temperature on the scattering amplitude at the Fermi surface.

It is also worthy of note that both coefficients  $R_p$  and  $R_d$  tend to zero as the four-critical point  $A_2$  is

approached, so that the dimensionless BCS constant remains finite at the very point  $A_2$ .

#### REFERENCES

1. D. Djurek, Z. Medunic, A. Tonejc, and M. Paljevic, Preprints I, II (Zagreb, Croatia).
2. J. Hubbard, Proc. R. Soc. London, Ser. A **276**, 238 (1963).
3. V. J. Emery, Phys. Rev. Lett. **58**, 2794 (1987).
4. R. O. Zaitsev, Phys. Lett. A **134**, 199 (1988).
5. R. O. Zaitsev, Fiz. Tverd. Tela (Leningrad) **30**, 1631 (1988) [Sov. Phys. Solid State **30**, 942 (1988)].
6. R. O. Zaitsev, Pis'ma Zh. Éksp. Teor. Fiz. **73**, 373 (2001) [JETP Lett. **73**, 331 (2001)].

*Translated by V. Sakun*

# Spin Dynamics and Structural Phase Transitions in Quasi-2D Antiferromagnets $R_2CuO_4$ ( $R = Pr, Sm, \text{ and } Eu$ )

E. I. Golovenchits\* and V. A. Sanina

Ioffe Physicotechnical Institute, Russian Academy of Sciences,  
Politekhnicheskaya ul. 26, St. Petersburg, 194021 Russia

\* e-mail: E.Golovenchits@pop.ioffe.rssi.ru

Received May 24, 2001

Spin and lattice dynamics of  $R_2CuO_4$  ( $R = Pr, Sm, \text{ and } Eu$ ) crystals were studied over the frequency and temperature ranges 20–250 GHz and 5–350 K, respectively. The absorption coefficients of the  $R_2CuO_4$  crystals ( $R = Pr, Sm, \text{ and } Eu$ ) were found to change dramatically at temperatures of, respectively, 20, 80, and 150 K over a broad frequency range above 120 GHz. The absorption jumps were caused by the structural phase transitions. Broad spin-wave bands were observed in the high-temperature phases of all crystals studied. Absorption lines due to lattice dynamics were observed near the temperatures of structural phase transition over a broad frequency range, including the frequencies corresponding to the spin-wave bands. © 2001 MAIK “Nauka/Interperiodica”.

PACS numbers: 61.50.Ks; 64.60.Ht; 75.30.Ds; 76.50.+g

$R_2CuO_4$  ( $R = La, Pr, Nd, Sm, Gd, \text{ and } Eu$ ) crystals are quasi-2D antiferromagnets with a giant exchange within the  $CuO_2$  layers (exchange constant  $J_p l \approx 120\text{--}150$  meV [1]). A quasi-2D long-range order caused by a weak interplanar exchange is characterized by Néel temperatures  $T_N \approx 250\text{--}300$  K.

It is commonly thought that crystals of the  $R_2CuO_4$  family with rare-earth ions have the  $T'$ -type tetragonal structure at any temperature. However, it is pointed out in a number of studies that some of these crystals exhibit structural distortions and structural phase transitions. For example, the X-ray studies of  $Eu_2CuO_4$  [2] have shown that it undergoes structural phase transition at temperature  $T \sim 150$  K. In the low-temperature phase, limited-scale rhombic distortions were observed in the  $CuO_2$  layers. At temperatures above 150 K, these distortions disappeared. The magnetic, low-frequency dielectric, and microwave studies of  $Eu_2CuO_4$  [3–5] showed that the structural and magnetic properties simultaneously change at the phase transition near  $T \sim 150$  K. The results of this work suggest that the structural phase transitions and the coupling between the spin-wave and lattice excitations are, likely, typical for  $R_2CuO_4$ .

This study is devoted to the spin and lattice dynamics of  $R_2CuO_4$  ( $R = Pr, Sm, \text{ and } Eu$ ) crystals. The temperature dependences of the absorption coefficient were studied for the electromagnetic waves over the frequency and temperature ranges 20–250 GHz and 5–350 K, respectively. Measurements were made with a quasi-optical spectrometer. A backward-wave tube was used as a radiation source, and the signal was

detected by InSb detectors. Samples shaped like plates with their plane perpendicular to the crystal axis were arranged perpendicular to the wave propagation direction and completely partitioned the beam. The alternating electric and magnetic fields were oriented in the  $ab$  crystal plane ( $CuO_2$  layers). The electric field was aligned with the sample holder axis, about which the sample can be rotated. The temperature dependences of the fractional absorption coefficient  $\Gamma = 1 - P(T)/P(T = 5\text{ K})$ , where  $P(T)$  and  $P(T = 5\text{ K})$  are the microwave signal powers transmitted through the sample at temperatures, respectively,  $T$  and  $T = 5\text{ K}$ , were studied at fixed frequencies. The  $\Gamma(T)$  dependences at different frequencies were used to construct the frequency dependences for this coefficient at fixed temperatures. Generally, to determine quantitatively the absorption coefficient, information about the phase of transmitted wave and the reflected power is required. However, in a search for the absorption bands, which was the main purpose of this study, one could restrict oneself to the measurement of the coefficient  $\Gamma$ .

One can see from Fig. 1 that the coefficient  $\Gamma$  increases sharply in the narrow temperature intervals near temperatures of 20, 80, and 150 K for the  $R_2CuO_4$  ( $R = Pr, Sm, \text{ and } Eu$ ) crystals, respectively. At temperatures below the jumps, the crystals are virtually transparent at the frequency chosen. At temperatures above the jumps, the coefficient  $\Gamma$  increases rapidly and then virtually does not change upon further rise in temperature to 300–350 K. It is also seen that the temperature dependences of the absorption coefficients of the  $R_2CuO_4$  ( $R = Pr, Sm, \text{ and } Eu$ ) crystals are similar and qualitatively differ from the same dependence for

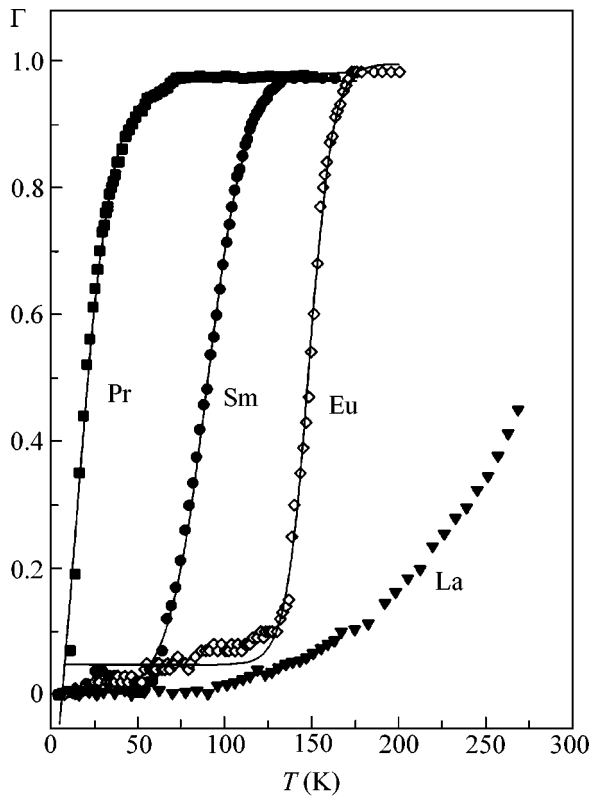


**Fig. 1.** Temperature dependences of the fractional absorption coefficient  $\Gamma$  for the  $R_2CuO_4$  ( $R = La, Pr, Sm,$  and  $Eu$ ) crystals. The frequency equals 169 GHz. The external magnetic field is  $H_0 = 0$ . The curves are recorded in the slow heating regime. The solid lines are the Boltzmann approximations  $\Gamma = \frac{\Gamma_1 - \Gamma_2}{1 + \exp(T - T_0)/dT} + \Gamma_2$ , where  $\Gamma_1$  is the

absorption coefficient at temperature  $T = -\infty$ ,  $\Gamma_2$  is the same at  $T = +\infty$ ,  $T_0$  is the temperature at which  $\Gamma = 0.5(\Gamma_1 + \Gamma_2)$ , and  $dT$  is the width of the temperature interval where the coefficient  $\Gamma$  sharply changes. The values of  $T_0$  and  $dT(K)$  for the  $R_2CuO_4$  ( $R = Pr, Sm,$  and  $Eu$ ) crystals are equal, respectively, to  $19.52 \pm 2.13$  and  $13.03 \pm 0.79$  for Pr,  $86.09 \pm 0.24$  and  $10.49 \pm 0.21$  for Sm, and  $115.82 \pm 0.62$  and  $10.78 \pm 0.53$  for Eu.

$La_2CuO_4$ . The absorption in the latter increases smoothly with temperature, probably, due to carriers that are thermally activated from impurities and defects. As can be seen, this attenuation (which can be assumed to be approximately the same for all  $R_2CuO_4$  crystals) is much weaker than the absorption in the crystals at temperatures above  $T_0$  (see caption to Fig. 1).

A jumpwise change in the absorption with changing temperature suggests that we deal with the phase transitions near the temperatures  $T_0$ . Indeed, as was pointed out above,  $Eu_2CuO_4$  undergoes structural phase transition at  $T \sim 150$  K. The fact that the curves in Fig. 1 are similar for all crystals suggests that the jumps in  $\Gamma(T)$  have a common origin, i.e., that the  $Pr_2CuO_4$  and  $Sm_2CuO_4$  crystals also undergo structural phase transi-

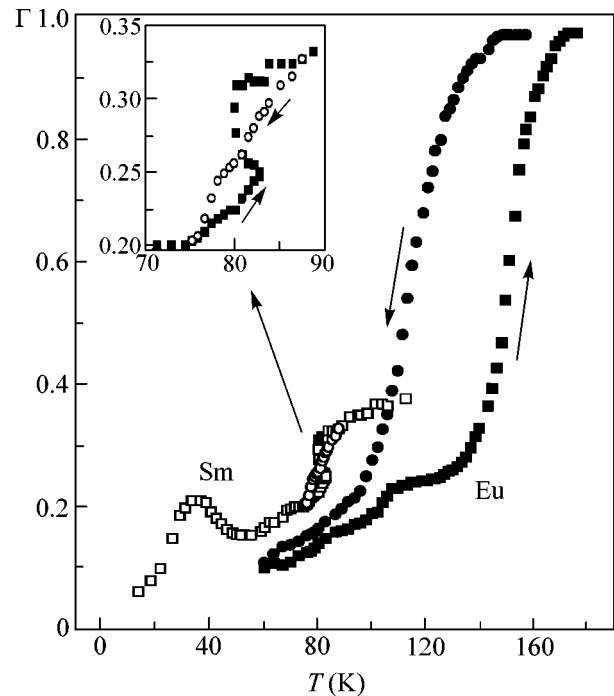


**Fig. 2.** The same as in Fig. 1, but for the  $Eu_2CuO_4$  (frequency  $f = 169$  GHz) and  $Sm_2CuO_4$  ( $f = 34$  GHz) crystals, recorded in the slow cooling and heating regimes near the temperatures of 150 and 80 K, respectively. The arrows indicate the directions of changing temperature. The absorption line of magnetic origin is seen for  $Sm_2CuO_4$  near  $T \approx 40$  K. Inset: the  $S$ -like instability and the hysteresis region for  $Sm_2CuO_4$ .

tions at temperatures of 20 and 80 K, respectively. In the low-temperature phases, the crystals do not show fundamental absorption bands at the corresponding frequencies, whereas such bands appear in the high-temperature phases. One can conclude from the polarization properties of absorption bands that they are due to the spin-wave excitations in the  $CuO_2$  plane of crystals. The absorption coefficient decreased upon turning the sample through a small angle (several degrees) about the holder axis. With such a turn, the alternating electric field remained in the  $ab$  crystal plane, while the alternating magnetic field left this plane. The angle of rotation was sufficiently small that the microwave power could not bypass the sample.

One can see from Fig. 2 that the structural phase transitions in the  $Sm_2CuO_4$  and  $Eu_2CuO_4$  crystals are first-order transitions. The absorption coefficient of  $Eu_2CuO_4$  shows a strong hysteresis:  $T_0 \approx 150$  K on heating and  $T_0 \approx 120$  K on cooling. Similar hysteresis, though smaller in amplitude (5–10 K), was also observed for  $Sm_2CuO_4$  and  $Pr_2CuO_4$  near temperatures of 80 and 20 K, respectively. In the frequency range where there is no spin-wave absorption, the  $S$ -like instability was observed in the  $\Gamma(T)$  dependence for  $Sm_2CuO_4$  near the structural phase transition; the rate

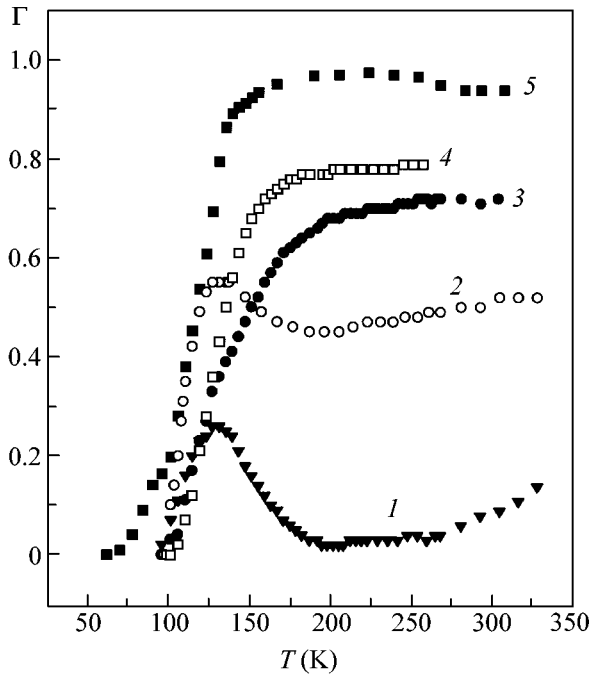


**Fig. 3.** The same as in Fig. 1, but for the  $\text{Eu}_2\text{CuO}_4$  crystal at frequencies for which the curves have the most characteristic shapes. Curves 1–5 correspond to (1) 55, (2) 78.8, (3) 120, (4) 150, and (5) 170 GHz.

of changing temperature of the sample decreased upon uniform heating and the sample cooled down (see inset in Fig. 2). Among the crystals studied, the phase transition in  $\text{Pr}_2\text{CuO}_4$  proved to be the most diffuse (most probably, of the first order close to the second order).

In the  $\text{Pr}_2\text{CuO}_4$  and  $\text{Eu}_2\text{CuO}_4$  crystals, additional absorption lines were observed near the temperatures  $T_0$  in the frequency range where the spin-wave bands were absent (lines 1 and 2 in Fig. 3). These lines can be naturally associated with the lattice dynamics in the vicinity of structural phase transitions. Note that the intensity of the lines of type 1 in Fig. 3 did not change upon the above-mentioned rotation of the sample about the holder axis, suggesting their electric nature.

One can see from Fig. 3 that the character of temperature dependence changes sizably for the absorption coefficients at different frequencies. With  $\text{Eu}_2\text{CuO}_4$ , the lines due to lattice dynamics are clearly seen at frequencies of 55 and 78.8 GHz. At frequencies above 120 GHz, the absorption bands due to spin-wave modes are mostly seen. For  $\text{Pr}_2\text{CuO}_4$  and  $\text{Sm}_2\text{CuO}_4$ , the dependences are similar to those shown in Fig. 3 at the same frequencies, but the features in these curves are shifted to temperatures of 20 and 80 K, respectively.

We failed to observe the short-wavelength edge of spin-wave bands for all crystals (Fig. 4), up to the maximum measurement frequency (250 GHz). The observed bands, which are caused by the oscillations of the total moment, are energetically close to the band

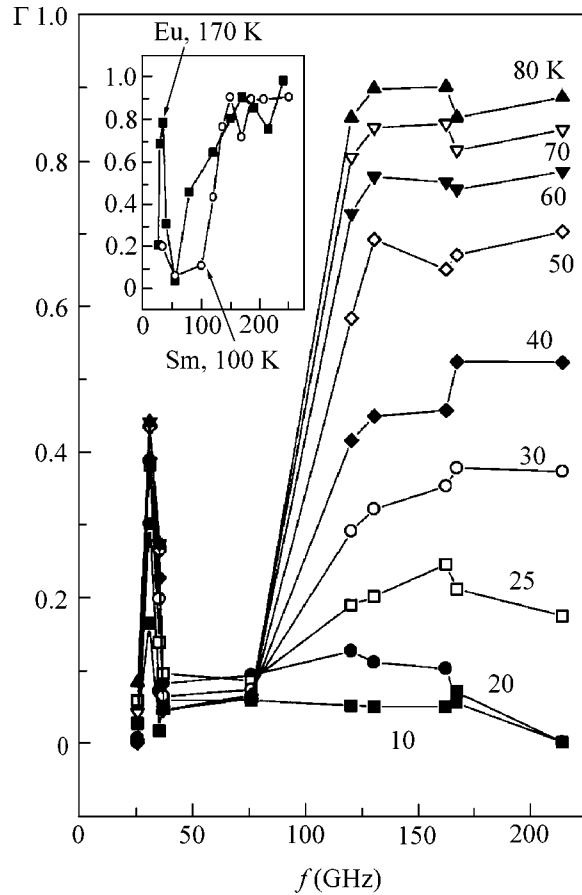


**Fig. 4.** Frequency dependences of the absorption coefficient for  $\text{Pr}_2\text{CuO}_4$  at several temperatures in the range 10–80 K. Inset: the same for the  $\text{Eu}_2\text{CuO}_4$  crystal at  $T = 170$  K and the  $\text{Sm}_2\text{CuO}_4$  crystal at  $T = 100$  K.

observed for the antiferromagnetic vector in inelastic neutron scattering by  $\text{Pr}_2\text{CuO}_4$  [6, 7]. According to these studies, the band is due to the in-plane spin-wave mode, for which the gap is determined by the quadratic anisotropy within the  $\text{CuO}_2$  layer.

As is seen from Fig. 4, the absorption coefficient (and the slope of the low-frequency band edge) of the in-plane spin-wave mode in the  $\text{R}_2\text{CuO}_4$  ( $\text{R} = \text{Pr}, \text{Sm}$ , and  $\text{Eu}$ ) crystals depends strongly on the temperature at temperatures near  $T_0$  and does not above 90, 100, and 170 K, respectively. The absorption band edge (i.e., gap in the spin-wave spectrum) was determined from the half-height at the low-frequency slope and found to change with temperature, as was reported for  $\text{Pr}_2\text{CuO}_4$  in [6]. In [8], this temperature dependence was explained by the interaction of spin waves in the presence of anisotropy violating the total spin conservation. However, it follows from our results that an alternative reason associated with the structural phase transitions is also possible for the temperature dependence of the gap. Indeed, the ratio of the coexisting low- and high-temperature phases, whose spin-wave spectra are dif-

ferent, changes with changing temperature near the phase transitions.

A comparatively narrow absorption line was also observed near 30 GHz for the high-temperature phases of the  $\text{Eu}_2\text{CuO}_4$  and  $\text{Pr}_2\text{CuO}_4$  crystals (Fig. 4). We assign this line to the well-defined two-dimensional homogeneous spin-wave excitations that were previously assumed to occur in the  $\text{CuO}_2$  layers and contribute to the microwave magnetic susceptibility [5, 9].

Note that the intensity of the absorption lines due to lattice dynamics (lines of types 1 and 2 in Fig. 3) increases with frequency. They also occur at frequencies of the in-plane spin-wave modes. Consequently, the absorption bands near the temperatures of structural phase transitions at frequencies higher than 120 GHz are likely not only due to the spin waves, but represent mixed spin and lattice modes. Since the character of these bands changes only slightly with an increase in temperature, the mixed character of excitations is, probably, retained over the entire temperature range of a high-temperature phase. The large band widths may be caused by the structural inhomogeneities that are typical of the high-temperature phases [4, 9]. The absorption in the band also depends weakly on the external magnetic field. In such a situation, the observation of antiferromagnetic resonance by the ordinary methods (with field sweep) is impracticable. These resonances were observed in the low-temperature phases of our crystals (see Fig. 2) and, earlier, in some other crystals [10, 11].

In summary, the  $\text{R}_2\text{CuO}_4$  ( $\text{R} = \text{Pr}, \text{Sm}, \text{and Eu}$ ) crystals undergo structural phase transitions, respectively, at temperatures of 20, 80, and 150 K. In the high-temperature phases, the dynamic properties of all crystals studied were found to be similar. The temperatures of structural phase transitions and the dynamic properties of the low-temperature phases of different crystals are

different and, most probably, governed by the type of rare-earth ion.

This work was supported in part by the Foundation of the Presidium of Russian Academy of Sciences "Basic Research" and the Russian Foundation for Basic Research "Scientific Schools," project no. 00-15-96757.

#### REFERENCES

1. S. Chakravarty, B. Halperin, and D. Nelson, *Phys. Rev. B* **39**, 2344 (1989).
2. V. P. Plakhty, A. B. Stratilatov, and S. Beloglazov, *Solid State Commun.* **103**, 683 (1997).
3. A. V. Babinskiĭ, E. I. Golovenchits, N. V. Morozov, *et al.*, *Fiz. Tverd. Tela (St. Petersburg)* **34**, 60 (1992) [*Sov. Phys. Solid State* **34**, 31 (1992)].
4. A. V. Babinskiĭ, S. L. Ginzburg, E. I. Golovenchits, and V. A. Sanina, *Pis'ma Zh. Ėksp. Teor. Fiz.* **57**, 289 (1993) [*JETP Lett.* **57**, 299 (1993)].
5. E. I. Golovenchits, S. L. Ginzburg, V. A. Sanina, and A. V. Babinskiĭ, *Zh. Ėksp. Teor. Fiz.* **107**, 1641 (1995) [*JETP* **80**, 915 (1995)].
6. A. S. Ivanov, P. Bourges, and D. Petitgrand, *Physica B (Amsterdam)* **259–261**, 879 (1999).
7. D. Petitgrand, S. V. Maleyev, Ph. Bourges, and A. S. Ivanov, *Phys. Rev. B* **59**, 1079 (1999).
8. S. V. Maleyev, *Phys. Rev. Lett.* **85**, 3281 (2000).
9. E. I. Golovenchits and V. A. Sanina, *Physica B (Amsterdam)* **284–288**, 1369 (2000).
10. V. V. Eremenko, S. A. Zvyagin, V. V. Pishko, *et al.*, *Pis'ma Zh. Ėksp. Teor. Fiz.* **52**, 955 (1990) [*JETP Lett.* **52**, 338 (1990)].
11. A. I. Smirnov, S. N. Barillo, and D. I. Zhigunov, *Zh. Ėksp. Teor. Fiz.* **100**, 1690 (1991) [*Sov. Phys. JETP* **73**, 934 (1991)].

*Translated by V. Sakun*

# Transition from the Antiferromagnetic to a Nonmagnetic State in FeBO<sub>3</sub> under High Pressure

I. A. Troyan<sup>1</sup>, A. G. Gavrilyuk<sup>1</sup>, V. A. Sarkisyan<sup>2</sup>, I. S. Lyubutin<sup>2</sup>, R. Rüffer<sup>3</sup>, O. Leupold<sup>3,4</sup>, A. Barla<sup>3</sup>, B. Doyle<sup>3,4</sup>, and A. I. Chumakov<sup>3</sup>

<sup>1</sup> Institute of High Pressure Physics, Russian Academy of Sciences, Troitsk, Moscow region, 142190 Russia

<sup>2</sup> Shubnikov Institute of Crystallography, Russian Academy of Sciences, Moscow, 117333 Russia

e-mail: lyubutin@ns.crys.ras.ru

<sup>3</sup> European Synchrotron Radiation Facility, BP-220 F-38043 Grenoble Cedex, France

<sup>4</sup> II. Institut für Experimentalphysik, Universität Hamburg, D-22761 Hamburg, Germany

Received May 25, 2001

A <sup>57</sup>FeBO<sub>3</sub> single crystal is studied by the nuclear forward scattering (NFS) method. The NFS time spectra from <sup>57</sup>Fe nuclei are recorded at room temperature under high pressures up to 50 GPa in a diamond anvil cell. In the pressure interval  $0 < p < 44$  GPa, the magnetic field  $H^{\text{Fe}}$  at the <sup>57</sup>Fe nuclei is found to increase nonlinearly, reaching a maximum value of 48.1 T at  $p = 44$  GPa. As the pressure increases further and reaches the point  $p = 46$  GPa, the field  $H^{\text{Fe}}$  abruptly drops to zero, indicating that a transition from the antiferromagnetic to a nonmagnetic state occurs in the crystal. In the pressure interval  $0 < p < 46$  GPa, the magnetic moments of the iron ions lie in the (111) basal plane of the crystal. Several possible mechanisms of magnetic collapse are discussed. © 2001 MAIK “Nauka/Interperiodica”.

PACS numbers: 75.30.Kz; 61.50.Ks; 75.25.+z

Iron borate FeBO<sub>3</sub> has a calcite rhombohedral structure, belongs to the  $R\bar{3}c(D_{3d}^6)$  space group [1, 2], and is an antiferromagnet with a weak ferromagnetism and Néel point  $T_N = 348$  K [2]. The magnetic Fe<sup>3+</sup> ions are in an octahedral environment formed by oxygen ions with (Fe–O) interion distances of 2.028 Å, (Fe–Fe) distances of 3.601 Å, and (O–Fe–O) bond angles of 91.82° and 88.18° [3]. Thus, the environment formed by six oxygen ions around iron is almost cubic. At normal pressure and room temperature, the magnetic moments of two iron ion sublattices lie in the (111) basal plane and are almost antiparallel. The angle  $\varphi$  between them is  $\sim 0.9^\circ$  [4], and the resulting weak ferromagnetic moment also lies in the basal plane. It was found from NMR measurements [4] that, in the interval  $4.2 \text{ K} < T < T_N$ , the magnetic moments of the sublattices and the weak ferromagnetic moment show identical temperature dependences. This suggests that the value of angle  $\varphi$  is constant within the above-mentioned temperature interval.

In this paper, we study a FeBO<sub>3</sub> single crystal under high pressure by the nuclear forward scattering (NFS)

method, which is a version of Mössbauer spectroscopy on the time scale. The measurements were performed at the ID18/ID22N Nuclear Resonance beamlines [5] of the European Synchrotron Radiation Facility (ESRF, Grenoble, France).

High-quality transparent FeBO<sub>3</sub> crystals light green in color were grown from flux by V.N. Seleznev at the Simferopol' State University. They contained iron enriched with the <sup>57</sup>Fe isotope to 96%. The crystals had the form of plates whose large surfaces were parallel to the (111) basal plane. The thickness of the plates was 10–40  $\mu\text{m}$ , and the maximum area of a plate was  $8 \times 8 \text{ mm}^2$ .

To perform the NFS studies at high pressures, a <sup>57</sup>FeBO<sub>3</sub> crystal with the dimensions  $80 \times 40 \times 10 \mu\text{m}^3$  was placed into a high-pressure cell with diamond anvils. The time spectra of the NFS from the <sup>57</sup>Fe nuclei were recorded at room temperature in the pressure range up to 50 GPa without applying an external magnetic field. The (111) basal plane of the crystal was oriented perpendicularly to the synchrotron radiation (SR) beam, and the polarization vector of gamma rays was

parallel to the sample plane. At each fixed pressure value, two spectra were recorded; the first spectrum was obtained for the initial position of the crystal with the (111) plane arbitrarily oriented about the polarization direction of the SR beam (we will call it the “zero” orientation), and the second spectrum was obtained after the crystal was rotated in the basal plane through  $90^\circ$  from the initial position (the “90-degree” orientation).

Figure 1 presents the time spectra of NFS for different pressure values. The measurements were performed in the 16-bunch mode of operation. The decay of nuclear excitation is modulated in time by quantum and dynamical beats. The quantum beats are caused by the interference of the scattered radiation components with different frequencies as a result of the nuclear level splitting due to the hyperfine interaction. The period of quantum beats is inversely proportional to the hyperfine splitting and, in the case under study, to the magnetic field at the iron nuclei. The dynamical beats are caused by multiple scattering processes and determined by the sample thickness. A detailed description of the method can be found in review [6].

At pressures below 46 GPa the spectra display pronounced quantum beats. Their period is about 8 ns in the case of the zero azimuthal orientation of the crystal and about 15 ns in the case of the 90-degree orientation. The beats with the period 15 ns are 100%-modulated; i.e., at the nodes of beats, the scattered intensity drops practically to zero. These data indicate that, over the whole pressure range from normal to 46 GPa, the orientation of the magnetic field at the iron nuclei remains in the (111) basal plane, which is perpendicular to the radiation beam. When the pressure rises above 46 GPa, the quantum beats disappear, testifying to the disappearance of the hyperfine magnetic field at the  $^{57}\text{Fe}$  nuclei. At normal pressure, the NFS spectrum qualitatively coincides with the spectrum obtained for iron borate in [7]. A small difference between them is caused by different crystal thicknesses and by the absence of an external magnetic field in our measurements.

The spectra were processed by the MOTIF program developed by Yu.V. Shvyd'ko [8]. The large number of quantum beats in each spectrum (more than 15) allows one to obtain the value of magnetic field  $H^{\text{Fe}}$  at the  $^{57}\text{Fe}$  nuclei with high accuracy. The field  $H^{\text{Fe}}$ , being the main parameter of this study, is practically uncorrelated with other parameters of the spectrum such as the crystal thickness, the quadrupole splitting, and the azimuthal orientation of magnetic field in the (111) plane, which affect only the relative heights of individual peaks of quantum beats. For example, the measurements of the field  $H^{\text{Fe}}$  at the zero and 90-degree orientations of the crystal provide practically the same results.

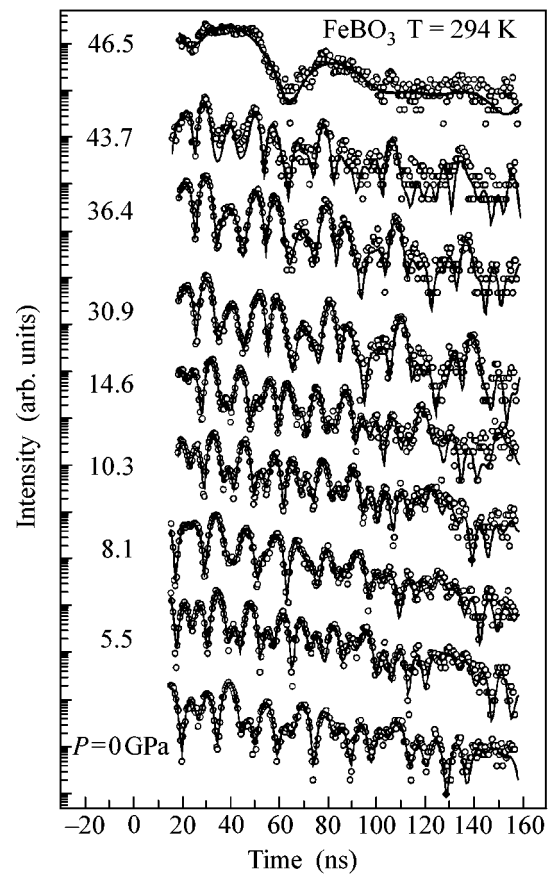


**Fig. 1.** Time spectra of resonance nuclear forward scattering from the  $^{57}\text{Fe}$  nuclei in a  $^{57}\text{FeBO}_3$  single crystal at room temperature. The dependence of the scattered radiation intensity on the time elapsed after the SR shot is represented on a logarithmic scale. The spectra are recorded for different pressures without applying an external magnetic field.

The pressure dependence of the hyperfine magnetic field  $H^{\text{Fe}}$  at an iron nucleus is shown in Fig. 2. In the pressure range  $0 < p < 44$  GPa, the field increases from 34.1 T at normal pressure to a maximal value of 48.1 T at  $p = 44$  GPa. With a further increase in pressure, at the point  $p = 46$  GPa, the magnetic field drops, pointing to an abrupt transition of the crystal from the antiferromagnetic to a nonmagnetic state. With this transition, the crystal, light green at normal pressure, darkens and becomes opaque. Presumably, this effect testifies to a drastic decrease in the optical absorption gap and implies a transition from the insulating to a metallic state.

From Fig. 2, one can see that the increase in the magnetic field with pressure up to 44 GPa is nonlinear and, presumably, is due to the increase in the exchange interaction owing to the decrease in the Fe–O–Fe interion distances. At normal pressure, the intersublattice exchange interaction between the nearest  $\text{Fe}^{3+}$  ions is dominant [9], and the exchange integral  $J$  evaluated in

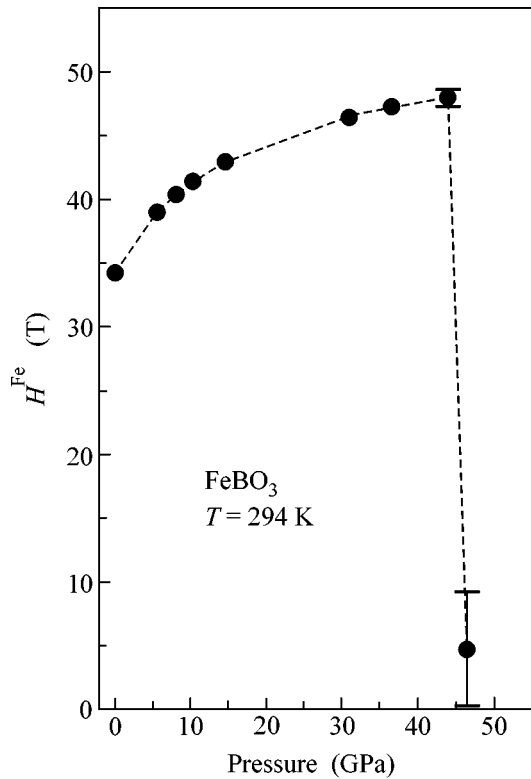


**Fig. 2.** Pressure dependence of the hyperfine magnetic field at the  $^{57}\text{Fe}$  nuclei in a  $^{57}\text{FeBO}_3$  single crystal at room temperature.

the approximation of spin-wave theory is equal to 27.3 K [9].

If we formally relate the increase in  $H^{\text{Fe}}$  to the increase in the Néel temperature  $T_N$ , we can estimate the pressure dependence of  $T_N$  from Fig. 2. For this purpose, we use the data on the temperature dependence of  $H^{\text{Fe}}$  [9] and assume that an increase in the field is equivalent to an increase in the Néel temperature. Dividing the curve shown in Fig. 2 into three approximately linear parts, we obtain  $dT_N/dp = 5.7$  K/GPa in the pressure interval  $0 < p < 6$  GPa,  $dT_N/dp = 2.3$  K/GPa in the interval  $6 < p < 15$  GPa, and  $dT_N/dp = 1.4$  K/GPa in the interval  $20 < p < 44$  GPa. We note that the value of  $dT_N/dp$  estimated for the first interval of low pressures is close to the value  $(5.3 \pm 0.3)$  K/GPa obtained from the magnetization measurements at hydrostatic pressures up to 0.3 GPa [10].

The most interesting effect is that the magnetic field at the iron nuclei abruptly disappears under pressures of about 46 GPa. This effect testifies to the transition of the  $^{57}\text{FeBO}_3$  crystal to a nonmagnetic state. We can propose several mechanisms for explaining such a magnetic collapse:

(1) A structural phase transition resulting in the formation of a new  $\text{FeBO}_3$  phase with the Néel point

below the room temperature. In this case, the magnetic transition at  $p = 46$  GPa is a Curie–Weiss-type transition from the antiferromagnetic to paramagnetic state.

(2) An insulator-to-metal transition at which the  $3d$  electrons of  $\text{Fe}^{3+}$  ions are delocalized and pass to the conduction band. In this case, the magnetic state of the material is determined by the band mechanism and depends on the features of the band structure. Then, the magnetic transition at  $p = 46$  GPa can be a Pauli-type transition from the antiferromagnetic to paramagnetic state.

(3) A transition of the iron ions from the high-spin to the low-spin state, analogous to the phenomenon that was recently observed in  $\text{LaFeO}_3$  orthoferrite in the pressure range 30–45 GPa [11]. In  $\text{FeBO}_3$  at normal pressure, the iron ions are trivalent and are in the high-spin state  $S = 5/2$ . The low-spin state  $S = 1/2$  of  $\text{Fe}^{3+}$  ions is not a diamagnetic one, but the Néel point of such a material should be much lower than for materials with  $\text{Fe}^{3+}$  ions in the high-spin state. For example, in the effective-field approximation, we have  $k_B T_N \propto AJS(S + 1)$ . In this case, the observed magnetic transition is a transition from the high-spin antiferromagnetic to the low-spin paramagnetic state.

In principle, we can also consider a change of the valence state of a  $\text{Fe}^{3+}$  ion to an even state,  $\text{Fe}^{2+}$  or  $\text{Fe}^{4+}$ . The low-spin states of such ions are diamagnetic. Then, the observed magnetic transition in  $\text{FeBO}_3$  can be a transition from the high-spin antiferromagnetic to the low-spin diamagnetic state.

In our NFS study, we did not intend to measure the isomer shifts (IS), which requires a more sophisticated measuring technique. The IS values can be obtained from the conventional Mössbauer absorption spectra, but their measurement in diamond anvils is a rather difficult problem. However, in order to study in more detail the possible mechanisms of magnetic transition and to obtain additional information on the valence and spin states of the iron ions, we are currently running such experiments. Their preliminary results point to a full coincidence of the dependences  $H^{\text{Fe}} = f(p)$  obtained by both methods in the pressure range  $0 < p < 35$  GPa.

In closing, we note that our data point to the orientation of the magnetic moments of the iron ions in the (111) plane of the crystal over the entire pressure range up to 46 GPa. Thus, the spin-flip transition, which was detected in an iron borate crystal at 1.7 GPa by magnetic neutron diffraction [12], did not occur in our crystal.

We are grateful to Professor R.Z. Levitin for useful discussions.

## REFERENCES

1. I. Bernal, C. W. Struck, and J. G. White, *Acta Crystallogr.* **16**, 849 (1963).
2. R. Wolff, A. J. Kurtzig, and R. C. LeCraw, *J. Appl. Phys.* **41**, 1218 (1970).
3. R. Diehl, *Solid State Commun.* **17**, 743 (1975).
4. M. P. Petrov, G. A. Smolenskiĭ, A. P. Pagurt, *et al.*, *Fiz. Tverd. Tela (Leningrad)* **14**, 109 (1972) [*Sov. Phys. Solid State* **14**, 87 (1972)].
5. R. Ruffer and A. I. Chumakov, *Hyperfine Interact.* **97/98**, 589 (1996).
6. G. V. Smirnov, *Hyperfine Interact.* **123/124**, 31 (1999).
7. T. Mitsui, S. Kitao, M. Seto, *et al.*, *J. Phys. Soc. Jpn.* **68**, 1049 (1999).
8. Yu. V. Shvyd'ko, *Phys. Rev. B* **59**, 9132 (1999).
9. M. Eibschütz and M. E. Lines, *Phys. Rev. B* **7**, 4907 (1973).
10. D. M. Wilson and S. Broersma, *Phys. Rev. B* **14**, 1977 (1976).
11. G. R. Hearne, M. P. Pasternak, R. D. Taylor, and P. Lacorre, *Phys. Rev. B* **51**, 11495 (1995).
12. V. P. Glazkov, V. V. Kvardakov, and V. A. Somenkov, *Pis'ma Zh. Éksp. Teor. Fiz.* **71**, 238 (2000) [*JETP Lett.* **71**, 165 (2000)].

*Translated by E. Golyamina*

# Percolation Nature of the Metal-to-Insulator Transition in $\text{La}_{0.8}\text{Ba}_{0.2}\text{MnO}_3$

R. V. Pomortsev, A. V. Korolev, V. E. Arkhipov, and V. P. Dyakina

Institute of Metal Physics, Ural Division, Russian Academy of Sciences, Yekaterinburg, 620219 Russia

e-mail: pomor@imp.uran.ru

Received May 30, 2001

For a  $\text{La}_{0.8}\text{Ba}_{0.2}\text{MnO}_3$  single crystal, the temperature dependences of its resistivity, magnetization, and differential magnetic susceptibility are studied in the vicinity of the metal-to-insulator transition and near the ferromagnetic-paramagnetic phase transition. The critical temperatures corresponding to these transitions are determined independently from the experiment. These temperatures are found to coincide within 2–3%. The results are discussed within the framework of percolation theory. © 2001 MAIK “Nauka/Interperiodica”.

PACS numbers: 71.30.+h; 64.60.Ak; 75.30.Kz; 75.60.-d; 75.50.Cc

The nature of the metal-to-insulator transitions in doped lanthanum manganites ( $\text{La}_{1-x}\text{B}_x\text{MnO}_3$ ), in which  $\text{La}^{3+}$  ions are partially replaced by bivalent ions (B) of some metal (specifically, by  $\text{Sr}^{2+}$ ,  $\text{Ca}^{2+}$ , or  $\text{Ba}^{2+}$ ), remains a topical problem despite the recent intensive studies of these systems [1–3]. By now, it is well known that, in doped manganites in the concentration interval  $0.16 < x < 0.4$ , a phase transition is observed from the low-temperature ferromagnetic phase with metallic conduction to the high-temperature paramagnetic phase that exhibits dielectric properties with the activation energy  $\Delta E$ . Such a behavior of manganites is quite unusual and can be explained only in general terms. Specifically, the appearance of the activation energy can be attributed to the presence of large polaron fluctuations in the paramagnetic phase [4, 5]. In the ferromagnetic phase, these fluctuations are strongly damped. However, the main point is that, in lanthanum manganites, in the region of the metal-to-insulator transition, the homogeneous state is unstable with a tendency to the phase layering into regions with metallic and dielectric properties [6–8]. In view of this fact, a better understanding of many experimental facts can be achieved by applying the methods developed for the theory of disordered media. For example, Gor'kov and Kresin [9, 10] have put forward an assumption that, in doped lanthanum manganites, the metal-to-insulator transitions due to the concentration variation, as well as to the temperature variation, are of a percolation nature. However, this hypothesis has not yet been reliably justified by experimental data. We are aware of only two publications [11, 12] lending some support to the percolation model.

In this paper, we study the temperature dependences of conductivity, magnetization, and differential magnetic susceptibility for the  $\text{La}_{0.8}\text{Ba}_{0.2}\text{MnO}_3$  compound over the temperature range 200–422 K. The Curie point

$T_C = 253.4$  K was determined from the analysis of the temperature dependence of the differential magnetic susceptibility, and the percolation transition temperature  $T_p$  was determined by using a newly proposed independent procedure, which provided the value  $T_p = 248.2$  K. Thus, the resulting values of  $T_p$  and  $T_C$  coincide within 2–3%.

All measurements described in this paper were made on the samples used in the previous experiments [13]. The samples were cut from a  $\text{La}_{0.8}\text{Ba}_{0.2}\text{MnO}_3$  single crystal grown by the floating zone method with zone heating by the radiation of a xenon lamp. The conductivity was determined by dc four-probe measurements. The magnetic measurements were performed with an MPMS-5XL SQUID magnetometer at the Magnetometry Center of the Institute of Metal Physics. The real  $\chi'$  and imaginary  $\chi''$  components of the dynamic magnetic susceptibility were measured in a magnetic field with amplitude  $H_m = 4$  Oe and frequency  $f = 80$  Hz.

Figure 1 presents the temperature dependence of the resistivity in the temperature interval 200–422 K. One can see that the resistivity exhibits a maximum at  $T_{\max}^p \approx 267$  K. To the left of the maximum, as the temperature grows smaller, the resistivity steeply decreases and, at  $T < 100$  K, reaches its minimum value  $\rho_M = 0.0019$   $\Omega$  cm. In the temperature region  $T > T_{\max}^p$ , the resistivity decreases with increasing temperature, according to the exponential law

$$\rho_D(T) = \rho_0 \exp(\Delta E/kT), \quad (1)$$

where  $\Delta E = 81.7$  eV and  $\rho_0 = 0.00222$   $\Omega$  cm (curve A). These values were determined by the linear interpolation of  $\ln \rho_D(T)$  as a function of  $T^{-1}$  in the temperature interval  $300 \leq T \leq 422$  K. It should be noted that the

activation energy  $\Delta E = 81.7$  meV determined in this way is much smaller than the typical manganite bandwidths and energy gaps, which, according to different estimates, are  $\sim 1$  eV [2]. In other systems, a similar situation is observed. For example, in  $\text{La}_{1-x}\text{Ca}_x\text{MnO}_3$  samples of like composition ( $x = 0.2$ ), the activation energy in the insulating state reaches 160 meV at high temperatures.

The simple percolation approach, which is essentially a macroscopic one, involves no specific details of the conduction mechanisms operating in different phases. It is sufficient to know the conductivity values for the metallic and insulating phases, their specific concentrations  $p$  and  $(1-p)$ , and the critical concentration of the metallic phase  $p_k$  corresponding to the formation of an infinite conducting cluster and to a sharp drop in resistivity. In our case, we observe a drastic change in the resistivity with varying temperature rather than concentration. Therefore, instead of the critical concentration, it is sufficient to determine the critical temperature  $T_p$  at which such a cluster is formed. For this purpose, we use the well-known relation from percolation theory, namely, the relation between the conductivity of a sample at  $p = p_k$  and the conductivities of each phase:

$$\sigma(p = p_k) = [\sigma_M]^u [\sigma_D]^{1-u}, \quad (2)$$

where  $u = s/(s+t)$  and  $s$  and  $t$  are the critical indices [14, 15].

Using this equality, one can easily derive the corresponding expression for the resistivity at the critical point  $T = T_p$ :

$$\rho(T_p) = [\rho_M]^u [\rho_D(T_p)]^{1-u}. \quad (3)$$

Here, we took into account that, in our case, the resistivity of the sample in the insulating state depends on temperature, while the resistivity in the metallic state is constant (curves A and B in Fig. 1). Actually, Eq. (3) is an equation for the determination of the quantity  $T_p$ .

To determine  $T_p$ , we use the following procedure. We define an auxiliary function  $f(T)$

$$f(T) = [\rho_M]^u [\rho_0]^{1-u} \exp[(1-u)\Delta E/kT] \quad (4)$$

and plot it in Fig. 1 (curve C). The point of intersection of the curves  $f(T)$  and  $\rho(T)$  (experimental curve) determines the desired critical temperature  $T_p$ . The plot was obtained with the following values of the quantities involved in Eq. (4):  $\rho_M = 0.0019$   $\Omega$  cm,  $\rho_0 = 0.00222$   $\Omega$  cm,  $\Delta E = 81.7$  meV, and the critical indices  $s = 0.7$  and  $t = 2.1$  [14]. With these values of  $s$  and  $t$ , the critical temperature was found to be  $T_p = 248.2$  K, which was almost 19 K lower than the temperature  $T_{\max}^p$ .

As was already noted above, the samples studied in our experiment possess ferromagnetic properties. From Fig. 2a, one can see that the susceptibility  $\chi'$  measured as a function of temperature in zero static field  $H$  exhib-

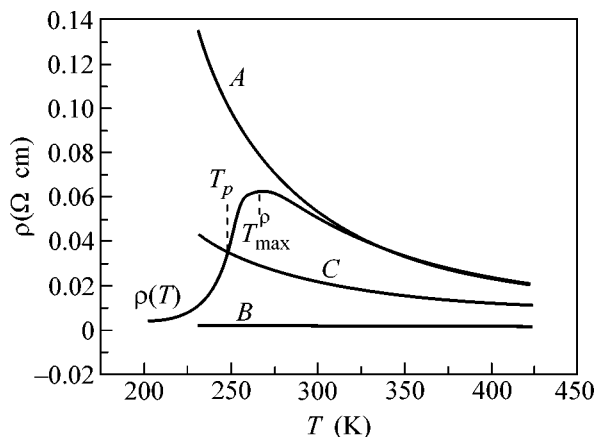


**Fig. 1.** Temperature dependence of the resistivity  $\rho(T)$  for a  $\text{La}_{0.8}\text{Ba}_{0.2}\text{MnO}_3$  single crystal near the metal-to-insulator transition. (A) Temperature dependence of the resistivity of the insulating phase, (B) the resistivity of the sample in the metallic state at  $T < 100$  K, and (C) the auxiliary curve determined by Eq. (4).

its a pronounced kink point corresponding to a critical temperature  $T_K$ . We note that, at all temperatures, the real part of the dynamic susceptibility  $\chi'$  is two or more orders of magnitude greater than the imaginary component  $\chi''$  ( $\chi' \gg \chi''$ ). Therefore, in the experiment under discussion, the susceptibility  $\chi'$  represents the differential reversible magnetic susceptibility. If we consider this experiment in the framework of the well-known concepts of the ferromagnetic–paramagnetic phase transition [16], we arrive at an apparent conclusion that  $T_K < T_C$ . We also note that the numerical value of the temperature  $T_K$  varies by several degrees when the magnetic field in the sample changes its direction. The analysis of this situation leads to the conclusion that the kink method provides the estimate of  $T_C$  only to a first approximation. At the same time, some doubts are cast upon the error in the determination of  $T_C$  because of the following important circumstance. In the experiment under discussion, at the point  $T_K$ , we have not a second-order phase transition of the order–disorder type but a fundamentally different transition, namely, the transition of a multidomain sample to a single-domain state. In fact, this is a transition caused by the variation of the magnetic field  $H$ , which occurs in much the same way as the magnetization of the sample near the kink point of the isotherm  $M(H)$  when it attains saturation. It is this fact which causes difficulties and ambiguity in the interpretation and processing of the results of such experiments. It can easily be shown that similar measurements performed on a sample in a single-domain state can fully eliminate the ambiguity in the determination of  $T_C$ .

To take the sample to the single-domain state, it is necessary to place it in a sufficiently strong static magnetic field  $H > NH_s$ , where  $N$  is the demagnetizing fac-

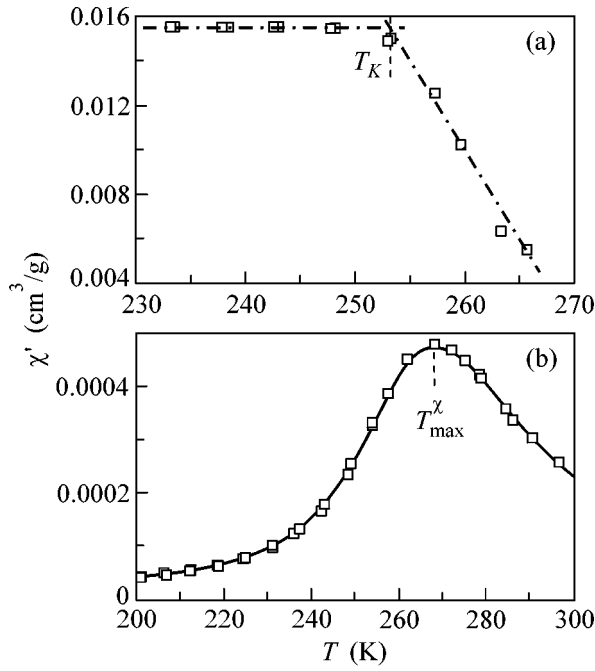


**Fig. 2.** Portions of the temperature dependence of the magnetic susceptibility  $\chi'$  for a C single crystal at  $H =$  (a) 0 and (b)  $10^4$  Oe.

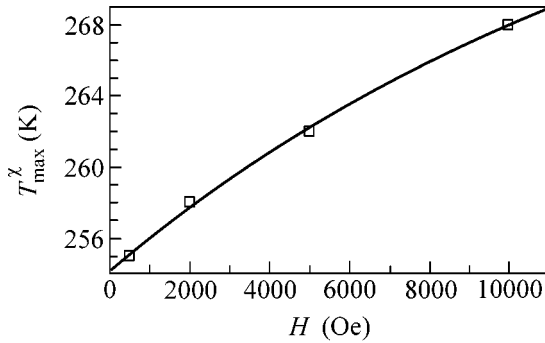


**Fig. 3.** Temperature  $T_{\max}^{\chi}$  corresponding to the maximum of magnetic susceptibility vs. static magnetic field  $H$ .

tor of the sample and  $M_S$  is its spontaneous magnetization. For a typical ferromagnetic sample, it can be shown that, in the single-domain state, the temperature dependence of  $\chi'$  at  $H = \text{const}$  will have a single maximum at  $T = T_{\max}^{\chi}$ , where  $T_{\max}^{\chi} > T_C$ . This can be seen from Fig. 2b in which the temperature dependence  $\chi'(T)$  obtained for  $H = \text{const}$  exhibits the above-mentioned single maximum. We note that our measurements were successful solely because of the use of a SQUID magnetometer. To determine the value of  $T_C$ , we measured  $\chi'(T)$  for different values of magnetic field and plotted the dependence of  $T_{\max}^{\chi}$  on  $H$  (Fig. 3). The

resulting  $T_{\max}^{\chi}(H)$  curve allows the value of  $T_C$  to be determined as a point of intersection of this curve with the ordinate axis.

By processing our experimental data, we found that the maximum value of  $T_K$  was  $T_K = 252.5$  K and that  $T_{\max}^{\chi}(H = 0) = 254.2$  K. Thus, the Curie point  $T_C = 253.4$  K can be estimated as the mean of the two above-mentioned temperatures,  $T_K$  and  $T_{\max}^{\chi}(H = 0)$ , with a reasonable error of  $\pm 1$  K.

The percolation picture of the behavior of resistance as a function of temperature would be incomplete without the determination of the critical behavior of resistance as a function of  $(T_p - T)$ . Evidently, in the case under study, the critical index can be determined only in the temperature region below  $T_p$ , because at  $T > T_p$  the critical behavior of  $\rho(T - T_p)$  is masked by a strong temperature dependence of the insulating phase. Therefore, we restrict our consideration to the region  $T < T_p$  and plot the dependence of the resistivity on the reduced temperature  $(T_p - T)/T_p$  (Fig. 4). If the resistance of the insulating phase were infinitely large, the critical behavior of  $\rho(T_p - T)$  would extend to  $T \rightarrow T_p$ . In our case, the resistivity of the insulating phase is finite, and, therefore, in the vicinity of  $T_p$  (i.e., near zero in Fig. 4), we have a crossover region [16], the study of which is beyond the scope of this paper. In the classical percolation theory, the critical behavior occurs in the region bounded by the condition  $\varepsilon^{s+t}h > 1$ , where  $\varepsilon = (p_k - p)/p_k$  and  $h = (\sigma_D/\sigma_M) \ll 1$ . To estimate the boundary of the region where the critical behavior of the resistivity can be observed, we use the following approach. We assume that  $(p_k - p)/p_k \propto (T_p - T)/T_p$ . In this case, one can easily see that the region of the critical behavior of resistivity is determined by the condition

$$(1 - T/T_p)^{s+t}(\rho_D/\rho_M) > 1, \quad (5)$$

which is satisfied for  $T < 223.6$  K. The critical index  $\mu$  determined in the temperature interval  $201.4 < T < 223.6$  K was found to be equal to  $-0.8$  [10]. In other words, below 223.6 K the behavior of  $\rho$  can be represented in the form

$$\rho \propto (T_p - T)^{-0.8}. \quad (6)$$

From Fig. 4 (see the inset), one can see that the temperature dependence of the resistivity obtained for the  $\text{La}_{0.8}\text{Ba}_{0.2}\text{MnO}_3$  samples fits relation (6) with reasonable accuracy. The critical index  $\mu = -0.8$  determined by us agrees satisfactorily with the value  $\mu = -0.6$  obtained by Gor'kov [10] from the analysis of the critical behavior of both the magnetic hardness coefficient and the magnetization for the  $\text{La}_{0.8}\text{Ba}_{0.2}\text{MnO}_3$  samples.

In closing, we summarize our results. We performed an independent determination of two different critical temperatures, namely, the critical temperature corresponding to the metal-to-insulator transition  $T_p =$

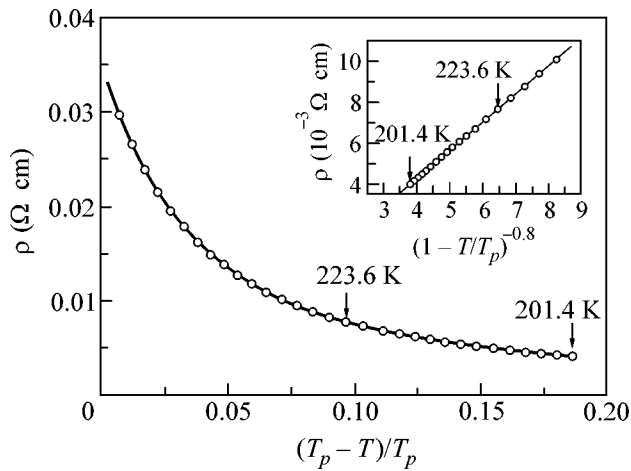


**Fig. 4.** Experimental dependence of the resistivity of  $\text{La}_{0.8}\text{Ba}_{0.2}\text{MnO}_3$  on the reduced temperature  $(T_p - T)/T_p$  in the temperature interval  $201.4 \leq T \leq 248$  K. The inset shows the resistivity vs.  $(1 - T/T_p)^{-0.8}$  in the temperature interval 201.4–223.6 K.

248.2 K and the critical temperature of the magnetic transition  $T_C = 253.4$  K. These temperatures proved to be close to each other. In our opinion, their coincidence within 2–3% is not accidental but is a consequence of the fact that, in the high-temperature region, the  $\text{La}_{1-x}\text{Ba}_x\text{MnO}_3$  system with  $x = 0.2$  is a two-phase disordered system consisting of an insulating matrix containing ferromagnetic metal inclusions. When the temperature decreases, both transitions exhibit a percolation nature, and the data obtained from the experiment justify the Gor'kov and Kresin [9, 10] hypothesis for the nature of the metal-to-insulator transitions in doped lanthanum manganites.

This work was supported by the Russian Foundation for Basic Research, project no. 99-02-16280.

## REFERENCES

1. *Colossal Magnetoresistance, Charge Ordering, and Related Properties of Manganese Oxides*, Ed. by C. N. R. Rao and B. Raveau (World Scientific, Singapore, 1998).
2. *Colossal Magnetoresistance Oxides*, Ed. by Y. Tokura (Cordon & Breach, London, 1999).
3. M. Imada, A. Fujimori, and Y. Tokura, *Rev. Mod. Phys.* **70**, 1039 (1998).
4. A. J. Millis, R. Mueller, and B. I. Shraiman, *Phys. Rev. B* **54**, 5389 (1996).
5. H. Roder, J. Zang, and A. R. Bishop, *Phys. Rev. Lett.* **76**, 1356 (1996).
6. S. Yunoki, J. Hu, A. L. Malvezzi, *et al.*, *Phys. Rev. Lett.* **80**, 845 (1998).
7. D. Khomskii, *Physica B (Amsterdam)* **280**, 325 (2000).
8. M. Yu. Kogan, D. I. Khomskii, and M. V. Mostovoy, *Eur. Phys. J. B* **12**, 217 (1999).
9. L. P. Gor'kov and V. Z. Kresin, *Pis'ma Zh. Éksp. Teor. Fiz.* **67**, 934 (1998) [*JETP Lett.* **67**, 985 (1998)].
10. L. P. Gor'kov, *Usp. Fiz. Nauk* **168**, 665 (1998) [*Phys. Usp.* **41**, 589 (1998)].
11. V. Podzorov, M. Uehara, M. E. Gershenson, *et al.*, *Phys. Rev. B* **61**, R3784 (2000).
12. M. Mayr, A. Moreo, J. A. Verges, *et al.*, *cond-mat/0007480*.
13. V. E. Arkhipov, V. G. Gaviko, K. M. Demchuk, *et al.*, *Pis'ma Zh. Éksp. Teor. Fiz.* **71**, 169 (2000) [*JETP Lett.* **71**, 114 (2000)].
14. V. I. Shklovskii and A. L. Éfros, *Electronic Properties of Doped Semiconductors* (Nauka, Moscow, 1979; Springer-Verlag, New York, 1984).
15. A. L. Éfros and V. I. Shklovskii, *Phys. Status Solidi B* **76**, 475 (1976).
16. I. K. Kamilov and Kh. K. Aliev, *Usp. Fiz. Nauk* **140**, 639 (1983) [*Sov. Phys. Usp.* **26**, 696 (1983)].

Translated by E. Golyamina

# Ionization of an Exciton Moving Perpendicular to a Magnetic Field in the GaAs/Al<sub>x</sub>Ga<sub>1-x</sub>As Superlattice

B. P. Zakharchenya and V. F. Sapega

*Ioffe Physicotechnical Institute, Russian Academy of Sciences, St. Petersburg, 194021 Russia*

*e-mail: bpz@solstate.ioffe.rssi.ru*

Received May 23, 2001; in final form, May 31, 2001

The magnetic field effect on the spectrum of excitons associated with various minibands in superlattices was studied by resonance Raman spectroscopy. It was found that the intensity of Raman scattering by acoustic phonons with the participation of the ground state of an exciton associated with the second miniband is sharply reduced even in weak magnetic fields if its velocity vector is orthogonal to the external magnetic field. This phenomenon was explained by the ionization of the exciton in the electric field arising in the system of coordinate associated with the exciton moving perpendicular to the external magnetic field. © 2001 MAIK "Nauka/Interperiodica".

PACS numbers: 71.35.Ji; 75.70.Cn

The quasiparticle spectrum of an exciton changes in a magnetic field for several reasons. First, there is a common Zeeman splitting, which was observed in exciton lines in a semiconductor in 1954 [1]. Second, there is a diamagnetic shift of exciton levels due to the acceleration of exciton motion in the magnetic field, which was found in 1956 [2] and was observed thereafter for both bulk semiconductors and quantum-size structures.<sup>1</sup> Third, a rearrangement of energy levels of an exciton may occur as a result of the motion of the quasiparticle excited by a photon with a momentum  $k = (\omega/c)n$  ( $n$  is the refractive index of the crystal) directed perpendicular to the magnetic field  $H$ . In this case, an electric field

$$\mathbf{E} = \frac{1}{c}[\mathbf{V}_{ex} \times \mathbf{H}], \quad (1)$$

where  $\mathbf{V}_{ex}$  is the velocity of the exciton, will appear in the system of coordinates associated with the moving exciton.

A situation arises when the external magnetic field and the electric field given by Eq. (1) turn out to be crossed, and the quasiparticle spectrum is rearranged. A manifestation of the electric field determined by Eq. (1) was observed experimentally in [4] for excitons in a cadmium sulfide crystal, in which the center of inversion is absent.

The effect of an electric field given by Eq. (1) on luminous hydrogen atoms (canal rays) moving perpendicular to a magnetic field was observed by Wilhelm

Wien as early as 1916 [5]; Wien named the corresponding splitting of the Balmer lines electrodynamic splitting. Wien's remarkable experiment has been forgotten. It is not mentioned in either textbooks or original papers. At the same time, Wien in the cited work predicted even the possibility of observing electrodynamic changes in the energy spectra of spatial objects. Such calculations are carried out now for neutron stars, where magnetic fields reach values of  $10^{11}$ – $10^{12}$  G [6].

In this work, the effect of a magnetic field on the spectrum of excitons in the GaAs/Al<sub>x</sub>Ga<sub>1-x</sub>As superlattice (SL) was studied by resonance Raman scattering by acoustic phonons for various orientations of the magnetic field relative to the direction of SL growth, that is, relative to the exciton velocity vector. We found that an exciton associated with the first electron and hole minibands in a magnetic field exhibits only a diamagnetic shift of the ground state energy regardless of the orientation of its group velocity vector relative to the magnetic field. An exciton associated with the second electron and hole minibands also exhibits a diamagnetic shift; however, the character of the magnetic field effect on the exciton state strongly depends on the mutual orientation of the magnetic field and the direction of the exciton motion. The line of Raman scattering associated with the ground state of an exciton moving perpendicular to the magnetic field disappears in magnetic fields, in contrast to the case when an exciton is moving along the magnetic field. This effect is explained by exciton ionization in the electric field determined by Eq. (1).

The experiments were carried out with undoped GaAs/Al<sub>0.05</sub>Ga<sub>0.95</sub>As SLs. The widths of quantum wells

<sup>1</sup> A diamagnetic shift for atomic orbitals of a giant radius was observed in 1939 [3].

(QWs) and barriers were fixed at  $60 \text{ \AA}$  each. Photoluminescence and Raman scattering by acoustic phonons were excited by a tunable titanium–sapphire laser pumped by an argon ion laser. The pumping density was  $1 \text{ W/cm}^2$ , which allowed us to avoid heating the sample. Photoluminescence was measured by a double grating SPEX 1404 monochromator equipped with a GaAs photomultiplier with a photon counting system. The experiments were carried out at a sample temperature  $T = 4 \text{ K}$  and in magnetic fields  $B \leq 14 \text{ T}$  in the Voigt (the magnetic field lies in the plane of SL layers and perpendicular to the exciting photon wave vector  $\mathbf{k}_{ph}$ ) or Faraday (the magnetic field is aligned with the direction of SL growth and the photon wave vector) geometry. In both cases, the backscattering geometry was used.

The energy spectrum (dispersion in the direction of SL growth) of the SL under study consists of electron and hole minibands whose structure is shown schematically in Fig. 1 as thin lines. Each of those minibands is associated with exciton states  $X_1$  and  $X_2$ , which appear in Fig. 1 as heavy lines. Choosing the energy of the exciting light (vertical arrows in Fig. 1), one can resonantly excite an exciton that belongs to the first or the second miniband (the transition diagram is shown in Fig. 1) with a wave vector  $K_z$  at a distance of 0.1 from the edges of the SL Brillouin zone. The edge photoluminescence spectrum of the SL under study is formed from the narrow line of the free exciton (marked with the symbol  $X_1$  in Fig. 2) associated with the first electron and hole (miniband of heavy holes) minibands. In a magnetic field, this line shifts toward the high-energy region both in the Faraday (circles in Fig. 2; the splitting of this line into two Zeeman components is negligibly small compared to the shift of their center of gravity and, therefore, is not taken into account subsequently) and in the Voigt (triangles in Fig. 2) geometry. The displacement of this line in a magnetic field is due to the diamagnetic shift. The weak shoulder  $X'_1$  in the photoluminescence (PhL) spectrum located on the high-energy side of the  $X_1$  line is possibly due to the recombination of excitons associated with the band of light holes, because it exhibits a diamagnetic shift comparable with the diamagnetic shift of exciton  $X_1$ . The magnetic field dependence of this state for the Faraday (circles) and Voigt (triangles) geometries is also presented in Fig. 2.

The magnetic field effect on the excited states of an exciton of the first electron and hole minibands was studied using magneto-Raman spectra. This technique was successfully used for studying Landau levels or Stark localization [7–10] and allowed states to be detected that were not observed in conventional photoluminescence spectra even at very high pumping. For each excitation energy, the spectrometer was used as a filter whose passband was shifted by  $4 \text{ cm}^{-1}$  toward the Stokes region. The scattered light intensity was measured under these conditions as a function of the mag-

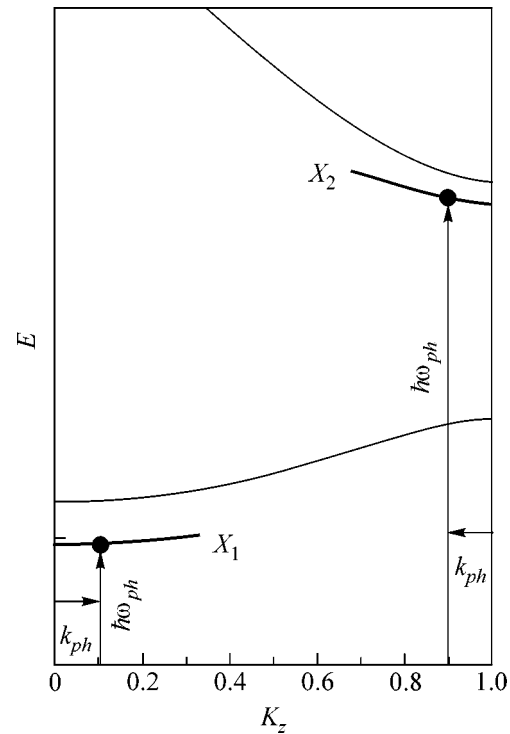


**Fig. 1.** Dispersion of electron and hole minibands (thin solid lines) and associated exciton states (heavy lines) in the direction of SL growth. Vertical arrows designate the optical excitation of excitons by photons with energy  $\hbar\omega_{ph}$  and wave vector  $k_{ph}$ .

netic field. Such magneto-Raman spectra are sensitive to all the electronic states for which the incoming or outgoing resonance conditions of the Raman process are fulfilled. The advantage of light scattering by acoustic phonons is that resonances are studied at small Raman shifts. Moreover, the double resonance conditions are almost always obeyed for phonons with energies lower than the homogeneous broadening, which leads to a considerable increase in the intensity of scattered light. The fan plot of electron–hole states in a magnetic field obtained in this way is presented in Fig. 2 as light circles for the Faraday geometry and as light triangles for the Voigt geometry. Note that the ground states  $X_1$  and the excited state  $X'_1$  were also observed in the magneto-Raman spectra, and their dependence on the magnetic field coincided with the dependence measured from the PhL spectra. The states of magnetoexcitons observed upon excitation by photons with the energy  $\hbar\omega_{ph} = 1.55\text{--}1.62 \text{ eV}$  are extrapolated to a state of the exciton continuum of the first electron and hole minibands at  $B \rightarrow 0$ . The difference in the magnetic field dependence of the electron and hole states associated with the Landau levels with  $n = 1, 2$  in the Faraday and Voigt geometries is due to the anisotropy of the cyclotron mass of electrons and holes in the SL. However, the main contribution is apparently due to the anisotropy of the heavy hole mass. The states of

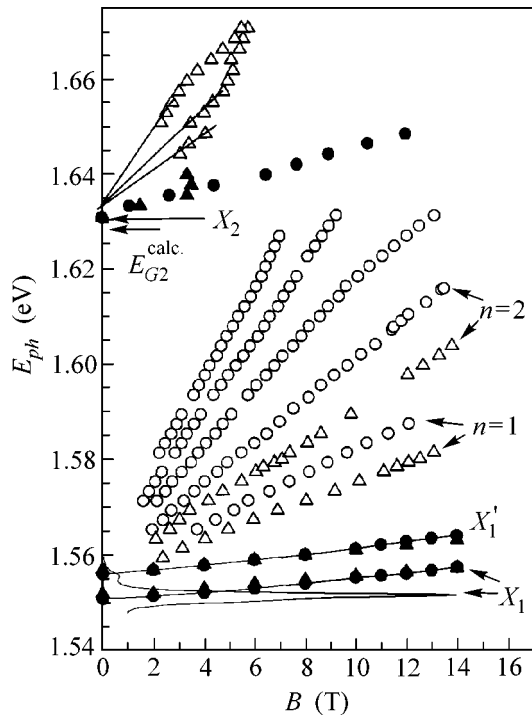


**Fig. 2.** Magnetic field dependence of the ground state energy of excitons of the first  $X_1$  and the second  $X_2$  minibands in the Faraday (circles) and the Voigt (triangles) geometry; magnetic field dependence of the Landau levels for the Faraday (light circles) and the Voigt (light triangles) geometry. The horizontal arrow indicates the calculated values of the energy between the bottom of the second electron miniband and the top of the corresponding valence miniband.

the diamagnetic exciton observed upon light excitation with the energy  $\hbar\omega_{ph} \geq 1.63$  eV are extrapolated to the ground state energy of an exciton associated with the second electron and hole minibands. The energy of this state is close to the energy between the bottom of the second electron miniband and the top of the second hole miniband calculated within the Kronig–Penny model [11] (the calculated energy value is marked in Fig. 2 with a horizontal arrow denoted by the symbol  $E_{G2}^{calc}$ ). In contrast to the ground state of the diamagnetic exciton associated with the first miniband, the ground state of the diamagnetic exciton associated with the second miniband behaves differently in the Faraday (circles) and Voigt (triangles) geometries. In the Faraday geometry, the diamagnetic shift of the exciton state  $X_2$  is considerably larger than the diamagnetic shift of the exciton  $X_1$  and is observed in the magneto-Raman spectrum up to high magnetic fields  $B \sim 14$  T. In the Voigt geometry in fields  $B \leq 3$ , the state of the exciton  $X_2$  exhibits the same diamagnetic shift as in the Faraday geometry; however, the intensity of the Raman process with the participation of this exciton decreases sharply in fields  $B > 3$  T. The decrease in the intensity of the Raman process with the participation of exciton  $X_2$  is

evidently due to the decrease in its lifetime. The state of exciton  $X_2$  is intermediate in the process of resonance Raman scattering by acoustic phonons and, therefore, determines its probability [12]. We believe that the ionization of exciton  $X_2$  is the main reason for the decrease in its lifetime.

Let us discuss the behavior of the ground states of the  $X_1$  and  $X_2$  excitons in the Faraday and Voigt geometries. It is evident that a photoexcited exciton in the resonance Raman process acquires (by virtue of the momentum conservation law) a quasi-momentum  $\hbar\mathbf{K}_x = \hbar\mathbf{k}_{ph}$  (where  $k_{ph} = (\omega/c)n$  is the photon momentum in a SL with the refractive index  $n$ ) from the exciting photon. Correspondingly, the directed exciton velocity  $\mathbf{V}_x = \hbar\mathbf{K}_x/M$  ( $M$  is the kinetic exciton mass) is either aligned with (Faraday geometry) or perpendicular to (Voigt geometry) the magnetic field. An exciton moving along the magnetic field direction,  $\mathbf{V}_x \parallel \mathbf{B}$ , exhibits a diamagnetic shift in energy (this shift is due to the magnetic field effect only on the relative motion of the electron and the hole in the exciton) and an increase in the oscillator strength. An exciton moving perpendicular to the magnetic field,  $\mathbf{V}_x \perp \mathbf{B}$ , also exhibits a diamagnetic shift. However, as was already mentioned above, an electric field arises in this geometry

$$\mathbf{E} = \frac{1}{c}[\mathbf{V}_x \times \mathbf{B}].$$

It is evident that the exciton interaction energy with this electric field at sufficiently high exciton velocities and sufficiently high magnetic fields can exceed its binding energy, which will be manifested in the ionization of the exciton. It is with this phenomenon that we associate the disappearance of the line of resonance Raman scattering with the participation of exciton  $X_2$  in the Voigt geometry in fields  $B \sim 4$  T. An estimate shows that a photoexcited exciton has a velocity perpendicular to the magnetic field  $V_x \sim 10^6$  cm/s (in the calculation of  $V_x$ , we used the mass of exciton motion along the SL  $M_{\parallel} = m_{hh} + m_e = 0.4m_0$  [13]). An electric field with a strength  $E_B \sim 400$  V/cm arises in the system of coordinates moving with this velocity perpendicular to a magnetic field  $B \sim 4$  T. It is known that an exciton in bulk GaAs with the binding energy  $E_X \sim 4$  meV is already ionized in a fairly weak constant external electric field  $E \sim 1000$  V/cm [13]. It may be expected that the binding energy of exciton  $X_2$  in the second miniband in the SL is lower than the binding energy of exciton  $X_1$  in the first miniband, which, in turn is found to be close to the binding energy of an exciton in bulk GaAs. Therefore, the exciton becomes ionized in lower electric fields.

At first glance, the ionization of exciton  $X_1$  associated with the first miniband in the Voigt geometry should be observed in a similar way. In fact, the quasi-momentum of this exciton is only slightly smaller than that of the  $X_2$  exciton ( $K_{X_1}/K_{X_2} = 0.95$ ); however, the

velocities of the  $X_1$  and  $X_2$  excitons can differ significantly because of the great difference in the effective masses. This difference in masses is mainly determined by the heavy hole and is associated with the SL parameters. A calculation made in the Kronig–Penny model indicates that the width of the first hole miniband  $\Delta E_{hh}^{(1)} = 2$  meV, whereas the second miniband has the width  $\Delta E_{hh}^{(2)} = 12$  meV and lies entirely in the overbarrier region. It is evident that the hole mass in the first miniband in the direction of SL growth in the tight-binding approximation  $m_{hh} \propto 1/\Delta E_{hh}^{(1)}$  and, thus, can be notably larger than the mass in the second miniband, which can be taken equal to the hole mass in bulk GaAs. The conclusion that the mass of the heavy hole in the direction of SL growth is notably larger than its mass in bulk GaAs is confirmed by the fact that the magnetic field dependence of the Landau levels of the first miniband in the Voigt geometry is considerably weaker than this dependence in the Faraday geometry.

The authors are grateful to Dr. K. Eberl for manufacturing the superlattice and for useful discussions. V.F.S. is grateful to Prof. M. Cardona for providing the possibility of carrying out experiments in his laboratory and to Max Planck Gesellschaft for financial support.

This work was supported by the Russian Foundation for Basic Research, project no. 00-15-96756.

## REFERENCES

1. E. F. Gross and B. P. Zakharchenya, Dokl. Akad. Nauk SSSR **99**, 527 (1954).
2. E. F. Gross and B. P. Zakharchenya, Dokl. Akad. Nauk SSSR **111**, 564 (1956) [Sov. Phys. Dokl. **1**, 678 (1957)]; E. F. Gross and B. P. Zakharchenya, J. Phys. Radium **1**, 68 (1957).
3. F. Jankins and E. Segre, Phys. Rev. **55**, 52 (1939).
4. U. F. Gross, B. P. Zakharchenya, and O. V. Konstantinov, Fiz. Tverd. Tela (Leningrad) **3**, 305 (1961) [Sov. Phys. Solid State **3**, 221 (1961)].
5. W. Wien, Ann. Phys. (Leipzig) **49**, 842 (1916).
6. A. Y. Potekhin, J. Phys. B **27** (6), 1073 (1994).
7. V. F. Sapega, V. I. Belitsky, T. Ruf, *et al.*, Phys. Rev. B **46**, 16005 (1992).
8. D. N. Mirlin, I. A. Merkulov, V. I. Perel', *et al.*, Solid State Commun. **82**, 305 (1992).
9. G. Goldoni, T. Ruf, V. F. Sapega, *et al.*, Phys. Rev. B **51**, 14542 (1995).
10. V. F. Sapega, T. Ruf, M. Cardona, *et al.*, Phys. Rev. B **56**, 1041 (1997).
11. G. Bastard, Phys. Rev. B **25**, 7584 (1982).
12. T. Ruf, J. Spitzer, V. F. Sapega, *et al.*, Phys. Rev. B **50**, 1792 (1994).
13. D. C. Reynolds and T. C. Collins, in *Excitons* (Academic, New York, 1981), p. 138, and references therein.

*Translated by A. Bagatur'yants*

# Antiferromagnetic Exchange Mechanism of Superconductivity in Cuprates

N. M. Plakida

Joint Institute for Nuclear Research, Dubna, Moscow region, 141980 Russia

e-mail: plakida@thsun1.jinr.ru

Received May 14, 2001; in final form, May 31, 2001

The theory of superconducting pairing due to antiferromagnetic exchange is considered. The strong dependence of the superconducting transition temperature  $T_c$  on the lattice constant  $a$  observed recently in mercury superconductors is explained within the framework of this theory. Calculations have been performed based on the two-band  $p$ - $d$  Hubbard model in the strong correlation limit. The large excitation energy  $\Delta_{pd}$  for the antiferromagnetic exchange of two particles from different Hubbard subbands results in the suppression of the retardation effects and in the pairing of all the particles in the conduction subband with the Fermi energy  $E_F \ll \Delta_{pd}$ :  $T_c \approx E_F \exp(-1/\lambda)$ , where  $\lambda \propto J$ . The dependence  $T_c(a)$  and the isotope effect are explained by the dependence of the exchange interaction  $J$  on  $a$  and on zero-point vibrations of oxygen ions. © 2001 MAIK "Nauka/Interperiodica".

PACS numbers: 74.20.-z; 74.72.-h

1. A distinctive feature of high- $T_c$  copper oxide (cuprate) superconductors is strong antiferromagnetic (AFM) exchange interaction (see, for example, [1]). The exchange binding energy of two holes with spin 1/2 in copper  $\text{Cu}(3d^9)$  and oxygen  $\text{O}(2p^5)$  ions has a value on the order of 1 eV, and the indirect (through oxygen ions) AFM exchange energy of holes in copper ions is on the order of 0.13 eV. If cuprates had a three-dimensional network of bonds for copper spins, the AFM Néel temperature in these materials could reach a record value  $T_N \approx 1500$  K. However, because of the two-dimensional character of the spin lattice in the  $\text{CuO}_2$  plane, the Néel temperature turns out to be much lower,  $T_N \approx 300$ – $500$  K. Note for comparison that the maximum Néel temperature  $T_N \approx 1040$  K is observed for vanadium sulfide (VS).

A certain confirmation of the particular importance of the AFM exchange in superconducting pairing in cuprates was obtained in recent experiments on studying the dependence of the superconducting transition temperature  $T_c$  on the interatomic copper–oxygen distance in mercury superconductors (see [2] and references therein). It is known that the maximum temperature reached in mercury  $\text{HgBa}_2\text{Ca}_{n-1}\text{Cu}_n\text{O}_{2n+2+\delta}$  ( $\text{Hg-12}(n-1)n$ ) superconductors is  $T_c \approx 135$  K, which can be increased up to 150 K by the action of an external pressure. These results can be explained by the structural features of mercury superconductors, in which the  $\text{CuO}_2$  plane exhibits the least distortion (buckling): the Cu–O bond angle is close to  $180^\circ$ , which provides the maximum value of the indirect AFM interaction. Under the action of an external pressure, the Cu–O bond lengths are decreased, which leads

to a further increase in the magnitude of the AFM exchange interaction. The doping of mercury superconductors by fluorine rather than oxygen gave evidence of the interrelation between the increase in  $T_c$  and the decrease in the Cu–O bond in the plane. The fluorination of Hg-1201 superconductors results in a significant change in the copper–apical oxygen bond length with unchanged Cu–O distance in the plane and with retaining the maximal  $T_c \approx 97$  K, whereas the fluorination of Hg-1223 results in a change in the Cu–O bond length in the plane (with no significant change in the bond angle) and increases  $T_c$  by 3 K [2]. Comparing the available data, the authors [2] came to the conclusion that the superconducting transition temperature at the optimal doping  $T_c(\delta_{\text{opt}})$  depends linearly on the lattice constant  $a$  (the Cu–O–Cu distance in the plane) with the coefficient  $dT_c/da \approx -1.35 \times 10^3$  K/Å. Close results were obtained for epitaxial  $\text{La}_{1.9}\text{Sr}_{0.1}\text{CuO}_4$  films:  $dT_c/da \approx -1.0 \times 10^3$  K/Å [3]. The increase in  $T_c$  due to the action of a hydrostatic pressure is an order of magnitude lower because of the buckling of the  $\text{CuO}_2$  plane and a decrease in the Cu–O bond angle, which always accompany the compression.

In this work, I give an explanation for the experimental results obtained, assuming that the mechanism of superconducting pairing in cuprates is determined by indirect antiferromagnetic exchange. The isotope effect in cuprates upon the substitution of  $^{18}\text{O}$  for  $^{16}\text{O}$  is explained within the same approach. It is also noted that pairing through the AFM exchange possesses a number of features that lead to  $d$ -wave pairing with a high  $T_c$ . The results obtained allow the conclusion that

the AFM exchange is the determining factor in superconducting pairing in cuprates.

2. The particular importance of the AFM exchange interaction in cuprates was noted by Anderson [4], who proposed the theory of resonant valence bonds within the framework of the one-band  $t$ - $J$  model. However, the use of the mean field approximation within the framework of the slave boson theory [4], as well as the further development of the spinon-holon theory, gave no convincing evidence in favor of the AFM exchange as the mechanism of high- $T_c$  superconductivity (see [5]). Subsequently, superconducting pairing due to the AFM exchange within the framework of the  $t$ - $J$  model was considered in many studies (see the review [6] and, for example, [7, 8] and references therein).

Superconductivity within the more general two-band  $p$ - $d$  model was considered in the recent work [9], where it was shown that the results obtained within the framework of the  $t$ - $J$  model with the instant exchange interaction remain true even when taking into account the retardation effects in the two-band model. Therefore, in order to determine the  $dT_c/da$  dependence and to estimate the isotope effect, I can restrict myself to calculating  $T_c$  in the one-band  $t$ - $J$  model using, however, its parameters calculated within the framework of the two-band  $p$ - $d$  model. Therefore, I will briefly outline this method of calculations below.

The strong AFM exchange interaction in cuprates is due to the two factors: the large value of  $pd\sigma$  hybridization  $t_{pd} \approx 1.5\text{eV}$  for the  $3d$  states of copper and the  $2p$  states of oxygen and the small splitting energy of their atomic levels  $\Delta_{pd} \approx 3\text{eV}$ . At the same time, strong Coulomb correlations for the  $3d$  states of copper  $U_d \approx 8\text{eV}$  considerably increase the energy of the two-hole  $3d$  states. Because of this fact, a dielectric phase arises in undoped cuprates, and a metallic phase appears upon doping the singlet  $p$ - $d$  hole band lying below the triplet band [10]. These features of the electronic spectrum of holes in the  $\text{CuO}_2$  plane (the main structural element of cuprates) can be described within the framework of the simple model  $p$ - $d$  Hamiltonian [11]

$$H = \sum_{i\sigma} \{ \epsilon_d \tilde{d}_{i\sigma}^+ \tilde{d}_{i\sigma} + \epsilon_p c_{i\sigma}^+ c_{i\sigma} \} + \sum_{i,j,\sigma} V_{ij} \{ \tilde{d}_{i\sigma}^+ c_{j\sigma} + \text{h.c.} \}. \quad (1)$$

Operators  $\tilde{d}_{i\sigma}^+$  and  $c_{i\sigma}^+$  describe the creation of one-hole  $d$  and  $p$  states at sites  $i$  of the square lattice in the  $\text{CuO}_2$  plane with the energies  $\epsilon_d$  and  $\epsilon_p = \epsilon_d + \Delta$ , respectively. Because of strong Coulomb correlations at copper sites ( $U_d \gg \Delta$ ), only singly occupied  $3d$  states are taken into account:  $\tilde{d}_{i\sigma}^+ = d_{i\sigma}^+ (1 - n_{i,-\sigma}^d)$ . The Wannier representation is introduced here for the oxygen orbitals, as a result of which the parameters of  $p$ - $d$  hybridization are

written as  $V_{ij} = 2t_{pd}v_{ij}$ , where the Wannier coefficients  $v_{ij}$  for the intrasite hybridization and the hybridization between the first and the second neighboring atoms are equal to:  $v_0 = v_{jj} \approx 0.96$ ,  $v_1 = v_{jj \pm a_{xy}} \approx -0.14$ ,  $v_2 = v_{jj \pm a_x \pm a_y} \approx -0.02$  [12]. Because the one-site hybridization is sufficiently large and considerably larger than the intersite one, the one-site part of the Hamiltonian in Eq. (1) should first be reduced to the diagonal form, and then the intersite hybridization should be written using the operators of the new (renormalized) one-site states. Taking into account only the two lowest energy levels, namely, the one-hole  $d$  state with the renormalized energy  $E_1 = \tilde{\epsilon}_d - \mu$  (where  $\mu$  is the chemical potential) and the two-hole singlet  $p$ - $d$  state with the energy  $E_2 = 2E_1 + \tilde{\Delta}$  (where  $\tilde{\Delta} \approx \Delta$ ), I come to the two-band effective Hubbard model [12]

$$H = E_1 \sum_{i,\sigma} X_i^{\sigma\sigma} + E_2 \sum_i X_i^{22} + \sum_{i \neq j, \sigma} \{ t_{ij}^{11} X_i^{\sigma 0} X_j^{0\sigma} + t_{ij}^{22} X_i^{2\sigma} X_j^{\sigma 2} + 2\sigma t_{ij}^{12} (X_i^{2\bar{\sigma}} X_j^{0\sigma} + \text{h.c.}) \}. \quad (2)$$

Here, I introduced the Hubbard operators  $X_i^{nm}$  =  $|in\rangle\langle im|$  describing transitions between the states indicated above:  $n, m = |0\rangle, |\sigma\rangle; |2\rangle = |\uparrow\downarrow\rangle; \sigma = \pm 1/2$ ; and  $\bar{\sigma} = -\sigma$ . The coefficients  $t_{ij}^{\alpha\beta} = K_{\alpha\beta} V_{ij}$  determine the effective hopping integrals between lattice sites ( $i \neq j$ ) for the one-hole subband of the  $d$  type ( $\alpha = 1$ ) and for the two-hole subband of the  $p$ - $d$  type ( $\alpha = 2$ ) and their hybridization. Parameters  $K_{\alpha\beta}$  depend on the value of one-site hybridization  $t_{pd}/\Delta$ . For physically reasonable parameters  $\Delta \approx 2t_{pd}$ , all the coefficients are of the same order of magnitude  $K_{\alpha\beta} \leq 1$  [12]. In view of the smallness of the Wannier coefficients  $v_{ij}$  in the definition of  $V_{ij}$  for distinct sites  $i \neq j$ , the hopping integrals  $t_{ij}^{\alpha\beta}$  are small: for the nearest neighbors,  $t_{\text{eff}} \approx 0.15t_{pd} \approx 0.2\text{eV}$  (see estimates in [12-14]). Therefore, the effective width of subbands  $W = 8t_{\text{eff}}$  for a two-dimensional lattice turns out to be smaller than their splitting energy,  $2W \leq \Delta$ , and the Hamiltonian in Eq. (2) corresponds to the limit of strong correlations in the Hubbard model.

In the limit of strong correlations, the interband hybridization can be excluded in the second order with respect to parameter  $t_{ij}^{12}$ , and the Hamiltonian in Eq. (2) can be reduced to the effective one-band  $t$ - $J$  model. In the case of  $p$ -type doping, this model for the singlet subband can be written using the Hubbard operators in the form

$$H_{t-J} = \sum_{i \neq j, \sigma} t_{ij}^{22} X_i^{2\sigma} X_j^{\sigma 2} - \mu \sum_i X_i^{22} + \frac{1}{4} \sum_{i \neq j, \sigma} J_{ij} (X_i^{\sigma\bar{\sigma}} X_j^{\bar{\sigma}\sigma} - X_i^{\sigma\sigma} X_j^{\bar{\sigma}\bar{\sigma}}), \quad (3)$$

where the exchange interaction  $J_{ij} = 4(t_{ij}^{12})^2/\tilde{\Delta}$ . In the case of  $n$ -type doping, the Hamiltonian in Eq. (2) is reduced to the effective one-band  $t$ - $J$  model for the one-hole states described by Hubbard operators  $X_i^{\sigma 0}(X_j^{0\sigma})$  with the hopping integral  $t_{ij}^{11}$ . However, the exchange interaction retains its previous form, as well as in the Hamiltonian in Eq. (3), which can be written in the standard Heisenberg form  $H_J = (1/2)\sum_{i \neq j} J_{ij} \mathbf{S}_i \mathbf{S}_j$  for the spin operators  $S_i^\pm = X_i^{\pm\mp}$ ,  $S_i^z = (1/2)(X_i^{++} - X_i^{--})$ . The above expression for the exchange interaction  $J_{ij}$  was obtained in the second order with respect to the hybridization parameter  $t_{ij}^{12}$ . A more consistent method of the reduction of the full  $p$ - $d$  model to an effective one-band  $t$ - $J$  model is given in [14], where the importance of the three-site terms that arise in such a reduction and can make a significant contribution to the dispersion curves of quasiparticles is also discussed. In this work, such refinements of the model will be neglected for qualitative estimates.

Using the method of projecting the equations of motion for the Hubbard operators, the system of Gor'kov equations can be readily obtained in the MFA for the normal and anomalous components of the one-particle Green's function (see [8]). In this case, the self-consistent equation for the superconducting gap  $\phi_\sigma(\mathbf{q})$  in the singlet subband takes the form

$$\begin{aligned} \phi_\sigma(\mathbf{q}) &= \frac{1}{N\chi_2} \sum_{\mathbf{k}} J(\mathbf{k} - \mathbf{q}) \langle X_{-\mathbf{q}}^{2\bar{\sigma}} X_{\mathbf{q}}^{2\sigma} \rangle \\ &= \frac{1}{N} \sum_{\mathbf{k}} J(\mathbf{k} - \mathbf{q}) \frac{\phi_\sigma(\mathbf{k})}{2E(\mathbf{k})} \tanh \frac{E(\mathbf{k})}{2T}, \end{aligned} \quad (4)$$

where the quasiparticle energy  $E(\mathbf{k}) = [\epsilon(\mathbf{k})^2 + |\phi_\sigma(\mathbf{k})|^2]^{1/2}$ , and  $\epsilon(\mathbf{k})$  is the excitation spectrum in the singlet subband in the normal state. The parameter  $\chi_2 = \langle X_i^{22} + X_i^{\sigma\sigma} \rangle = n/2$  determines the weight of the singlet band, depending on the hole concentration  $n = 1 + \delta$ .

Going beyond the scope of the MFA in [8] taking into account the self-energy corrections in the Green's functions in the second order with respect to the hopping integrals  $t_{ij}^{22}$  (in the approximation of noncrossing diagrams) allowed the damping of the quasi-particle spectrum in the  $t$ - $J$  model and the additional contribution to pairing due to the exchange of spin fluctuations, which arise through the kinematical interactions in the second order with respect to the hopping integrals. It was also found that the exchange interaction, for which the effects of retardation (and finite quasiparticle lifetime) are not important, makes the main contribution to superconducting pairing. Therefore, in order to estimate  $T_c$  within the framework of the two-band  $p$ - $d$  or reduced  $t$ - $J$  model (Eq. (3)), it is sufficient to examine

the gap equation (Eq. (4)) with allowance made for only the exchange interaction.

This conclusion was confirmed recently in the solution of the system of equations for the Green's function of the four-component Hubbard operators  $\hat{X}_{i\sigma}^\dagger = (X_i^{2\sigma} X_i^{\bar{\sigma}0} X_i^{\bar{\sigma}2} X_i^{0\sigma})$  for the two-band model (Eq. (2)) in [9]. In this work, it was shown that the anomalous averages in the model defined by Eq. (2) are determined by the correlation functions of the form  $\langle c_{i\downarrow} c_{i\uparrow} N_j \rangle = \langle X_i^{02} N_j \rangle = -(4t_{ij}^{12}/\Delta)2\sigma \langle X_i^{\sigma 2} X_j^{\bar{\sigma}2} \rangle$ , whose calculation leads to Eq. (4) with the exchange interaction  $J_{ij}$  if the retardation effects of order  $(t_{ij}^{22}/\Delta)$  are neglected.

**3.** Taking into account what was outlined above, I will estimate the temperature of the  $d$ -wave superconducting pairing in Eq. (4), assuming that the gap is described by the dependence  $\phi_\sigma(\mathbf{q}) = \phi_d(\cos q_x - \cos q_y) = \phi_d \eta(\mathbf{q})$ . Multiplying Eq. (4) by  $\eta(\mathbf{q})$  and summing up over  $\mathbf{q}$  for the model of the nearest neighbor exchange interaction  $J(\mathbf{q}) = 2J(\cos q_x + \cos q_y)$  give the equation for  $T_c$

$$\begin{aligned} 1 &= \frac{J}{2N} \sum_{\mathbf{k}} (\eta(\mathbf{k}))^2 \frac{1}{\epsilon(\mathbf{k})} \tanh \frac{\epsilon(\mathbf{k})}{2T_c} \\ &\approx \frac{J}{2} \int_{-\mu}^{W-\mu} \frac{d\epsilon}{\epsilon} N(\epsilon) \tanh \frac{\epsilon}{2T_c}. \end{aligned} \quad (5)$$

This approximate equation was obtained after averaging over the angles of the  $\mathbf{k}$  vector and passing to integration over the quasi-particle energy in the singlet conduction subband with the effective bandwidth  $W$  and the density of states  $N(\epsilon)$ . Calculations show (see, for example, [12]) that the density of states in the initial Hubbard model (Eq. (2)) depends on the energy and concentration of holes in a rather sophisticated way. However, in contrast to the conventional theory of boson pairing, in which integration is performed in a narrow energy layer on the order of the boson energy at the Fermi energy  $E_F$  and, therefore, the density of states at the Fermi surface  $N(\epsilon = 0)$  determines the coupling constant, integration in our case is extended over the entire conduction band. In this case, qualitative estimates can be obtained by carrying out the integration in Eq. (5) by introducing the averaged density of states  $N_\delta$ . In the weak coupling approximation for  $T_c \ll \mu = E_F$ , the following estimate for the pairing temperature can be obtained in the logarithmic approximation:

$$T_c \approx 1.14 \sqrt{\mu(W - \mu)} \exp(-1/\lambda), \quad \lambda \approx JN_\delta, \quad (6)$$

where  $\mu = E_F(\delta)$  determines the dependence of the Fermi energy on the concentration of holes  $\delta$  in the singlet band. Because the exchange interaction energy in cuprates is sufficiently large,  $J \approx 0.13$  eV, at a moderate density of states in the narrow correlation band, for example,  $N_\delta \geq 2$  (eV) $^{-1}$ , one obtains  $\lambda \approx 0.3$ . The max-

imum value of  $T_c$  is reached at optimal doping,  $E_F(\delta_{\text{opt}}) \approx W/2$ . Here, because the preexponential factor (electronic Fermi energy) is large (for example,  $E_F \approx 0.35$  eV [15]), the pairing temperature is high,  $T_c \approx 170$  K. For deviations from the optimal doping,  $E_F \neq W/2$ ,  $T_c$  decreases, which corresponds to the  $T_c(\delta)$  dependence observed experimentally for all the copper oxide superconductors. It is evident that the estimate obtained above is not suitable in the case of light doping when antiferromagnetic correlations lead to a significant rearrangement of the quasiparticle (spin polaron) spectrum and the Fermi surface (when hole pockets formed in the vicinity of  $(\pm\pi/2, \pm\pi/2)$  points of the Brillouin zone).

4. Now, the  $T_c(a)$  (Eq. (6)) dependence on the lattice constant  $a$  will be estimated based on the assumption that the exchange interaction for the nearest neighbors  $J$  makes the main contribution to this dependence. In addition to the explicit dependence on the one-site hybridization parameter  $t_{pd}$ , the above equation for the exchange interaction  $J_{ij}$  in the second order with respect to  $t_{ij}^{12}$  also contains an implicit dependence on this parameter due to the renormalization of the starting one-particle and singlet  $p-d$  states made when the Hamiltonian in Eq. (2) was derived. To simplify the estimations, I will use the simple dependence of the indirect exchange interaction on the  $p-d$  hybridization as  $J(a) \propto t_{pd}^4$  already obtained by Ph. Anderson and used in the original work by Zhang and Rice [10]. Taking into account that the  $p-d$  hybridization parameter depends on the distance according to the relationship  $t_{pd}(a) \propto 1/(a)^{7/2}$  [16], one obtains the estimate  $J(a) \propto (1/a)^{14}$ . In this approximation, the dependence of the transition temperature (Eq. (6)) on the interatomic distance takes the form

$$\frac{d \ln T_c}{d \ln a} = \frac{d \ln T_c}{d \ln J} \frac{d \ln J}{d \ln a} \approx -14 \frac{1}{\lambda} \approx -47. \quad (7)$$

Using the experimental data for the Hg-1201 compound  $T_c = 97$  K at  $a = 3.880$  Å and the dependence  $dT_c/da \approx -1.35 \times 10^3$  K/Å [2] gives the value for the logarithmic derivative  $d \ln T_c/d \ln a \approx 54$ , close to our estimate (Eq. (7)). To obtain more rigorous quantitative estimates, it is necessary to examine the gap equations in the initial two-band  $p-d$  Hubbard model (Eq. (2)) as was done in [9]. However, the qualitative conclusion that the dependence of the transition temperature  $T_c(a)$  is strong because of the significant change in the indirect exchange interaction upon a change in the hybridization parameter  $t_{pd}(a)$  (and in the Cu–O bond angle) will be certainly retained.

The fact that the dependence of the transition temperature  $T_c$  on the lattice constant at the optimal doping  $\delta_{\text{opt}}$  is so strong is difficult to explain within the framework of other pairing mechanisms, because the contri-

bution to the change in  $T_c$  due to charge transfer is absent in this case. According to the experimental results,  $T_c(\delta) \propto (\delta - \delta_{\text{opt}})^2$  and  $dT_c/da \propto dT_c/d\delta = 0$  in the vicinity of  $\delta_{\text{opt}}$ , and the other electronic parameters ( $E_F, N_\delta$ ) vary only slightly in the case of insignificant compression,  $\Delta/a \approx 0.008$ .

The electron–phonon pairing mechanism is commonly justified by the occurrence of the isotope effect in cuprate superconductors: a small decrease of 0.5–1 K in the  $T_c$  temperature is observed on substituting  $^{18}\text{O}$  oxygen for  $^{16}\text{O}$ , so that the isotope exponent at the optimal doping is small,  $\alpha = -d \ln T_c/d \ln M \leq 0.1$ . Outside the region of optimal doping or on introducing impurities that lower  $T_c$ ,  $\alpha$  can reach high values,  $\alpha \approx 0.6$ . I will show that this isotope effect can also be explained in the context of the electronic pairing mechanism considered above.

Taking into account the existence of a certain correlation between the dependence of  $T_c$  on the pressure and mass of ions at isotope substitution [17] and the analysis of  $T_c(a)$  given above, one may suggest that the isotope effect in cuprates is also associated with the change in the exchange energy  $J$  upon isotope substitution of oxygen. Actually, the isotope effect at the Néel temperature was found in [18]: upon substituting  $^{18}\text{O}$  oxygen for  $^{16}\text{O}$ , the Néel temperature  $T_N = 310$  K in nondoped  $\text{La}_2\text{CuO}_4$  decreased by 1.8 K, which gives  $\alpha_N = -d \ln T_N/d \ln M \approx 0.05$ . Because the Néel temperature is determined by the exchange interaction,  $T_N \propto J$ , the isotope exponent can be estimated for the superconducting transition temperature in lanthanum compounds using the relationship

$$\alpha = -\frac{d \ln T_c}{d \ln M} = -\frac{d \ln T_c}{d \ln J} \frac{d \ln J}{d \ln M} \approx \frac{1}{\lambda} \alpha_N \approx 0.16. \quad (8)$$

For the absolute shift of  $T_c$ , the relationship  $\Delta T_c \approx (1/\lambda)(T_c/T_N)\Delta T_N \approx 0.7$  K is obtained, where it is assumed that  $T_c \approx 40$  K and  $T_N = 310$  K. When  $T_c$  decreases outside the region of optimal doping, the coupling constant  $\lambda$  decreases, and the isotope exponent can reach a high value. The estimates obtained in this work correspond to the results observed experimentally.

5. Thus, the calculation carried out within the framework of the two-band Hubbard model (Eq. (2)) in the limit of strong correlations indicates that the retardation effects are not important in the case when two electrons (holes) are paired through the AFM exchange interaction. Therefore, all the particles in the filled subband can participate in pairing because of the large energy of interband splitting  $\Delta \gg |t_{ij}^{\alpha\beta}|$ . Hence, as in the BCS theory, the superconducting transition temperature can be estimated using the one-band  $t-J$  model with the instant exchange interaction. This pairing mechanism is principally distinguished by the suppression of the retardation effects from the standard mechanisms based on the

exchange of bosons (phonons or spin excitations), in which pairing due to the retardation effects is restricted to a narrow region of energies on the order of the boson energy  $\omega_0$  at the Fermi surface. Because the boson energy  $\omega_0 \leq 0.05$  eV is low, high  $T_c$  can be obtained in these models only in the case of strong coupling.

The strong dependence of the transition temperature  $T_c$  on zinc impurities as compared to paramagnetic impurities observed in cuprates [1] may serve as a confirmation of the AFM exchange mechanism of pairing. The fully occupied  $3d$  shell in  $Zn^{2+}$  ( $3d^{10}$ ) blocks the AFM exchange, which must lead to an additional decrease in  $T_c$  as compared to the common effects of a drop in  $T_c$  due to the impurity scattering.

Because the AFM exchange interaction is a specific property of systems with strong electron correlations and is absent in conventional Fermi systems (see discussion in [19]), it may be argued that the specific pairing mechanism in cuprates is due to the AFM exchange, whose energy reaches a record high value in cuprates because of peculiarities of their electronic structure. One may expect a manifestation of the AFM exchange interaction in other systems with strong Coulomb correlations as, for example, in vanadates or in systems with heavy fermions in which AFM ordering is observed along with superconductivity.

#### REFERENCES

1. N. M. Plakida, *High-temperature Superconductivity: Experiment and Theory* (Springer-Verlag, Berlin, 1995).
2. E. V. Antipov, A. M. Abakumov, K. A. Lokshin, *et al.*, *Physica C* (Amsterdam) **341–348**, 579 (2000); K. A. Lokshin, D. A. Pavlov, S. N. Putilin, *et al.*, *Phys. Rev. B* **63**, 064511 (2001).
3. J.-P. Locquet, J. Perret, J. Fompeyrine, *et al.*, *Nature* **394**, 453 (1998).
4. P. W. Anderson, *Science* **235**, 1196 (1987).
5. P. W. Anderson, *The Theory of Superconductivity in the High- $T_c$  Cuprates* (Princeton Univ. Press, Princeton, 1997).
6. Yu. A. Izyumov, *Usp. Fiz. Nauk* **169**, 225 (1999).
7. N. M. Plakida, V. Yu. Yushankhai, and I. V. Stasyuk, *Physica C* (Amsterdam) **160**, 80 (1989); V. Yu. Yushankhai, N. M. Plakida, and P. Kalinay, *Physica C* (Amsterdam) **174**, 401 (1991).
8. N. M. Plakida and V. S. Oudovenko, *Phys. Rev. B* **59**, 11949 (1999).
9. N. M. Plakida, L. Anton, S. Adam, and Gh. Adam, Preprint E-17-2001-59 (Joint Inst. for Nuclear Research, Dubna, 2001); cond-mat/0104234.
10. F. C. Zhang and T. M. Rice, *Phys. Rev. B* **37**, 3759 (1988).
11. V. Emery, *Phys. Rev. Lett.* **58**, 2794 (1987); C. M. Varma, S. Schmitt-Rink, and E. Abrahams, *Solid State Commun.* **62**, 681 (1987).
12. N. M. Plakida, R. Hayn, and J.-L. Richard, *Phys. Rev. B* **51**, 16599 (1995).
13. L. F. Feiner, J. H. Jefferson, and R. Raimondi, *Phys. Rev. B* **53**, 8751 (1996); R. Raimondi, J. H. Jefferson, and L. F. Feiner, *Phys. Rev. B* **53**, 8774 (1996).
14. V. Yu. Yushankhai, V. S. Oudovenko, and R. Hayn, *Phys. Rev. B* **55**, 15562 (1997).
15. L. P. Gor'kov and N. B. Kopnin, *Usp. Fiz. Nauk* **156**, 117 (1988) [*Sov. Phys. Usp.* **31**, 850 (1988)].
16. W. A. Harrison, *Electronic Structure and the Properties of Solids* (Freeman, San Francisco, 1983).
17. J. P. Franck, *Physica C* (Amsterdam) **282–287**, 198 (1997).
18. Guao-Meng Zhao, K. K. Singh, and D. E. Morris, *Phys. Rev. B* **50**, 4112 (1994).
19. P. W. Anderson, *Adv. Phys.* **46**, 3 (1997).

*Translated by A. Bagatur'yants*

# Anisotropy of Electronic Wave Functions in Self-Assembled InAs Dots Embedded in the Center of a GaAs Quantum Well Studied by Magnetotunneling Spectroscopy<sup>1</sup>

E. E. Vdovin<sup>1</sup>, Yu. N. Khanin<sup>1</sup>, A. V. Veretennikov<sup>3</sup>, A. Levin<sup>2</sup>, A. Patane<sup>2</sup>, Yu. V. Dubrovskii<sup>1</sup>,  
L. Eaves<sup>2</sup>, P. C. Main<sup>2</sup>, M. Henini<sup>2</sup>, and G. Hill<sup>4</sup>

<sup>1</sup> *Institute of Microelectronics Technology, Russian Academy of Sciences,  
Chernogolovka, Moscow region 142432 Russia*

<sup>2</sup> *School of Physics and Astronomy, University of Nottingham, Nottingham NG7 2RD, UK*

<sup>3</sup> *Institute of Solid State Physics, Russian Academy of Sciences, Chernogolovka, Moscow region 142432 Russia*

<sup>4</sup> *Dept. of Electronic and Electrical Engineering, University of Sheffield, UK*

Received June 5, 2001

We present an experimental study of electron wave functions in InAs/GaAs self-assembled quantum dots by magnetotunneling spectroscopy. The electronic wave functions have a biaxial symmetry in the growth plane, with axes corresponding to the main crystallographic directions in the growth plane. Moreover, we observed the in-plane anisotropy of the subbands of the quantum well. © 2001 MAIK “Nauka/Interperiodica”.

PACS numbers: 73.21.La; 73.21.Fg; 73.40.Gk; 73.61.Ey

Quantum dots (QDs) are characterized by a relatively small number of electrons confined within an island of a nanometer dimension. They can confine the motion of an electron in all three spatial dimensions [1]. The strong confinement in the QD gives rise to a set of discrete and narrow electronic energy levels similar to those in atomic physics. The epitaxial growth of lattice-mismatched InAs on GaAs or AlAs opens new possibilities for the simple fabrication of semiconductor nanostructures. InAs QDs are formed *in situ* during growth owing to the relaxation of a strained InAs wetting layer on GaAs or AlAs [2]. The particular interest lies in their uniformity and small size: lateral dimension 10–20 nm and height 3–4 nm. Several theoretical approaches were used to calculate the eigenstates of InAs QDs [3]. The results of calculation depend strongly on the assumed shape and composition of the QDs. Experimentally, the quantized energy levels of a given potential can be probed using various spectroscopic techniques. The corresponding wave functions are much more difficult to measure. Information about the extent of the carrier wave function for the ground state of a QD was obtained from tunneling measurements in a magnetic field [4]. Also, the anisotropy of electronic wave function in self-aligned InAs QDs was deduced from magnetic-field-dependent photoluminescence spectroscopy [5]. However, until recently there have been no reported

measurements of the detailed spatial form of the ground- and excited-state wave functions of the QD. Recently, it has been demonstrated that magnetotunneling spectroscopy can be employed as a noninvasive probe to produce images of the probability density of the electron confined in a QD [6]. In this work, we use magnetotunneling spectroscopy to investigate in detail the spatial form of the wave functions of the electronic states of a double-barrier resonant tunneling diode with InAs QDs embedded in the center of a GaAs quantum well (the ground and excited states of the QDs and confined subbands of the quantum well). We measure the dependence of the resonant tunneling current through the QD states as a function of magnetic field,  $B$ , applied perpendicular to the tunneling direction. This allows us to map out the full spatial form of the probability density of the ground and excited states of the QDs and confined subbands of the quantum well. The electronic wave functions have a biaxial symmetry in the growth plane, with axes corresponding quite closely (within measurement error of 15°) to the main crystallographic directions  $X[01\bar{1}]$  and  $Y[\bar{2}33]$  for (311) $B$  substrate orientation. For a similar InAs QD structure grown on a (100) substrate, we also obtained characteristic probability density maps of ground and excited states. Moreover, we observed the in-plane anisotropy of the subbands of the quantum well.

InAs QDs are embedded in an  $n-i-n$  resonant tunneling diode. Samples were grown by molecular beam epitaxy on a GaAs substrate with the orientations (100)

<sup>1</sup> This article was submitted by the authors in English.

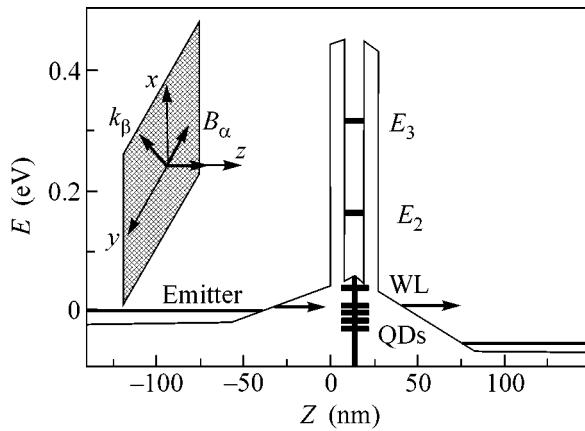


**Fig. 1.** Schematic conduction band profile under an applied bias of an  $n$ - $i$ - $n$  GaAs/(AlGa)As double barrier resonant tunneling diode incorporating InAs QDs. Inset: orientation of the magnetic field,  $B$ , and current,  $I$ , in the magnetotunneling experiment.  $X$  and  $Y$  define the two main crystallographic axes  $[01\bar{1}]$  and  $[\bar{2}33]$ , respectively, in the  $(311)$ -oriented GaAs substrate.  $\alpha$  and  $\beta$  indicate, respectively, the direction of  $B$  and of the momentum acquired by the tunneling electron due to the action of the Lorentz force.

and  $(311)B$ . A layer of InAs QDs, nominally 2.3 monolayers thick, was placed in the center of a 9.6-nm-wide GaAs quantum well (QW) with 8.3-nm  $\text{Al}_{0.4}\text{Ga}_{0.6}\text{As}$  confining barriers, sandwiched between two nominally undoped 50-nm GaAs spacer layers. The intrinsic region was surrounded by graded  $n$ -type contact layers, with the doping concentration increasing from  $2 \times 10^{17} \text{ cm}^{-3}$  to  $3 \times 10^{18} \text{ cm}^{-3}$ . The layers were grown at  $600^\circ\text{C}$ , and there was a growth interrupt before the QDs were grown at  $480^\circ\text{C}$ . For comparison, we also studied two control samples grown with the same sequence of layers, except that one had only a thin InAs two-dimensional wetting layer (i.e., containing no QDs) and the other had no InAs layer at all. The samples were processed into circular mesa structures of diameters between 50 and 200  $\mu\text{m}$ , with ohmic contacts to the doped regions.

Figure 1 shows a schematic energy band diagram for our device under bias voltage.  $X$  and  $Y$  define the two main crystallographic axis in the plane perpendicular to the growth direction  $Z$  (see inset). The layer of InAs QDs introduces a set of discrete electronic states below the GaAs conduction band edge. At zero bias voltage, equilibrium is established by electrons diffusing from the doped GaAs layers and filling some of the dot states. The resulting negative charge in the QW produces depletion layers in the regions beyond the (AlGa)As barriers. By applying a bias voltage to the emitter layer,  $V$ , the QD energy level is shifted in energy with respect to both contacts. When a particular dot state is resonant with an adjacent filled state in the biased electron emitter layer, electrons tunnel through the dot into the collector and a current flows as shown

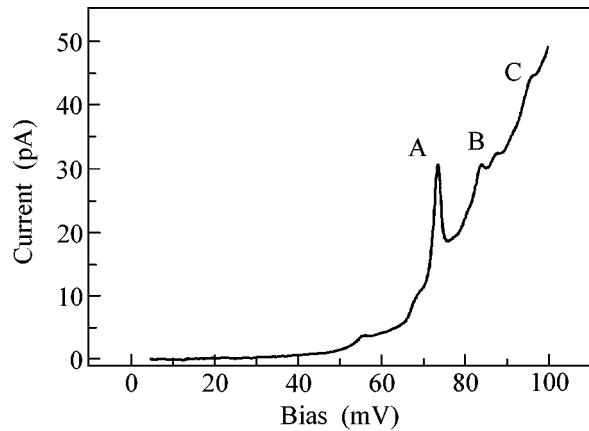


**Fig. 2.** Low-temperature ( $T = 1.2 \text{ K}$ ) current-voltage characteristics,  $I(V)$ . Dots are grown on  $(311)B$  substrate orientation.

schematically in Fig. 1. Therefore, as we adjust the voltage, we can study different energy states of the QDs. At sufficiently high voltages we are able to observe two separate resonances in the current related to confined subbands of the QW states.

Figure 2 shows a typical low-temperature ( $T = 1.2 \text{ K}$ )  $I(V)$  curve. The device contains InAs QDs grown on a  $(311)B$ -oriented GaAs substrate. Similar results were obtained for QDs grown on a  $(100)$  substrate. We observe a series of resonant peaks corresponding to carrier tunneling into the dot states. Pronounced current features appear at biases as low as 55 mV. They are superimposed on a rising background current and cannot be resolved for  $V > 200 \text{ mV}$ . These features are not observed in our control samples which do not contain QDs, and, therefore, we can ascribe them to the InAs QD layer. Despite the large number of quantum dots in our sample ( $10^6$ – $10^7$  for a 100- $\mu\text{m}$ -diameter mesa), we observed only a small number of resonant peaks in the bias range ( $\sim 200 \text{ mV}$ ) close to the threshold for current flow. This behavior has been reported in earlier studies [4, 6–12] and, although not fully understood, is probably related to the limited number of conducting channels in the emitter that can transmit electrons from the doping layer to the quantum dots at low bias. There is no reason to believe that the dots studied are atypical of the distribution as a whole. On increasing the temperature to 4.2 K, the main peaks are still prominent, but much weaker features, which may be related to density-of-state fluctuation in the emitter [13], are strongly suppressed. A key observation is that many peaks look similar, so we cannot tell if the peaks are due to tunneling through the states of a single dot or several dots. In the following, we will concentrate on three voltage regions labeled A, B, and C. We will focus on the magnetic-field dependence of the QD resonances and on how this provides detailed information about the form of the wave function associated with an electron in the QD state.

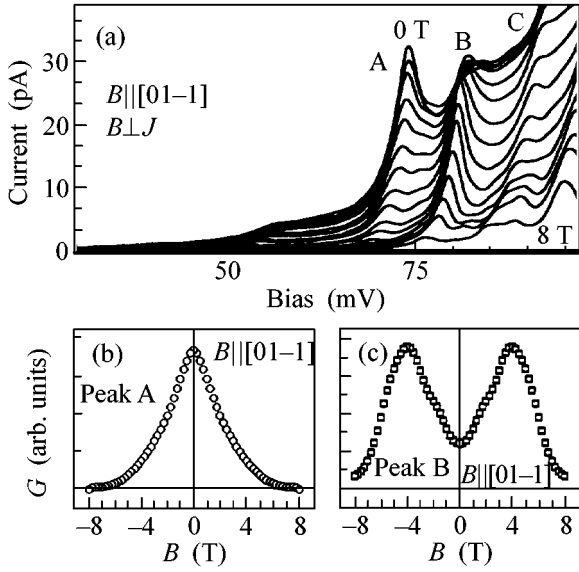


**Fig. 3.** (a) Low-temperature ( $T = 4.2$  K)  $I(V)$  characteristics in the presence of a magnetic field  $B$ . The direction of  $B$  is perpendicular to the current flow. (b, c) Dependence of conductance  $G$  on magnetic field for  $B$  parallel to  $[01\bar{1}]$  for different QDs states.  $B$  was varied from 0 to 8 T with a step of 0.5 T.

Figure 3a shows the low-temperature ( $T = 4.2$  K)  $I(V)$  characteristics in the presence of a magnetic field  $B$ .

The direction of  $B$  is perpendicular to the current flow and lies in the  $(X, Y)$  plane (see Fig. 1). The axes  $[01\bar{1}]$  and  $[\bar{2}33]$  define the two main crystallographic axes in the plane perpendicular to the growth direction  $[311]$ . The amplitude of each resonance exhibits a strong dependence on  $B$ . In particular, with increasing  $B$ , the low-voltage resonances “A” decrease steadily in amplitude, whereas the others, “B” and “C,” have a nonmonotonic magnetic-field dependence. Figures 3b and 3c clearly show two characteristic types of magnetic-field dependence: type “A” shows a maximum for  $G(B)$  at  $B = 0$  T followed by a steady decay to zero at about 8 T; type “B” shows a broad maximum at  $\sim 4.5$  T followed by a gradual decay to zero.

Figure 4a shows the  $I(V)$  characteristics in an in-plane magnetic field of 4.5 T. The first curve (circles) is for  $B \parallel [01\bar{1}]$ , and the second curve (triangles) is for  $B \parallel [\bar{2}33]$ . We observe a clearly defined anisotropy in the dependence of  $I(V)$  on  $B$  for the two field orientations. As can clearly be seen in Fig. 4a, peaks “A” and “B” in the  $I(V)$  plot reveal a strong anisotropy of about  $\rho \sim 0.5$ . We have also determined angular dependence of the peaks. The results are plotted in Fig. 4b for peaks “A” and “B.” Note that all peaks observed in the bias range ( $\sim 200$  mV) have maxima in current amplitudes at field orientation  $B \parallel [01\bar{1}]$  or  $B \parallel [\bar{2}33]$ . The main

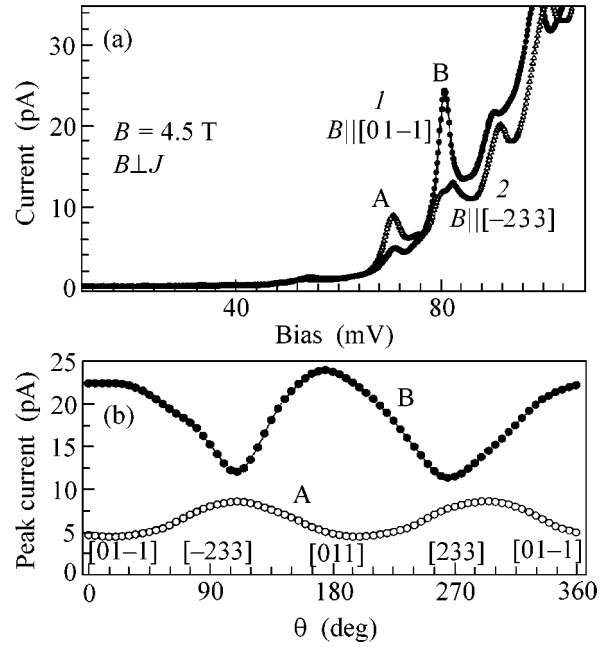


**Fig. 4.** (a)  $I(V)$  characteristics in an in-plane magnetic field of 4.5 T. The first curve (circles) is for  $B \parallel [01\bar{1}]$ , and the second curve (triangles) is for  $B \parallel [\bar{2}33]$ ; (b) angular dependence of the peak current.

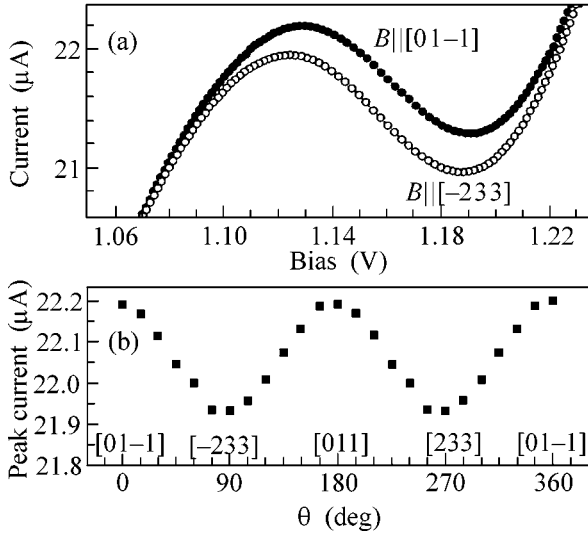
effect to be noted from Fig. 4 is the dependence of the current on the orientation of the in-plane magnetic field.

Figure 5a shows the  $I(V)$  characteristics in an in-plane magnetic field of 4.5 T in the voltage range corresponding to the resonant tunneling through the second subband of the quantum well. The first curve (open circles) is for  $B \parallel [01\bar{1}]$ , and the second curve (solid circles) is for  $B \parallel [\bar{2}33]$ . The anisotropy of the observed resonance is plotted in Fig. 5b. The angular dependence of the peak current measured with magnetotunneling spectroscopy is interpreted as a direct representation of the in-plane anisotropy of a subband [14–16]. The anisotropy of the quantum-well subband can be induced by the orientation of the Al–As bonds at the neighboring interfaces of the quantum well [15].

We can understand the magnetic-field dependence of the features in terms of the effect of  $B$  on a tunneling electron. Let  $\alpha$ ,  $\beta$ , and  $Z$  indicate, respectively, the direction of  $B$ , the direction normal to  $B$  in the growth plane  $(X, Y)$ , and the normal to the tunnel barrier (see Fig. 1b). When an electron tunnels from the emitter into the dot, it acquires an additional in-plane momentum given by [17]

$$k_{\beta} = eB\Delta s/\hbar, \quad (1)$$

where  $\Delta s$  is the effective tunneling distance along  $Z$ . This effect can be understood semiclassically in terms of the increased momentum along  $\beta$ , which is acquired



**Fig. 5.** (a)  $I(V)$  characteristics in an in-plane magnetic field of 4.5 T in the voltage range corresponding to the resonant tunneling through the second subband of the quantum well. The first curve (solid circles) is for  $B \parallel [01\bar{1}]$ , and the second curve (open circles) is for  $B \parallel [\bar{2}33]$ ; (b) angular dependence of the peak current.

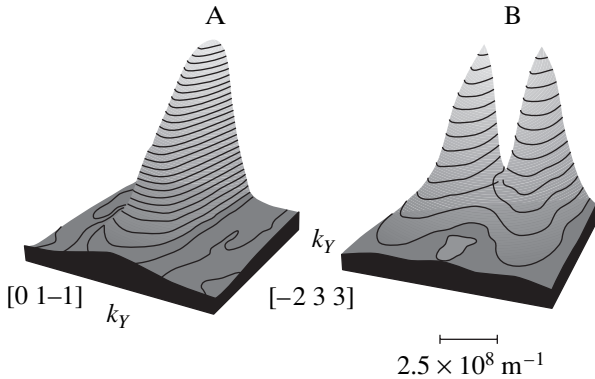


**Fig. 6.** Distribution of the differential conductance  $G = dI/dV$  in the  $(k_x, k_y)$  plane for two representative states. This provides a spatial map of  $|\Phi_{QD}(k_x, k_y)|^2$ , the square of the Fourier transform  $\Phi_{QD}(k_x, k_y)$  of the probability density of an electron confined in the dot.  $X$  and  $Y$  define the two main crystallographic axes  $[01\bar{1}]$  and  $[\bar{2}33]$ , respectively, in the (311)-oriented GaAs plane.

by the tunneling electron due to the action of the Lorentz force. In terms of mapping out the spatial form of an electronic state, we can envisage the effect of this shift as being analogous to the effect of displacement, in real space, of the atomic tip in an STM imaging measurement. The applied voltage allows us to tune resonantly to the energy of a particular QD state. Then, by measuring the variation of the tunnel current with  $B$ , we can determine the value of matrix element that governs the quantum transition of an electron as it tunnels from

a state in the emitter layer into the QD. In our experiment, the tunneling matrix element is most conveniently expressed in terms of the Fourier transforms  $\Phi_{i,k}(\underline{k})$  of the conventional real-space wave functions [17, 18]. Here, the subscripts  $i$  and  $f$  indicate the initial (emitter) and final (QD) states of the tunnel transition. Relative to the strong spatial confinement in the QD, the initial emitter state has only weak spatial confinement. Hence, in  $\underline{k}$  space it corresponds to a sharply peaked function with a finite value only close to  $\underline{k} = 0$ . Since the tunnel current is given by the square of the matrix element involving  $\Phi_i(\underline{k})$  and  $\Phi_{QD}(\underline{k})$ , the narrow spread of  $\underline{k}$  for  $\Phi_i(\underline{k})$  allows us to determine the form of  $\Phi_{QD}(\underline{k})$  by varying  $B$  and, hence,  $\underline{k}$  according to Eq. (1). Thus, by plotting  $G(B)$  for a particular direction of  $B$ , we can measure the dependence of  $|\Phi_{QD}(\underline{k})|^2$  along the  $\underline{k}$  direction perpendicular to  $B$ . Then, by rotating  $B$  in the  $(X, Y)$  plane and making a series of measurements of  $I(B)$  with  $B$  set at regular intervals ( $\Delta\theta \sim 5^\circ$ ) of the rotation angle  $\theta$ , we obtain a full spatial profile of  $|\Phi_{QD}(k_x, k_y)|^2$ . This represents the projection in  $\underline{k}$  space of the probability density of a given electronic state confined in the QD.

The model provides a simple explanation of the magnetic-field dependence of the resonant current features “A–C.” In particular, the *forbidden* nature of the tunneling transition associated with “B” at  $B = 0$  T is due to the odd parity of the final-state wave function, which corresponds to the first excited state of a QD. The applied magnetic field (i.e., the Lorentz force) effectively breaks the mirror symmetry at  $B = 0$  and thus makes the transition *allowed*.

Figure 6 shows the spatial form of  $G(B) \sim |\Phi_{QD}(k_x, k_y)|^2$  in the  $(k_x, k_y)$  plane for the two representative QD states corresponding to the labeled features in Fig. 3b and 3c. The  $\underline{k}$  values are estimated from Eq. (1), assuming that  $\Delta s$  has nominal value of 30 nm, which we estimated from the capacitance measurements and from the doping profile and composition of the device. The contour plots reveal clearly the characteristic form of the probability density distribution of a ground-state orbital and the characteristic lobes of the higher energy states of the QD. The electron wave functions have a biaxial symmetry in the growth plane, with axes corresponding quite closely (within measurement error of  $15^\circ$ ) to the main crystallographic directions  $X - [01\bar{1}]$  and  $Y - [\bar{2}33]$  for (311) $B$  substrate orientation. For a similar InAs QD structure grown on a (100) substrate, we also obtained characteristic probability density maps of ground and excited states.

To summarize, we have observed features in  $I(V)$  corresponding to resonant tunneling through a limited number of discrete states whose wave functions display the symmetry of the ground state and excited states of

quantum dots. With the simple device configuration we have used, it is impossible to tell whether an excited-state feature and a ground-state feature correspond to the same quantum dot. This question could be resolved by new experiments on structures with electrostatic gates.

In conclusion, we have shown how magnetotunneling spectroscopy provides a new means of probing the spatial form of the wave functions of electrons confined in quantum dots and quantum well. The study revealed a biaxial symmetry of QD states in the growth plane. We observed the elliptical shape of the ground state and the characteristic lobes of the higher energy states. Moreover we observed the elliptical shape of the subbands of the quantum well.

The work is supported in part by the Russian Foundation for Basic Research (project no. 00-02-17903), the INTAS-RFBR (grant no. 95-849), and the EPSRC (UK). A.L. gratefully acknowledges the support of the FAPESP Foundation (Brazil). E.E.V. gratefully acknowledge supports from the Royal Society. We are grateful to V.A. Tulin and V.G. Lysenko for helpful discussions and V.V. Belov and A. Orlov for technical assistance.

#### REFERENCES

1. D. Bimberg, M. Grundmann, and N. N. Ledentsov, *Quantum Dot Heterostructures* (Wiley, New York, 1999).
2. C. Pryor, Phys. Rev. B **57**, 7190 (1998); L.-W. Wang, J. Kim, and A. Zunger, Phys. Rev. B **59**, 5678 (1999); O. Stier, M. Grundmann, and D. Bimberg, Phys. Rev. B **59**, 5688 (1999); W. Yang, H. Lee, T. J. Johnson, *et al.*, Phys. Rev. B **61**, 2784 (2000).
3. M. F. Crommie, C. P. Lutz, and D. M. Eigler, Nature **262**, 218 (1993).
4. M. Narihiro, G. Yusa, Y. Nakamura, *et al.*, Appl. Phys. Lett. **70**, 105 (1997).
5. H. J. Zhu, M. Ramsteiner, K. H. Ploog, *et al.*, Phys. Rev. B **62**, 16314 (2000).
6. E. E. Vdovin, A. Levin, A. Patane, *et al.*, Science **290**, 122 (2000).
7. A. Patane, A. Polimeni, L. Eaves, *et al.*, Phys. Rev. B **62**, 13595 (2000).
8. P. C. Main, A. S. G. Thornton, R. J. A. Hill, *et al.*, Phys. Rev. Lett. **84**, 729 (2000).
9. T. Suzuki, K. Nomoto, K. Taira, and I. Hase, Jpn. J. Appl. Phys., Part 1 **36**, 1917 (1997).
10. I. E. Itskevich, T. Ihn, A. Thornton, *et al.*, Phys. Rev. B **54**, 16401 (1996).
11. I. Hapke-Wurst, U. Zeitler, H. Frahm, *et al.*, Phys. Rev. B **62**, 12621 (2000).
12. D. G. Austing, S. Tarucha, P. C. Main, *et al.*, Appl. Phys. Lett. **75**, 671 (1999).
13. T. Schmidt, R. J. Haug, V. I. Fal'ko, *et al.*, Phys. Rev. Lett. **78**, 1540 (1997).
14. F. Aristone, J. F. Palmier, P. Gassot, *et al.*, Appl. Phys. Lett. **67**, 2916 (1995).
15. P. W. Lukey, J. Caro, T. Zijlstra, *et al.*, Phys. Rev. B **57**, 7132 (1998).
16. T. Reker, H. Im, L. E. Bremme, *et al.*, in *Proceedings of the 25th International Conference on Physics of Semiconductor, ICPS, Osaka, 2000*.
17. P. H. Beton, H. Buhmann, L. Eaves, *et al.*, Phys. Rev. Lett. **75**, 1996 (1995).
18. J. W. Sakai, T. M. Fromhold, P. H. Beton, *et al.*, Phys. Rev. B **48**, 5664 (1993).

# A Simplified Model for the Rearrangement of Single-Particle Degrees of Freedom near the Point of Antiferromagnetic Phase Transition in Strongly Correlated Fermi Systems

M. V. Zverev, V. A. Khodel', and J. W. Clark\*

Russian Research Centre Kurchatov Institute, pl. Kurchatova 1, Moscow, 123182 Russia

\*Washington University, St. Louis, USA

Received June 7, 2001

It is shown that the antiferromagnetic transition is preceded by the fermion condensation with rearrangement of single-particle degrees of freedom and appearance of plateaus in the spectrum of single-particle excitations. The results obtained are used to explain the gap structure in the spectrum of two-dimensional high- $T_c$  superconductors at  $T = 0$ . © 2001 MAIK "Nauka/Interperiodica".

PACS numbers: 71.27.+a; 71.10.-Hf; 74.20.-z

It is well known that the quasiparticle description is the most fruitful approach in the theory of Fermi systems. With this approach, the characteristics of different systems are calculated using different quasiparticle schemes. The simplest of them, the Kohn–Sham scheme, is suitable for calculating energies of the systems with Coulomb forces. In this scheme, the quasiparticles and free particles are identical, while the effective interaction between them is constructed using the Monte-Carlo computations of electron-gas energy  $E(\rho)$ . However, this scheme is ill suited for calculating the single-particle excitation spectra, because it does not take into account a change in the effective interaction upon the addition of a particle. More sophisticated quasiparticles with the dispersion of a single-particle spectrum in a medium are introduced in the theory of Fermi liquid. This theory is based on well-known experimental facts, in particular, on the fact that the damping of single-particle excitations near the Fermi surface (FS), as a rule, is weak, allowing the system to be treated as a gas of interacting undamped quasiparticles with the same momentum distribution  $n_F(p)$  as in an ideal Fermi gas. Inasmuch as the relevant Monte-Carlo computations are lacking, one is forced to use the available experimental data to parameterize the effective interaction between quasiparticles. This approach allows the qualitative description of a broad spectrum of phenomena, and this was clearly demonstrated by Migdal in the theory of atomic nucleus [1]. The theory of Fermi liquid is good not only for atomic nuclei but also for many other real systems, including liquid  $^3\text{He}$  and metals. It is worthy of note that, if their properties were described using Kohn–Sham quasiparticles, instead of Landau–Migdal ones, the qualitative picture would suffer only insignificantly. As to the quantitative

aspect of the problem, the stronger the correlation and the higher the velocity forces, the greater the number of parameters characterizing the interaction needed to describe the experiment.

However, this is unhelpful if one deals with strongly correlated systems such as electrons in two-dimensional (2D) high- $T_c$  superconductors, where the damping effects are much stronger than in usual Fermi systems, so that the applicability of a formalism exploiting “immortal” quasiparticles becomes doubtful, in spite of the fact that the Fermi surface is well defined in such systems. To understand the reasons for this inconsistency, one should bear in mind that the standard Landau theory applies only in a certain range of coupling constants. At  $T = 0$ , this theory is operative until the necessary condition for ground-state stability breaks. This condition requires that a change in the total energy  $E_0$ , considered as a functional of momentum distribution, be nonnegative for any variation of  $n_F(\mathbf{p})$ ,

$$\delta E_0 = \sum \xi(\mathbf{p}) \delta n_F(\mathbf{p}) \geq 0. \quad (1)$$

In this formula,  $\xi(\mathbf{p}) = \varepsilon(\mathbf{p}) - \mu$ , where  $\varepsilon(\mathbf{p})$  is the energy of Landau quasiparticle and  $\mu$  is the chemical potential. In a homogeneous system, this condition is violated, e.g., every time when the equation

$$\xi(p) = 0 \quad (2)$$

for determining Fermi momentum  $p_F$  acquires a new root. The latter can appear only if the velocity dependence of the effective interaction between particles (in fact, it is responsible for the single-particle spectrum) becomes strong. This necessarily occurs [2] as the system approaches the point of a second-order phase transition, where a certain branch of collective excitations

collapses, so that the amplitude of oscillations with critical wave number  $\mathbf{q} = \mathbf{q}_c$  starts to grow exponentially. However, before the density  $\rho$  reaches its critical value  $\rho_c$ , the spectrum  $\xi(p; \rho)$  ceases to be a monotonic function of  $p$ , and, hence, the group velocity  $v_g(p) = d\xi(p)/dp$  changes its sign. This change in sign is a precursor of the subsequent rearrangement of Fermi filling and can be analyzed using the Landau–Pitaevski formula [3] written as [4]

$$\frac{\partial \varepsilon(\mathbf{p})}{\partial \mathbf{p}} = \frac{\partial \varepsilon_{\mathbf{p}}^0}{\partial \mathbf{p}} + \frac{1}{2} \int F_{\alpha\delta; \alpha\delta}(\mathbf{p}, \mathbf{p}_1, \mathbf{k} = 0; \omega = 0) \frac{\partial n(\mathbf{p}_1)}{\partial \mathbf{p}_1} d\tau_1. \quad (3)$$

Here,  $\varepsilon_{\mathbf{p}}^0 = p^2/2M$  is the free-particle spectrum;  $d\tau = d^2p/(2\pi)^2$  (for definiteness, a 2D system is considered);  $F(\mathbf{p}_1, \mathbf{p}_2, \mathbf{k} = 0, \omega = 0) = z^2 \Gamma^k(\mathbf{p}_1, \mathbf{p}_2) M^*/M$ , where  $\Gamma^k(\mathbf{p}_1, \mathbf{p}_2)$  is the Landau static amplitude of zero-angle scattering;  $z$  is the renormalizing multiplier; and  $M^*$  is the effective mass.

In the vicinity of the point of second-order phase transition, the amplitude  $F(\rho \rightarrow \rho_c)$  is expressed through the corresponding susceptibility  $\chi(\mathbf{q}, \omega = 0; \rho)$ , which is singular at  $\mathbf{q} \rightarrow \mathbf{q}_c, \rho \rightarrow \rho_c$  [2]. When reconstructing  $F$ , the symmetry relations requiring a change in sign of this amplitude upon particle transposition, i.e., replacement of  $\mathbf{k}$  by  $(\mathbf{p}_1 - \mathbf{p}_2 + \mathbf{k})$  and transposition of the corresponding spin indices, play an important role. With allowance made for these relations, the singular part  $F^e(\mathbf{p}_1, \mathbf{p}_2, \mathbf{k}, \omega = 0)$  of the amplitude in Eq. (3) takes the form [2]

$$F_{\alpha\delta; \beta\gamma}^e(\mathbf{p}_1, \mathbf{p}_2, \mathbf{k}, \omega = 0) \sim -O_{\alpha\beta} O_{\gamma\delta} \chi(\mathbf{k}) + O_{\alpha\gamma} O_{\beta\delta} \chi(\mathbf{p}_1 - \mathbf{p}_2 + \mathbf{k}). \quad (4)$$

Making use of the phenomenological expression obtained in [2] for the static susceptibility  $\chi(\mathbf{q})$  in the vicinity of a transition point and substituting singular amplitude component (4) into Eq. (3), one can verify that, for both the critical density oscillations with  $O = 1$ , considered in [5], and the antiferromagnetic fluctuations (AFs) with  $O_i = \sigma_i$ , analyzed in this work, the  $\xi(p)$  spectrum of a homogeneous system ceases to be a monotonic function of  $p$  well before the density  $\rho$  achieves  $\rho_c$ . In what follows, it is essential that interaction (4) at  $\mathbf{k} = 0$  depends only on the difference  $(\mathbf{p}_1 - \mathbf{p}_2)$ , so that the right-hand side of Eq. (3) can be integrated analytically to arrive at a closed relationship that can be used for calculating the single-particle excitation spectrum and determining the stability limits for the Landau ground state.

For the AFs in a 2D crystal with square lattice, the static spin susceptibility  $\chi(\mathbf{q})$  displays a sharp peak at the point corresponding to the momentum transfer  $\mathbf{q} = \mathbf{Q} \equiv (\pi/a, \pi/a)$ , where  $a$  is the lattice constant. With the

parameterization used in [6], i.e.,  $\chi(\mathbf{q}) \sim F(\mathbf{q}) = [\beta^2 + \gamma^2(\mathbf{q} - \mathbf{Q})^2/Q^2]^{-1}$ , one has from Eq. (3) after simple mathematics

$$\xi(\mathbf{p}) = \xi_{\mathbf{p}}^0 + \frac{3}{2} \int \frac{n_F(\xi(\mathbf{p}_1))}{\beta^2 + \gamma^2(\mathbf{p}_1 - \mathbf{p} + \mathbf{Q})^2/Q^2} d\tau_1. \quad (5)$$

Here, the notation  $\xi_{\mathbf{p}}^0 = \varepsilon_{\mathbf{p}}^0 - \mu$  is introduced, where  $\varepsilon_{\mathbf{p}}^0$  is the LDA-calculated spectrum. Note that the choice of a different vertex  $O$  would only change the numerical coefficient [4].

Thus, based on the renormalized Landau–Pitaevski relation (3), we derived a Hartree–Fock-type relationship between the spectrum  $\xi(\mathbf{p})$  and the distribution  $n(\xi(\mathbf{p}))$ . It is worth noting that attempts at deducing a relationship of this type in the standard random phase approximation encounter a quite difficult problem of integrating complex expressions with respect to energy.

The main feature of the integral in Eq. (5) is that it diverges at  $\rho \rightarrow \rho_c$ , and, hence, the right-hand side of Eq. (5) inevitably turns to zero at some point beyond the Fermi surface. Thus, the Landau ground state ceases to be stable before the density reaches its critical value, where the frequencies of the collective spectrum become complex; consequently, the rearrangement of the single-particle degrees of freedom always precedes a collapse of the collective degrees of freedom. For instance, when calculating the spectrum  $\xi(p)$  of liquid  $^3\text{He}$ , one can verify by changing the parameter  $\beta$  characterizing the proximity of antiferromagnetic transition that the bifurcation in Eq. (2) occurs at a  $\beta$  value half as large as its value obtained in [2] for  $^3\text{He}$  at a pressure of 0.28 atm.

To illustrate how the rearrangement proceeds in the electronic system with strong AFs, we use the fact that the integrand in Eq. (5) has a peak at the point  $\mathbf{p}_1 = \mathbf{p} - \mathbf{Q}$ , so that the function  $n(\xi(\mathbf{p}_1))$  can be factored outside the integral at this point, to give the equation

$$\xi(\mathbf{p}) = \xi_{\mathbf{p}}^0 + fn(\xi(\mathbf{p} - \mathbf{Q})) \quad (6)$$

with the positive effective constant  $f \sim 1/\beta$ . This equation differs from an analogous equation in [7] in that  $\xi(\mathbf{p})$  in Eq. (6) is expressed through  $n(\mathbf{p} - \mathbf{Q})$  rather than through  $n(\mathbf{p})$ , as in the phenomenological model used in [7]. Despite the fact that both interactions differ rather strongly from each other, the results have much in common, although the model with AFs is more realistic

Equation (6) can conveniently be recast as a system of two equations

$$\begin{aligned} \xi_1 &= \xi_1^0 + fn(\xi_2), \\ \xi_2 &= \xi_2^0 + fn(\xi_1), \end{aligned} \quad (7)$$

where  $\xi_1 = \xi(\mathbf{p})$  and  $\xi_2 = \xi(\mathbf{p} - \mathbf{Q})$ . In deriving Eqs. (7), it was taken into account that  $\xi(\mathbf{p} - 2\mathbf{Q}) = \xi(\mathbf{p})$ . This system can be solved graphically (see Fig. 1). Each of

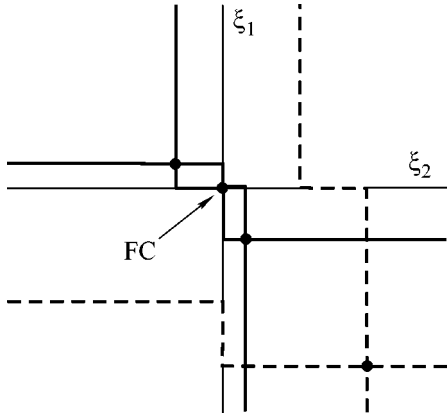


**Fig. 1.** Graphical solution to the system of Eqs. (7) for two parameter sets. One of them (dashed lines) corresponds to a single intersection, and the other (solid lines), to three intersections.

the right-hand sides in Eqs. (7) has the form of a rectangular kink in the  $(\xi_1, \xi_2)$  plane, the kink being “fixed” to the  $\xi_2$  axis in the first case and to the perpendicular  $\xi_1$  axis in the second case. As a rule, the parameters  $\xi_1^0$ ,  $\xi_2^0$ , and  $f$  in system (7) are such that both kinks (or either of them) lie far from the origin of coordinates. In this case, the lines (dashed in Fig. 1) intersect only at a single point which determines the only solution to the system of equations for the spectrum  $\xi(\mathbf{p})$ . If two inequalities

$$-f < \xi_p^0 < 0, \quad -f < \xi_{\mathbf{p}-\mathbf{Q}}^0 < 0, \quad \mathbf{p} \in C, \quad (8)$$

are fulfilled simultaneously, the kinks may simultaneously pass through the origin, so that the lines may intersect at three points instead of one, as seen in Fig. 1. An analysis shows that conditions (8) may be fulfilled in the vicinity of the van Hove points and only if they are situated below the Fermi surface.

The solution  $\xi_1 = 0, \xi_2 = 0$  corresponding to the middle intersection point always lies at the origin of coordinates and can be obtained from the variational principle [8]

$$\delta E_0 / \delta n(\mathbf{p}) = \mu, \quad \mathbf{p} \in C, \quad (9)$$

where the energy functional is

$$E_0 = \sum_{\mathbf{p}} \left[ \varepsilon_{\mathbf{p}}^0 n(\mathbf{p}) + \frac{1}{2} f n(\mathbf{p}) n(\mathbf{p}-\mathbf{Q}) \right]. \quad (10)$$

By varying this expression with respect to  $n(\mathbf{p})$ , one indeed obtains Eq. (6). Inasmuch as the left-hand side of this equation is nothing but the quasiparticle energy  $\varepsilon(\mathbf{p})$ , both the direct solution to Eq. (6) and the variational Eq. (9) give the same result  $\xi(\mathbf{p}) = \varepsilon(\mathbf{p}) - \mu \equiv 0$  for a group of states corresponding to the fermion condensate (FC) and occupying certain domains in the

Brillouin zone, the boundaries of these domains being determined from the same Eq. (9).

As an illustration, Fig. 2 shows the Fermi surface obtained by solving system (7) with a 2D tide-binding spectrum  $\varepsilon_{\mathbf{p}}^0 = -e_0[\cos(ap_x) + \cos(ap_y) - 2t \cos(ap_x)\cos(ap_y)]$ , where the parameter  $t = 0.45$  and the constant  $f = 0.5e_0$ . One can see that the Fermi surface consists of the FC patches concentrated near the van Hove points and connected with each other by arcs. For the momentum distribution in the domains occupied by the fermion condensate, one has after substituting  $\xi(\mathbf{p}) = 0$  into Eq. (6)

$$n(\mathbf{p}) = -\xi_{\mathbf{p}-\mathbf{Q}}^0 / f, \quad \mathbf{p} \in C, \quad (11)$$

which has nothing to do with the standard jump on the FS arc. Note that, for fixed parameters of the spectrum  $\xi_p^0$  and for a fixed constant  $f$ , the relative area of the FC patches in the model considered depends on the zone filling that is determined by the chemical potential  $\mu$ . For a certain optimal filling in the vicinity of half-filling, this area achieves its maximal value. The parameters used in the calculation are so chosen that the Fermi surface in Fig. 2 corresponds to the maximal phase volume of fermion condensate. The coexistence of the FC domains and usual FS domains is yet another distinction between the model with AFs and the models used in [7, 9], where the usual FS arcs are absent, while the “straits” between the FC domains are also filled with the fermion condensate.

We now make sure that the rearrangement of the Landau ground state and the formation of the FC domains are energetically favorable. By substituting distribution (11) into Eq. (10) for energy and subtracting the energy calculated with allowance made for the Fermi filling, one gets after simple algebra for the difference  $\Delta E = -(f/2) \sum_{\mathbf{p} \in C} (1 + \xi_{\mathbf{p}}^0 / f)(1 + \xi_{\mathbf{p}-\mathbf{Q}}^0 / f)$ . Due to inequality (8), this difference is negative; i.e., the state with fermion condensate lies energetically lower than the Landau state.

Let us briefly discuss the role of regular terms, which are retained after separating singular part (4) from the amplitude  $F$ , e.g., the role of phonon contributions. First, the latter introduce effective mass and, hence, transform the LDA spectrum  $\xi_{\mathbf{p}}^0$ ; and, second, they modify, for the same reason, the parameters of antiferromagnetic exchange and, thus, give rise to the isotopic effect in the FC structure.

In our opinion, the following analogy is noteworthy in connection with variational condition (9). Recall that liquid differs from gas in that the functional  $E(\rho)$  either has a minimum or not. It is absent in gas (the gas density is determined by the boundary conditions), whereas liquids exist in the states near the minimum of this functional. By analogy, we can say that by the Landau theory of Fermi liquid is usually meant the Landau

theory of interacting Fermi gas, because the momentum distribution  $n(\mathbf{p})$  is determined not by the minimum of functional  $E(n)$  but by the boundary conditions in the form of the Pauli principle. In actuality, by the Landau theory of Fermi liquid should be meant the theory of fermionic states near the point where variational condition (9) is fulfilled.

The formulas obtained in this work can be used in the BCS description of the superfluid states of strongly correlated systems with fermion condensate. Note that, since the fermion condensate appears only if the van Hove points lie below the Fermi surface, the superconductivity in a system with fermion condensate is of the hole type. It is also worth noting that the problem of FC-excitation damping does not arise in the description of superfluidity, because the main damping channel (into two holes and a particle) is suppressed at energies lower than  $3|\Delta|$ . In the standard gap equation

$$\Delta(\mathbf{p}) = \int v(\mathbf{p}, \mathbf{p}_1) \frac{\Delta(\mathbf{p}_1)}{2E(\mathbf{p}_1)} d\tau_1 \quad (12)$$

with the irreducible four-pole kernel  $v(\mathbf{p}, \mathbf{p}_1)$  and the single-particle spectrum  $E(\mathbf{p}) = \sqrt{\xi^2(\mathbf{p}) + \Delta^2(\mathbf{p})}$ , the fermion condensation affects  $\xi(\mathbf{p})$  and changes dramatically the single-particle excitation spectrum of a superfluid system. Following [10], we retain only the AF contribution to  $v$ . Since this contribution is repulsive at the Fermi surface, the solution, if it exists, must have zeros. This becomes evident after factoring  $\Delta(\mathbf{p}_1)/2E(\mathbf{p}_1)$  outside the integral at the point  $\mathbf{p}_1 = \mathbf{p} - \mathbf{Q}$ , where the interaction has a peak. The gap equation in the FC patches then takes the form

$$\Delta(\mathbf{p}) = -f \frac{\Delta(\mathbf{p} - \mathbf{Q})}{2E(\mathbf{p} - \mathbf{Q})}, \quad (13)$$

where the constant  $f$ , being the integral of the interaction over the FC domain, is determined by the FC phase volume. It follows from Eq. (13) that  $E(\mathbf{p})E(\mathbf{p} - \mathbf{Q}) = f^2/4$  and, hence,  $E(\mathbf{p}) = f/2$  in the FC patches situated in the vicinity of the van Hove points connected by the vector  $\mathbf{Q}$ . As it follows from Eq. (13) that the gap changes sign upon turning through  $90^\circ$  from one FC patch to another, i.e., that the appearance of the fermion condensate does not affect this basic property of the  $d_{x^2-y^2}$ -pairing model [10, 6], the gap in the systems with fermion condensate also disappears on the diagonal of the Brillouin zone. If one neglects a small contribution of pairing to  $\xi(\mathbf{p} - \mathbf{Q})$ , then one can easily verify that the gap in the  $E(\varphi)$  spectrum is small at the Fermi surface away from the van Hove points, i.e., in the region where the fermion condensate is absent. A qualitative analysis of the solution to Eq. (12) is illustrated in Fig. 3. It is seen from this figure that the gap in the single-particle spectrum  $E(\varphi)$  does not change within the FC domain and decreases rapidly upon leaving the FC patch along the Fermi arc. The following two features of pairing in a system with fermion condensate are

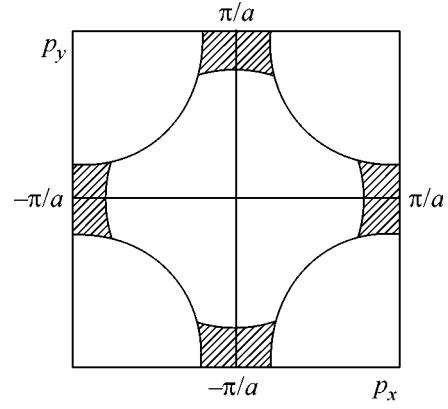


**Fig. 2.** Fermi surface for the ground state in model (10). The calculation was carried out for the optimum filling that provides the maximal area of FC domains (shaded).

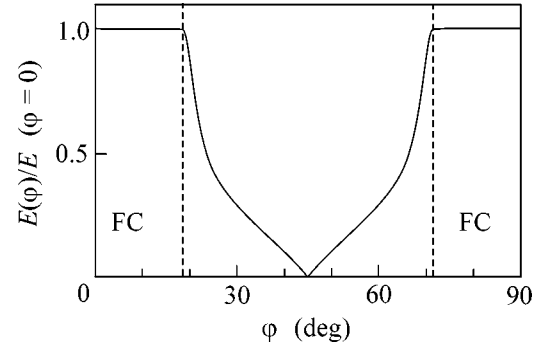


**Fig. 3.** Gap  $E(\varphi)$  in units of  $E(\varphi = 0)$  in the single-particle excitation spectrum at the Fermi surface.

also noteworthy. First, inasmuch as the gap  $E(\varphi) = f/2$  in the FC domains is determined by the FC phase volume, it is maximal at the optimum filling that provides the largest area of FC patches, so that the fillings lower and higher than the optimum can correspond to the same gaps. Second, the energy gain  $\sim \Delta$  [8] due to pairing in a system with fermion condensate is appreciably greater than the usual BCS gain  $\sim \Delta^2/\varepsilon_F$  in a system without FC. The solution to Eq. (12) fits the available experimental data on the gap structure in the spectra of 2D high- $T_c$  superconductors with square lattice [11, 12]. These data were derived from the photoemission spectra, and their accuracy is as yet low, so that the question of quantitative comparison between our results and the experiment remains open.

In summary, we have used the Landau-Pitaevski relation to separate the singular contribution of AFs from the interaction amplitude and have shown that the antiferromagnetic transition is preceded by the rearrangement of the single-particle degrees of freedom, giving rise to plateaus in the single-particle excitation spectrum. As a result of this rearrangement, the Fermi surface of the 2D high- $T_c$  superconductors with square lattice takes the form of FC patches situated near the

van Hove points and connected to each other by arcs. By retaining only the contribution of AFs in the pairing interaction, we have studied the manifestation of fermion condensate in the single-particle spectra of such superconductors at  $T = 0$  and found that the gap shape  $E(\varphi)$  in the spectrum at the Fermi surface agrees qualitatively with the available experimental data [11, 12] but differs from the shape in the  $d_{x^2-y^2}$  model. The qualitative check of our results is, likely, a matter of the immediate future.

This work was supported in part by the Russian Foundation for Basic Research (project no. 00-15-96590), the NSF (grant no. 9900713), and the McDonnell Center for Space Sciences. We are grateful to N.E. Zein and to C.M. Bender, J.C. Campuzano, J. Mesot, and M.R. Norman for discussion.

#### REFERENCES

1. A. B. Migdal, *Theory of Finite Fermi Systems and Applications to Atomic Nuclei* (Nauka, Moscow, 1967; Interscience, New York, 1967).
2. A. M. Dyugaev, Zh. Éksp. Teor. Fiz. **70**, 2390 (1976) [Sov. Phys. JETP **43**, 1247 (1976)].
3. A. A. Abrikosov, L. P. Gor'kov, and I. E. Dzyaloshinskii, *Methods of Quantum Field Theory in Statistical Physics* (Fizmatgiz, Moscow, 1962; Prentice-Hall, Englewood Cliffs, 1963).
4. J. W. Clark, V. A. Khodel, and M. V. Zverev, Yad. Fiz. **64**, 677 (2001) [Phys. At. Nucl. **64**, 619 (2001)].
5. V. A. Khodel', V. R. Shaginyan, and M. V. Zverev, Pis'ma Zh. Éksp. Teor. Fiz. **65**, 242 (1997) [JETP Lett. **65**, 253 (1997)].
6. P. Montoux, A. V. Balatsky, and D. Pines, Phys. Rev. Lett. **67**, 3448 (1991).
7. G. E. Volovik, Pis'ma Zh. Éksp. Teor. Fiz. **59**, 798 (1994) [JETP Lett. **59**, 830 (1994)].
8. V. A. Khodel' and V. R. Shaginyan, Pis'ma Zh. Éksp. Teor. Fiz. **51**, 626 (1990) [JETP Lett. **51**, 553 (1990)]; Condens. Matter Theor. **12**, 222 (1997).
9. V. A. Khodel, J. W. Clark, and V. R. Shaginyan, Solid State Commun. **96**, 353 (1995).
10. N. E. Bickers, D. J. Scalapino, and R. T. Scalettar, Int. J. Mod. Phys. B **1**, 687 (1987); N. E. Bickers, D. J. Scalapino, and S. R. White, Phys. Rev. Lett. **62**, 961 (1989).
11. H. Ding, M. R. Norman, J. C. Campuzano, *et al.*, Phys. Rev. B **54**, R9678 (1996).
12. M. R. Norman, in *High Temperature Superconductivity*, Ed. by S. E. Barnes, J. Ashkenazi, J. L. Kohn, and F. Zuo (American Inst. of Physics, Woodbury, 1999), p. 298.

*Translated by V. Sakun*

# ***P*-Odd Effects Observed in Neutron-Induced Reactions and Isospin Structure of Weak Nucleon–Nucleon Interaction**

**L. M. Smotrisky**

*Petersburg Nuclear Physics Institute, Russian Academy of Sciences, Gatchina, Leningrad region, 188350 Russia*  
*e-mail: smotrisky@mail.pnpi.spb.ru*

Received May 16, 2001

It is shown that, by introducing a resonance phase for two opposite-parity quasistationary states of the same spin, the observed sign dependence of *P*-odd effects in neutron-induced reactions can be matched with theoretical predictions. The proposed approach makes it possible to deduce information about the isospin structure of weak nucleon–nucleon interaction. © 2001 MAIK “Nauka/Interperiodica”.

PACS numbers: 25.40.Fq; 24.80.+y; 21.30.Fe

Parity-violation effects observed in neutron–nucleus interactions belong to the class of so-called interference phenomena. Eventually, such effects depend on the product of reaction amplitudes rather than on their squares. In view of this, the sign dependence of the effects in question is of paramount importance, since it opens new possibilities both in interpreting experimental data and in seeking a viable theoretical description of the phenomenon.

Parity-odd (*P*-odd) effects arise owing to the weak-interaction-induced mixing of *s*- and *p*-wave resonances—that is, continuum nuclear levels (compound resonances) occurring above the neutron binding energy in a nucleus. Since the structure of *s*- and *p*-wave resonances is very intricate (they are of a multiparticle nature), it is common practice to make use of statistical approaches, which lead to a random sign of *P*-odd effects.

In recent years, however, there appeared some data suggesting that a regular mechanism is responsible for the formation of signs of *P*-odd effects [1–3]. On the basis of these results, the entire body of currently available data on the subject was analyzed in [4], where it was found that the sign of the *P*-odd effect can be described by taking into consideration the properties of a nuclear system that are governed by strong interaction. These include the resonance positions with respect to the neutron energy, the spin factor, and the parity of a *p*-wave resonance. In particular, the sign of the parity-violating (*PV*) effect in target nuclei whose ground states are of positive parity can be described by the simple formula

$$\text{sgn}(PV) = \text{sgn}[(E_n - E_s)(E_n - E_p)(E_s - E_p)], \quad (1)$$

where  $E_n$  is the neutron energy, while  $E_s$  and  $E_p$  are the energies of, respectively, the *s*- and the *p*-wave reso-

nances involved. Equation (1) is valid for a more general case, that of a thermal point (away from the *p*-wave resonance). In the case of resonance measurements, where the neutron energy coincides with the energy of the *p*-wave resonance, the pattern is incomplete.

It could seem that the regular behavior of the signs of *P*-odd effects that is observed experimentally is at odds with the commonly accepted statistical model of dynamical enhancement [5, 6]. It will be shown below that the inclusion of a resonance phase makes it possible to fit theoretical predictions to experimental data [7] and to deduce, on the basis of experimental data, information about the isospin structure of weak nucleon–nucleon interaction.

Experiments usually study *P*-odd effects of two classes. According to the terminology adopted in [8], the first class includes *P*-odd effects that arise in the interference of relevant amplitudes in the reaction final state. In this case, one observes a *P*-odd (pseudoscalar) correlation of the  $\sigma_n \cdot \mathbf{k}$  type, where  $\sigma_n$  is the neutron spin and  $\mathbf{k}$  is the outgoing-particle momentum. For the sake of simplicity, we will henceforth imply that  $\mathbf{k}$  is the momentum  $\mathbf{k}_\gamma$  of the photon emitted in a ( $n, \gamma$ ) reaction. An observation of the *P*-odd effect then amounts to determining the coefficient of asymmetry  $a_\gamma$  in an angular distribution of the form  $W(\theta) \sim 1 + a_\gamma \sigma_n \cdot \mathbf{k}_\gamma$ . The *P*-odd circular polarization  $P_\gamma$ , which differs from  $a_\gamma$  by the absence of the spin factor  $A_s$ , belongs to the same class of observables.

The second class embraces *P*-odd effects in neutron optics [5, 6]. In this case, one observes a correlation of the form  $\sigma_n \cdot \mathbf{k}_n$ , where  $\mathbf{k}_n$  is the neutron momentum. This can be the *P*-odd effect arising in the total cross section when longitudinally polarized opposite-helicity neutrons propagate through a sample or a rotation of the

plane of polarization of transversely polarized neutrons traversing a sample ( $\Phi_{pv}$ ). The  $P$ -odd effect in the total cross section is defined as  $P_{\text{tot}} = (\sigma^+ - \sigma^-)/(\sigma^+ + \sigma^-)$ , where  $\sigma^+$  and  $\sigma^-$  are the total cross sections for longitudinally polarized neutrons whose spins are, respectively, parallel and antiparallel to the neutron momentum.

The magnitudes of  $P$ -odd effects can be expressed in terms of three basic amplitudes, which are denoted by  $f_1, f_2$ , and  $f_3$  [9]. The amplitude  $f_1$  describes the process in which neutron capture into the  $s$ -wave compound state of nucleus  $A$  is followed by its decay leading to the formation of nucleus  $A + 1$  and to the emission of a photon whose multipolarity can be, for example,  $M1$ . The amplitude  $f_2$  is that for the process where neutron capture into the  $p$ -wave state is accompanied by the emission of an  $E1$  photon. The amplitude  $f_3$  describes neutron capture into the  $s$ -wave state, the population of the  $p$ -wave state due to weak interaction, and its subsequent decay accompanied by the emission of an  $E1$  photon. For the  $P$ -odd observables, we can then obtain the expressions<sup>1</sup>

$$a_\gamma \sim \frac{\text{Re}(f_1 f_3^*)}{|f_1|^2}, \quad (2)$$

$$P_{\text{tot}} \sim \frac{\text{Re}(f_2 f_3^*)}{|f_2|^2}. \quad (3)$$

For the  $P$ -odd observables, the substitution of the explicit expressions for the amplitudes from [9] into (2) and (3) leads to formulas that are usually used in comparing experimental data with theoretical predictions. Specifically, we have

$$a_\gamma = \frac{2W_{sp}}{E - E_p} A_s \sqrt{\frac{\Gamma_p^\gamma}{\Gamma_s^\gamma}}, \quad (4)$$

$$P_{\text{tot}} = P_{\text{tot}}^\gamma = -\frac{2W_{sp}}{E - E_s} x \sqrt{\frac{\Gamma_s^n}{\Gamma_p^n}}. \quad (5)$$

where  $W_{sp} \equiv \langle p|V_{sp}|s\rangle$  is the matrix element of weak interaction between the  $s$ - and the  $p$ -wave state;  $\Gamma_{s,p}^\gamma$  and  $\Gamma_{s,p}^n$  are the gamma and neutronic widths of the  $s$ - and the  $p$ -wave state, respectively; and  $x = \sqrt{\Gamma_{p1/2}^n/\Gamma_p^n}$ ,  $\Gamma_{p1/2}^n$  being the partial-wave neutron width of the  $p$ -wave resonance with respect to its capture through the channel where the total angular momentum of the captured neutron is  $j = 1/2$ . In deriving expressions (4) and (5), the potential phases were disregarded because they are small for slow neutrons ( $kR \ll 1$ ). As is sug-

gested by the physics behind the derivation of the amplitudes and of  $W_{sp}$ , each of these expressions is characterized by the sign inherent in it.

The following special features of Eqs. (2)–(5) are worthy of special note. For  $P$ -odd effects of the first class [Eqs. (2), (4)], the input reaction channel is common (neutron capture into the  $s$ -wave state), whereas the effect arises in the output reaction channel owing to the interference between the amplitudes for the decays of the  $s$ - and the  $p$ -wave state. In the second class [Eqs. (3), (5)], the pattern is inverse: the amplitudes interfere in the input reaction channel (these are those for neutron capture into the  $s$ - and the  $p$ -wave state), the output reaction channel being common (decay of the  $p$ -wave state).

The most interesting point is that information about the common reaction channel is canceled in either case. In view of this, expression (5) can be derived by a different method, that which is based on the elastic reaction channel (as represented by the amplitude  $f_3$  in the presence of neutron emission), along with the use of the optical theorem, and which was adopted, for example, in [10]. This was the way in which such effects were considered originally. However, the question of where  $P$ -odd effects arise—in the elastic or in an inelastic channel—is of fundamental importance. In [11], it was shown experimentally that  $P$ -odd effects in neutron optics are due to radiative capture.

Following the derivation of expressions (3) and (5) and adopting the same line of reasoning as in [9], one can see that the two types of  $P$ -odd effects have a common origin associated with the capture process: they have the same weak-interaction amplitude ( $f_3^*$ ), and either effect depends on the real part of the product of the amplitudes. Furthermore, it is not accidental that neither expression (4) nor expression (5) depends on the common reaction channel. From the physical point of view, this seems bizarre. Neutron capture into the  $s$ -wave resonance is the channel common to  $P$ -odd effects belonging to the first class. Obviously, the situation where the resonance is to the left of the neutron-energy value must be different from that where the resonance is to the right of it. This problem is solved by introducing a resonance phase for a quasistationary state [12] (neutron resonances in our case). The inclusion of a resonance phase that has zero asymptotic value below the resonance and the asymptotic value of  $\pi$  above the resonance generates the dependence on the sign of  $E_n - E_s$  in expression (4).

There only remains the question of how one can introduce the dependence on  $E_s - E_p$  in the theoretical scheme used. Such a dependence arises in perturbatively calculating the matrix element of weak interaction and the mixing coefficient  $\alpha$  [13],

$$\alpha = \frac{\langle p|V_{sp}|s\rangle}{E_s - E_p}. \quad (6)$$

<sup>1</sup> The amplitude  $f_4$  was disregarded because of its smallness in relation to  $f_3$ .

For the case of a quasistationary state, the denominator in (6) must be replaced by  $E - E_p + i\Gamma_p/2$  [5], where  $\Gamma_p$  is the total width of the  $p$ -wave resonance. Thus, the dependence on  $E_s$  seems to be effectively removed upon going over to the quasistationary problem, but the introduction of the resonance phase ( $\phi_{\text{res}}$ ) for two resonances (an  $s$ - and a  $p$ -wave one) coupled by weak interaction restores such a dependence. From experimental data, it follows that this phase must be constant between the resonances and be equal to  $\pi$  if  $E_s < E_p$  and to zero if  $E_s > E_p$ . The resonance phase introduced in this way renders the theoretical predictions consistent with the empirical formula (1) for  $P$ -odd effects belonging to the first class.

For  $P$ -odd effects from the second class, the situation is somewhat more intricate. As a rule, they are studied in the vicinity of a  $p$ -wave resonance, where there are features in the energy dependences: at  $E_p$ ,  $P_{\text{tot}}$  attains a maximum, while  $\Phi_{pv}$  goes through zero. An analysis of expression (3) reveals that the amplitude  $f_3^*$  involves the phase of a free motion of the  $p$  wave. Since the matrix element of weak interaction is a pure imaginary quantity, it compensates for this phase, which is equal to  $\pi/2$  ( $e^{i\pi/2} = i$ ) with respect to the  $s$  wave [5]. Thus, we see that, in relation to (2), expression (3) contains an extra  $p$  wave that is associated with the amplitude  $f_2$ . There arises the additional phase  $\phi(f_2) = \pi/2$ , which must be subtracted, according to the experimental situation, from the resonance phase. As a result, the total phase vanishes at the energy of the  $p$ -wave resonance, so that the sign of  $P_{\text{tot}}$  is determined by the energy denominator in expression (5). Off the resonance, the total phase takes the values of  $+\pi/2$  and  $-\pi/2$ , with the result that the effect decreases faster.<sup>2</sup>

For the sign of  $P_{\text{tot}}$ , we can now formulate a simple rule. If the  $s$ -wave resonance involved occurs to the right (left) of a given  $p$ -wave resonance, the sign of the effect is positive (negative). On this basis, one can explain the sign correlation in  $^{232}\text{Th}$  [3], which is widely discussed in the literature. In [3], the quantity  $P_{\text{tot}}$  was studied for a number of resonances in  $^{232}\text{Th}$ . It was surprising that, for ten  $p$ -wave resonances where the  $P$ -odd effect was observed, the sign of the effect was positive. The analysis performed in [4] revealed that, for these ten  $p$ -wave resonances, the contribution of all  $s$ -wave resonances occurring to the right of a given one is greater than the analogous contribution from the  $s$ -wave resonances occurring to the left. It is this circumstance that leads to a positive sign of the effect. In [14], the entire body of information necessary for the relevant calculation is presented for the  $p$ -wave resonance at  $E_p = 8.35$  eV. However, the result quoted

<sup>2</sup> It should be noted that, because of a nonzero total resonance width, the resonance phase is not equal precisely to zero or  $\pi$ . This circumstance must be taken into account in the total phase.

there is based on the assumption that all  $s$ -wave resonances contribute at random.

By introducing a resonance phase, it is possible to remove the discrepancy between the signs in globally describing  $P$ -even effects at the  $p$ -wave resonances in the  $^{113}\text{Cd}$  and  $^{117}\text{Sn}$  nuclei [15, 16].

According to [5, 12], the resonance phase can be expressed in terms of the parameters of the  $s$ - and  $p$ -wave resonances as

$$\phi_{\text{res}}(E) = \text{arccot} \left[ \frac{(E - E_s)(E - E_p) + \Gamma_s \Gamma_p / 4}{(E - E_s)\Gamma_p / 2 - (E - E_p)\Gamma_s / 2} \right]. \quad (7)$$

Thus, the introduction of a resonance phase in a theoretical consideration makes it possible to reconstruct information about the common reaction channel and, in conjunction with the energy denominators in Eqs. (4) and (5), to describe the experimentally observed sign dependence (1) of  $P$ -odd effects.

From the aforesaid, we can draw the following conclusion. In studying a weak-interaction-induced process (recall that one aims here at observing a  $P$ -odd correlation), the sign of the  $P$ -odd effect can be described by allowing only for strong and electromagnetic interaction. It follows that the sign associated with weak interaction is constant in all such cases [17]. This result, which seems paradoxical at first glance, can be explained from the viewpoint of weak-interaction physics.

At low energies,  $P$ -odd nuclear forces are described by a set of six constants that determine the exchanges of  $\pi$ ,  $\rho$ , and  $\omega$  mesons between nucleons [18, 19]. Such exchanges correspond to weak charged and neutral currents and are governed by the isospin selection rules

$$|\Delta T| = 0, 1, 2. \quad (8)$$

It is well known [20, 21] that the contribution of  $|\Delta T| = 1$  weak neutral currents to  $P$ -odd nuclear forces is strongly suppressed. According to the estimates presented in [22], isotensor interaction ( $|\Delta T| = 2$ ) makes but a small contribution that vanishes upon summation over the nucleon core [23]. It follows that it is the isoscalar component of weak nucleon–nucleon interaction [17] that predominantly manifests itself in neutron-induced reactions. This means that, if the isospin of the neutron resonances involved is zero, the formation of the effect is always controlled by the same set of constants, which yields the same sign of weak interaction, in agreement with experimental data.

The theory of the nucleus has yet to resolve a number of problems posed by advances in experimental investigations of  $P$ -odd effects. These problems include those of (i) a complete correlation of the signs of the amplitudes and  $W_{sp}$  in Eqs. (4) and (5), as well as of the signs of the amplitudes of  $P$ -even and  $P$ -odd effects in fission [24, 25]; (ii) the isospin in intermediate-mass and heavy nuclei as a good quantum number; and

(iii) construction of an effective single-particle weak-interaction nuclear potential.

In conclusion, I would like to thank my colleagues from the Department of Neutron Investigations at the Petersburg Nuclear Physics Institute (Russian Academy of Sciences, Gatchina).

This work was supported by the state program Fundamental Nuclear Physics (grant no. 134-08).

#### REFERENCES

1. V. A. Vesna, É. A. Kolomensky, V. M. Lobashev, *et al.*, Pis'ma Zh. Éksp. Teor. Fiz. **36**, 169 (1982) [JETP Lett. **36**, 209 (1982)].
2. L. M. Smotrisky and V. N. Dobrynin, Preprint PIYaF-2041 (Institute of Nuclear Physics, Gatchina, 1995).
3. S. L. Stephenson, J. D. Bowman, B. E. Crawford, *et al.*, Phys. Rev. C **58**, 1236 (1998).
4. L. M. Smotrisky, Preprint PIYaF-2307 (Institute of Nuclear Physics, Gatchina, 1999); L. M. Smotrisky, Yad. Fiz. **64** (8) (2001) (in press) [Phys. At. Nucl. **64** (2001)].
5. O. P. Sushkov and V. V. Flambaum, Usp. Fiz. Nauk **136**, 3 (1982) [Sov. Phys. Usp. **25**, 1 (1982)].
6. V. E. Bunakov and V. P. Gudkov, Nucl. Phys. A **401**, 93 (1983).
7. L. M. Smotrisky, Preprint PIYaF-2418 (Institute of Nuclear Physics, Gatchina, 2001).
8. Yu. G. Abov, O. N. Ermakov, I. L. Karpikhin, *et al.*, Nucl. Instrum. Methods Phys. Res. A **284**, 80 (1989).
9. V. V. Flambaum and O. P. Sushkov, Nucl. Phys. A **435**, 352 (1985).
10. V. P. Alfimenkov, Usp. Fiz. Nauk **144**, 361 (1984) [Sov. Phys. Usp. **27**, 797 (1984)].
11. E. A. Kolomensky, V. M. Lobashev, A. N. Pirozhkov, *et al.*, Phys. Lett. B **107B**, 272 (1981).
12. L. D. Landau and E. M. Lifshitz, *Course of Theoretical Physics*, Vol. 3: *Quantum Mechanics: Non-Relativistic Theory* (Fizmatgiz, Moscow, 1963; Pergamon, New York, 1977); L. Valentin, *Physique subatomique (noyaux et particules)* (Hermann, Paris, 1982; Mir, Moscow, 1986), Vol. 1.
13. I. S. Shapiro, Usp. Fiz. Nauk **95**, 647 (1968) [Sov. Phys. Usp. **11**, 582 (1969)].
14. C. M. Frankle, J. D. Bowman, J. E. Bush, *et al.*, Phys. Rev. C **46**, 778 (1992).
15. V. P. Alfimenkov, S. B. Borzakov, Yu. D. Mareev, *et al.*, Yad. Fiz. **52**, 927 (1990) [Sov. J. Nucl. Phys. **52**, 589 (1990)].
16. V. P. Alfimenkov, S. B. Borzakov, Yu. D. Mareev, *et al.*, Kratk. Soobshch. Ob'edin. Inst. Yad. Issled., Dubna, No. 10-85, 19 (1985).
17. L. M. Smotrisky, in *Proceedings of the 12th International Symposium on High-Energy Spin Physics, SPIN 96*, Ed. by C. W. de Jager *et al.* (World Scientific, Singapore, 1997), p. 657; L. M. Smotrisky, Yu. E. Loginov, and P. A. Sushkov, in *Proceedings of the 9th International Symposium on Capture Gamma-Ray Spectroscopy and Related Topics*, Ed. by G. L. Molnar *et al.* (Springer-Verlag, New York, 1997), p. 628; L. M. Smotrisky, in *Abstract of Contributed Papers of the International Nuclear Physics Conference, Paris, 1998*, p. 733; L. M. Smotrisky, in *International Workshop on Parity Violation in Atomic, Nuclear and Hadronic Systems, ECT\* Trento, 2000* (unpublished).
18. E. G. Adelberger and W. C. Haxton, Ann. Rev. Nucl. Part. Sci. **35**, 501 (1985).
19. G. A. Lobov, Nucl. Phys. A **577**, 449 (1994).
20. S. A. Page, H. C. Evans, G. T. Ewan, *et al.*, Phys. Rev. C **35**, 1119 (1987).
21. M. Bini, T. F. Fazzini, G. Poggi, *et al.*, Phys. Rev. C **38**, 1195 (1988).
22. M. Horoi, G. Clausnitzer, B. A. Brown, *et al.*, Phys. Rev. C **50**, 775 (1994).
23. W. C. Haxton, Invited talk on Workshop on Parity Violation in Hadronic System, TRIUMF, May 1987.
24. V. A. Vesna, V. A. Knyaz'kov, É. A. Kolomensky, *et al.*, Pis'ma Zh. Éksp. Teor. Fiz. **31**, 704 (1980) [JETP Lett. **31**, 663 (1980)].
25. A. Ya. Aleksandrovich, T. K. Zvezdkina, D. V. Nikolaev, *et al.*, Yad. Fiz. **39**, 805 (1984) [Sov. J. Nucl. Phys. **39**, 509 (1984)].

*Translated by A. Isaakyan*

## Advances in the Investigation of the Extraction of a Proton Beam from the U-70 Accelerator with the Aid of Bent Single Crystals

A. G. Afonin<sup>1</sup>, V. T. Baranov<sup>1</sup>, V. M. Biryukov<sup>1</sup>, V. I. Kotov<sup>1</sup>, V. A. Maishev<sup>1</sup>,  
V. I. Terekhov<sup>1</sup>, E. F. Troyanov<sup>1</sup>, Yu. S. Fedotov<sup>1</sup>, V. N. Chepegin<sup>1</sup>, Yu. A. Chesnokov<sup>1\*</sup>,  
Yu. M. Ivanov<sup>2</sup>, V. Guidi<sup>3</sup>, G. Martinelli<sup>3</sup>, M. Stefanchik<sup>3</sup>, D. Vincenzi<sup>3</sup>,  
D. Trboevich<sup>4</sup>, V. Scandale<sup>5</sup>, and M. B. H. Breese<sup>6</sup>

<sup>1</sup> Institute for High Energy Physics, Protvino, Moscow region, 142284 Russia

\* e-mail: chesnokov@mx.ihep.su

<sup>2</sup> Petersburg Nuclear Physics Institute, Russian Academy of Sciences, Gatchina, Leningrad region, 188350 Russia

<sup>3</sup> Università di Ferrara, via Savonarola 9, I-44100 Ferrara, Italy

<sup>4</sup> Brookhaven National Laboratory, PO Box 5000, Upton, NY 11973-5000, USA

<sup>5</sup> CERN (European Laboratory for Particle Physics), CH-1211 Genève 23, Switzerland

<sup>6</sup> University of Surrey, Guilford, Surrey GU2 5XH, UK

Received May 30, 2001

The efficiency of the extraction of a beam from an accelerator is radically improved owing to the application of short crystals of length up to 1.8 mm bent through a small angle of about 1 mrad. This success is due to an increase in the multiplicity of particle transmission through the crystal used. A record efficiency of the extraction of 70-GeV protons in excess of 80% is achieved experimentally, this result being in agreement with theoretical predictions. It is shown that the crystal can efficiently operate at the injection energy of 1.3 GeV. © 2001 MAIK "Nauka/Interperiodica".

PACS numbers: 29.27.Ac

A new method for extracting beams from accelerators that is based on the application of bent crystals is being developed in several laboratories worldwide [1–5].

This method has a number of appealing features. Specifically, it admits a simple implementation and is compatible both with the collider mode and with mode of internal targets; moreover, the intensity of the resulting beam exhibits but small pulsations. The crystal used has a minimal septum thickness; therefore, it is very convenient for application in loss-localization systems as a coherent scatterer as well.

For a long time, however, attempts at achieving a high efficiency of extraction have been futile, since but a small number of particles are captured into the channeling regime when the beam from an accelerator traverses the crystal only once. One possible idea to increase sharply the efficiency of extraction is based on the application of a very short crystal [6, 7]. In long crystals bent through large angles previously in use, the losses of particles in dechanneling were great. In the case of a short crystal, the efficiency is improved not only owing to the reduction of dechanneling-induced losses of particles but also owing to less intense scattering over the crystal length. Concurrently, the mecha-

nism associated with an increase in the mean number of particle transmissions through the crystal comes into play, contributing to the improvement of the efficiency. Even the first experimental studies along these lines [3–5] at the 70-GeV accelerator installed at the Institute for High Energy Physics (IHEP, Protvino) led to a significant improvement of the parameters of extraction in relation to known world data: the intensity of extraction of a 70-GeV proton beam was in excess of  $10^{11}$  protons per spill at an efficiency of about 40%. In that experiment, use was made of short silicon crystals 6 and 5 mm long that were bent through angles of 1.7 and 1.5 mrad, respectively, according to different technologies yielding P- and O-shaped constructions, which are described in [3–5].

These technologies for preparing bent crystals have been developed further. Through creating new crystals of shorter length and better polished and bent, the efficiency of extraction was pushed up to 85%.

Presently, a few crystals are arranged at the U-70 accelerator. Their positions are chosen in such a way that bent crystals appear to be the first step in the slow-extraction system. The properties of the crystals are listed in the table. Crystals in the shape of strips (P type) and O-shaped crystals have orientations of

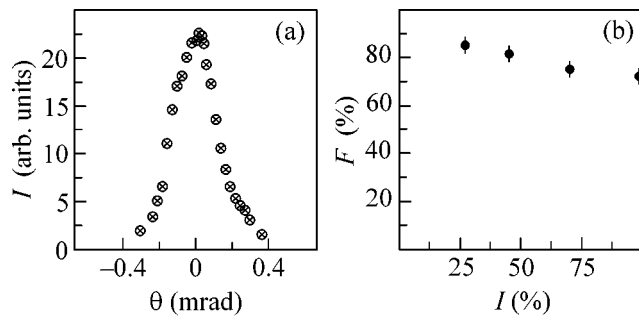


**Fig. 1.** (a) Intensity of the extracted beam versus the orientation of crystal no. 1; (b) efficiency  $F$  of beam extraction with the aid of crystal no. 1 versus the intensity  $I$  of the beam guided to the crystal (in percent of the intensity of the beam circulating in the U-70 accelerator).

Si(111) and Si(110), respectively. A specially generated local distortion of the orbit ensured transportation of the beam to the working crystal. The arrangement of equipment and instruments for diagnostics and the features of the beam in the accelerator were described in detail elsewhere [3–5].

All instruments for beam diagnostics (TV system of observation, monitors of losses, profilometers, equipment for measurement of the intensity) were preliminarily tested in the fast-extraction mode and calibrated with the aid of a current transformer. According to the results of the calibration, the absolute error in measurements of the extracted-beam intensity was within 2% [8]. The background conditions were periodically measured when the crystal was disoriented and when it was removed from the accelerator beam. The measured background level, together with the apparatus noise, did not exceed 3% of the channeled-beam intensity. From the measurements of the intensity of the circulating beam prior to and after the extraction, the beam fraction delivered to the crystal was determined with a systematic error of about 1%. With allowance for all

factors, the total systematic error in measuring the efficiency amounted to about 4%. The efficiency of extraction (that is, the ratio of the extracted-beam intensity to the intensity of the beam delivered to the crystal) was determined in each cycle of accelerator operation. For each experimental point, we collected statistics over a few hundred cycles. A feedback monitor based on a phototube equipped with a scintillator was used to ensure a uniform transportation of the beam to the crystal.

The best result was obtained with the shortest crystals nos. 1 and 6, which had a length of 2 and 1.8 mm, respectively, and which were manufactured in the form of narrow strips. Figure 1 displays the results of our investigations with crystal no. 1, which made it possible to achieve the extraction efficiency of  $(85 \pm 2.8)\%$  at the beam intensity in the accelerator of  $1 \times 10^{12}$  particles per spill. Further investigations are expected to establish the degree to which it is possible to increase the intensity of the beam extracted with the aid of this crystal.

Crystal no. 6 was used as a coherent scatterer in the loss-localization system. It was arranged at a distance of 20 m upstream of the beam collimator, and  $(85 \pm 2.8)\%$  of particles incident on this crystal were scattered into the collimator body. The results obtained by measuring the beam profile at the collimator inlet are shown in Fig. 2 for various modes. As might have been expected, guiding particles directly to the collimator edge (Fig. 2a) leads to very small parameters of particle acceptance, which are concentrated near the edge; as a result, the efficiency of collimation is reduced. The case illustrated in Fig. 2b corresponds to a disoriented crystal, while the case in Fig. 2c is that in which the crystal is oriented and in which the majority of the particles are thrown into the interior of the collimator. The graph in Fig. 2d represents the situation where the beam is thrown into the collimator by a kicker magnet. Delivery by the kicker magnet was used to calibrate the measure-

#### Properties of the crystals used

Crystal number	Position, number of a magnetic block	Type	Angle, mrad	Length $\times$ height $\times$ thickness, mm <sup>3</sup>	Efficiency	Comments
1	106	P	1.0	$2.0 \times 35 \times 0.5$	85	Extraction scheme 106-24-26
					80	Extraction scheme 106-20-22
2	106	O	0.7	$3.5 \times 5.0 \times 0.7$	60	Particle flux is $\sim 2 \times 10^{20}/\text{cm}^2$ 70 GeV 1.3 GeV
3	19	P	2.0	$5.0 \times 45 \times 0.5$	67	
4	19	O	2.1	$5.0 \times 5.0 \times 0.7$	65	
5	19	O	2.3	$5.0 \times 5.0 \times 0.6$	45	
6	84	P	0.8	$1.8 \times 27 \times 0.5$	85	
					20	
7	84	O	1.7	$2.5 \times 5.0 \times 0.5$	60	
8	86	P	1.4	$4.0 \times 45 \times 0.5$	65	

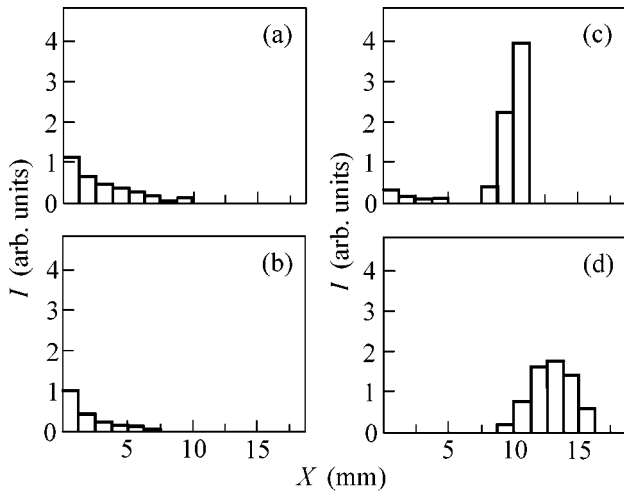


**Fig. 2.** Beam profiles measured at the collimator end face: (a) the case where there is no crystal and where the beam is guided directly to collimator; (b) the case where a disoriented crystal is inserted in a beam; (c) the case where an oriented crystal is inserted in a beam; and (d) the case where there is no crystal and where beam is guided by a kicker magnet.

ments of the fraction of the beam deflected by the crystal.

In applying a crystal, the radiation levels downstream of the collimator were reduced considerably.

The generalized experimental results obtained by measuring the efficiency of beam extraction implemented with the aid of crystals having different length values (see table) are presented in Fig. 3, along with the results of a simulation that took into account particle transport in the crystal (according to the CATCH code [9]) and many turns of motion in the accelerator. It can

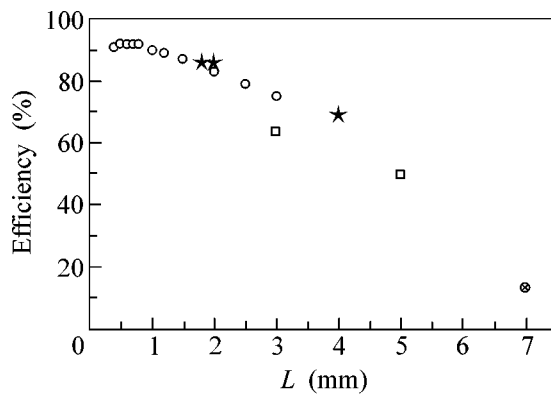


**Fig. 3.** Efficiency of proton-beam extraction with aid of a crystal according to measurements at 70 GeV: (★) results of 2000, (□) results of 1999 and 2000, (⊙) results of 1997, and (○) theoretical prediction (EPAC'2000 [11]) for the efficiency of extraction for a deflector having an ideal bend through 0.9 mrad.

be seen that the experimental data comply well with the results of the calculations.

The designed short crystals of length about 1 mm along the beam can be used not only at high-energy accelerators but also at particle energies of about 1 GeV. By way of example, we indicate that the first tests of the deflection of protons of energy 1.3 GeV (U-70 synchrotron injection energy) were performed at the U-70 accelerator. The profile of the beam deflected by crystal no. 6 is shown in Fig. 4 for the conditions specified above. A feature peculiar to this case is that the transmitted particles undergo intense Coulomb scattering within the crystal. The root-mean-square scattering angle of about 1 mrad is commensurate with angle of the crystal bend. Even in this case, however, channeled particles constitute a sizable fraction (about 50%) of the beam delivered to the crystal. According to estimates, the corresponding efficiency of delivery of the beam channeled by the crystal is about 20%. In principle, a further optimization of short crystals by applying a new technology for their growth [10] will make it possible to achieve, for low energies (less than 1 GeV), an extraction efficiency as high as that for 70 GeV.

At the IHEP accelerator, the use of a crystal for extracting a beam and for directing it to a facility intended for studying rare *K*-meson decays made it possible to increase, over two months of operation, the number of events collected worldwide for these decays by a factor of 40 [11]. We note that two internal targets that generated secondaries for other experiments operated in this mode along with the device that extracted protons with the aid of a crystal.

In summary, the results of our experiments show that, over a wide energy range, bent crystals can be suc-

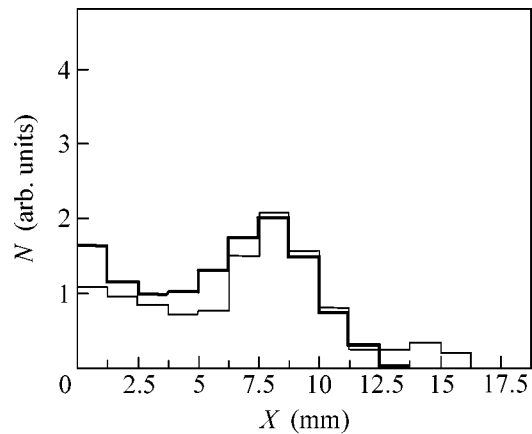


**Fig. 4.** Profile of a 1.3-GeV proton beam as measured at the collimator end face for the case where use is made of crystal no. 6. The thin line represents the simulated profile of particles channeled and scattered in the crystal, the motion of the particles in the accelerator ring being taken into account.

cessfully used to extract and collimate beams at accelerators.

This work was supported by the Russian Foundation for Basic Research (project no. 01-02-16229) and by a joint grant from INTAS and CERN (no. 132-2000).

#### REFERENCES

1. H. Akbari, X. Altuna, S. Bardin, *et al.*, Phys. Lett. B **313**, 491 (1993).
2. C. T. Murphy, R. A. Carrigan, Jr., D. Chen, *et al.*, Nucl. Instrum. Methods Phys. Res. B **119**, 231 (1996).
3. A. G. Afonin, V. M. Biryukov, V. A. Gavrilushkin, *et al.*, Pis'ma Zh. Éksp. Teor. Fiz. **67**, 741 (1998) [JETP Lett. **67**, 781 (1998)].
4. A. A. Arkhipenko, A. G. Afonin, B. I. Baranov, *et al.*, Phys. Lett. B **435**, 240 (1998).
5. A. G. Afonin, V. M. Biryukov, V. A. Gavrilushkin, *et al.*, Pis'ma Zh. Éksp. Teor. Fiz. **68**, 544 (1998) [JETP Lett. **68**, 568 (1998)].
6. V. Biryukov, Nucl. Instrum. Methods Phys. Res. B **53**, 202 (1991).
7. A. M. Taratin, S. A. Vorobiev, M. D. Bavizhev, *et al.*, Nucl. Instrum. Methods Phys. Res. B **58**, 103 (1991).
8. A. G. Afonin, V. N. Gres, and V. I. Terekhov, in *Proceedings of European Particle Accelerator Conference, EPAC, Stockholm, 1998*.
9. V. Biryukov, Phys. Rev. E **51**, 3522 (1995).
10. M. Breese, Nucl. Instrum. Methods Phys. Res. B **132**, 540 (1997).
11. V. I. Kotov, A. G. Afonin, V. M. Biryukov, *et al.*, in *Proceedings of the European Particle Accelerator Conference, EPAC, Vienna, 2000*, p. 364.

*Translated by A. Isaakyan*

# $\hat{sl}(2) \oplus \hat{sl}(2)/\hat{sl}(2)$ Coset Theory Is a Hamiltonian Reduction of the $\hat{D}(2|1; \alpha)$ Superalgebra

**A. M. Semikhatov\*** and **B. L. Feigin\*\***

\**Tamm Theoretical Physics Department, Lebedev Institute of Physics, Russian Academy of Sciences,  
Leninskii pr. 53, Moscow, 117924 Russia*

\*\**Landau Institute for Theoretical Physics, Russian Academy of Sciences,  
ul. Kosygina 2, Moscow, 117334 Russia*

Received April 19, 2001; in final form, May 31, 2001

It is shown that  $\hat{sl}(2)_{k_1} \oplus \hat{sl}(2)_{k_2}/\hat{sl}(2)_{k_1+k_2}$  coset theory is a quantum Hamiltonian reduction of the exceptional affine Lie superalgebra  $\hat{D}(2|1; \alpha)$ . In addition, the  $W$  algebra of this theory is the commutant of the  $\mathcal{U}_q D(2|1; \alpha)$  quantum group. © 2001 MAIK “Nauka/Interperiodica”.

PACS numbers: 02.20.Uw; 11.25.Hf

In this paper, it is found that (i) the well-known  $\hat{sl}(2)_{k_1} \oplus \hat{sl}(2)_{k_2}/\hat{sl}(2)_{k_1+k_2}$  coset models and (ii) the exceptional affine Lie superalgebra  $\hat{D}(2|1; \alpha)$ , two structures in two-dimensional conformal field theories, are related to one another as follows:

$$\begin{aligned} & \text{Quantum Hamiltonian Reduction } [\hat{D}(2|1; \alpha)_\kappa] \\ & = \hat{sl}(2)_{k_1} \oplus \hat{sl}(2)_{k_2}/\hat{sl}(2)_{k_1+k_2} \end{aligned} \quad (1)$$

(at general parameter values). This result seems nontrivial in view of the popularity of the  $\hat{sl}(2) \oplus \hat{sl}(2)/\hat{sl}(2)$  coset models [which are analogous to the  $\hat{su}(2) \oplus \hat{su}(2)/\hat{su}(2)$  ones]—they have been extensively studied from various points of view, but the presence of the  $\hat{D}(2|1; \alpha)$  algebra in them has not been revealed so far. As to the  $\hat{D}(2|1; \alpha)$  algebra itself, it appeared in models of conformal field theory only in [1] (where its partial Hamiltonian reduction to the  $N = 4$  superconformal algebra was constructed) and, more recently, in [2] [in the construction of the vertex-operator extension of  $\hat{sl}(2)_k \oplus \hat{sl}(2)_k$ ]; this algebra, which is exceptional in the classification of Lie algebras [3], therefore remains quite an “exceptional” object in models of conformal field theory. It is even more interesting that, in the aforementioned coset theories, it is hidden. The reduction being considered is maximal (all currents that take values in the nilpotent subalgebra are constrained), whereas the nilpotent subalgebra corresponds to the case where all simple roots are chosen to be fermionic.

The equality in (1) requires describing the relation between the parameters on the left- and on the right-hand side. For this, we recall that the definition of a coset theory is invariant under permutations of the three levels  $k_1$ ,  $k_2$ , and  $k_3 = -k_1 - k_2 - 4$  and that the parameter  $\alpha$  is defined modulo a order-six group of discrete transformation; moreover, the level  $\kappa$  on the left-hand side of (1) can be chosen to be equal to the level of any of the three  $\hat{sl}(2)$  subalgebras in  $D(2|1; \alpha)$ , so that it is convenient to specify these three levels  $\kappa_1$ ,  $\kappa_2$ , and  $\kappa_3$ , which are related by the equation  $1/\kappa_1 + 1/\kappa_2 + 1/\kappa_3 = 0$ , instead of the parameter  $\alpha$  and the level  $\kappa$ . The relations  $\kappa_1 = 1/(k_1 + 2)$ ,  $\kappa_2 = 1/(k_2 + 2)$ , and  $\kappa_3 = -1/(k_1 + k_2 + 4)$  then hold; modulo the aforementioned arbitrariness, we also have  $\alpha = -1 - (k_1 + 2)/(k_2 + 2)$ .

In addition to (1), we will show that the algebra of local fields of the coset theory in question coincides with the  $W$  algebra  ${}^{\mathcal{W}}D(2|1; \alpha)$  defined by the root system of the  $D(2|1; \alpha)$  Lie superalgebra; that is,

$$\hat{sl}(2)_{k_1} \oplus \hat{sl}(2)_{k_2}/\hat{sl}(2)_{k_1+k_2} = {}^{\mathcal{W}}D(2|1; \alpha). \quad (2)$$

It is in order here to dwell at some length on the definition of the right-hand side. It is well known that, for a bosonic Lie algebra  $\mathfrak{g}$  (more precisely, for a root system), the  $W$  algebra  ${}^{\mathcal{W}}\mathfrak{g}$  is specified as the commutant of operators (referred to as screenings in this context) that realize the nilpotent subalgebra of the  $\mathcal{U}_q \mathfrak{g}$  quantum group. The screenings  $\sigma_i = \oint e^{\mathbf{a}_i \cdot \boldsymbol{\varphi}}$  are constructed in terms of free fields  $\boldsymbol{\varphi}$  by taking the simple-root vectors  $\boldsymbol{\alpha}_i$  and by replacing them by  $\mathbf{a}_i = \frac{1}{\kappa} \boldsymbol{\alpha}_i$  (the central

charge of the resulting  $W$  algebra depends on the parameter  $\kappa$  introduced here). For the Lie superalgebra  $\mathfrak{g}$  such that all its odd roots are isotropic [in particular, for  $D(2|1; \alpha)$ ], we define  ${}^{\mathcal{W}}\mathfrak{g}$  in a way similar to that in the bosonic case, the only distinction being that the operator corresponding to each odd root  $\alpha_i$  is replaced by  $\oint e^{\mathbf{a}_i \cdot \Phi}$ , where  $\mathbf{a}_i$  satisfy the condition  $\mathbf{a}_i \cdot \mathbf{a}_i = 1$  and where the set of all screenings satisfies the nilpotent subalgebra in  ${}^{\mathcal{U}}\mathfrak{g}$ . Operators of the form  $\oint e^{\mathbf{a}_i \cdot \Phi}$ , where  $\mathbf{a}_i \cdot \mathbf{a}_i = 1$ , will be referred to as fermionic screenings, while all the remaining ones are called bosonic screenings.

Described below are basic steps leading to (1) and (2).

**1. Reminder:  $D(2|1; \alpha)$  superalgebra [3].** The  $D(2|1; \alpha)$  superalgebra of dimension (9|8) has the even part  $sl(2) \oplus sl(2) \oplus sl(2)$ , whose action on the odd part is the product of two-dimensional representations. This algebra admits a set of roots where all three simple roots are fermionic; the Chevalley generators  $\psi_i$ ,  $i = 1, 2, 3$ , satisfy the relations  $[\psi_1, \psi_1] = 0$ ,  $[\psi_2, \psi_2] = 0$ ,  $[\psi_3, \psi_3] = 0$  (here,  $[\ , \ ]$  stands for a supercommutator), and  $[\psi_2, [\psi_1, \psi_2]] + (\alpha + 1)[\psi_3, [\psi_1, \psi_2]] = 0$ . Therefore, the nilpotent subalgebra also contains three even elements

$$e^{(1)} = \frac{\kappa_1}{2}[\psi_2, \psi_3], \quad e^{(2)} = \frac{\kappa_2}{2}[\psi_1, \psi_3],$$

$$e^{(3)} = \frac{\kappa_3}{2}[\psi_1, \psi_2],$$

which are upper-triangle generators of three  $sl(2)$  subalgebras, and, in addition, one odd element  $\psi_0 = [\psi_1, e^{(1)}] = [\psi_2, e^{(2)}] = [\psi_3, e^{(3)}]$ . Here,  $1/\kappa_1 + 1/\kappa_2 + 1/\kappa_3 = 0$ , while the parameter  $\alpha$  is then defined as  $\alpha = -1 - (\kappa_3/\kappa_2)$ .

**2. Hamiltonian reduction of  $\hat{D}(2|1; \alpha)$ .** The Hamiltonian reduction of superalgebras may require introducing auxiliary fields used in imposing constraints. For the  $\hat{D}(2|1; \alpha)$  algebra, there are a few natural options of such fields and constraints. The scheme that we consider is asymmetric in three fermionic roots—namely, we introduce a free fermionic system generated by  $\eta$  and  $\xi$  and characterized by the operator product  $\eta(z)\xi(w) = 1/(z-w)$  and impose the constraints  $\psi_1(z) = \eta(z)$ ,  $\psi_2(z) = \eta(z)$ , and  $\psi_3(z) = \xi(z)$  and, accordingly,  $e^{(1)}(z) = -\kappa_1/2$ ,  $e^{(2)}(z) = -\kappa_2/2$ ,  $e^{(3)}(z) = 0$ , and  $\psi_0(z) = 0$ . In order to construct the relevant Becchi–Rouet–Stora–Tyutin (BRST) differential, we introduce ghosts—that is, first-order bosonic and fermionic systems featuring the relevant operator products  $\beta_i(z)\gamma_j(w) = -\delta_{ij}/(z-w)$  and  $B_i(z)C_j(w) = \delta_{ij}/(z-w)$ . The

BRST differential is then given by  $\mathcal{Q} = \oint (\mathcal{T}^{(0)} + \mathcal{T}^{(1)} + \mathcal{T}^{(2)})$ , where

$$\mathcal{T}^{(0)} = \psi_1\gamma_1 + \psi_2\gamma_2 + \psi_3\gamma_3 + e^{(1)}C_1 + e^{(2)}C_2$$

$$+ e^{(3)}C_3 + \psi_0\gamma_0 - \frac{2}{\kappa_1}B_1\gamma_2\gamma_3 - \frac{2}{\kappa_2}B_2\gamma_3\gamma_1$$

$$- \frac{2}{\kappa_3}B_3\gamma_1\gamma_2 - \beta_0\gamma_1C_1 - \beta_0\gamma_2C_2 - \beta_0\gamma_3C_3,$$

$$\mathcal{T}^{(1)} = -\gamma_1\eta - \gamma_2\eta - \gamma_3\xi,$$

$$\mathcal{T}^{(2)} = \frac{\kappa_1}{2}C_1 + \frac{\kappa_2}{2}C_2.$$

The cohomology of this BRST operator is the result of the Hamiltonian reduction in question. More precisely, the cohomology of  $\mathcal{Q}$  inevitably contains the Heisenberg algebra, since we have introduced the auxiliary fields  $\eta$  and  $\xi$ —our objective is to find, in a cohomology with zero ghost number, a  $W$  algebra that commutes with this Heisenberg algebra  $\mathcal{H}_0$ . One can easily find a current that generates the  $\mathcal{H}_0$  algebra. The result is

$$\tilde{H} = 2h^{(3)} + 2B_3C_3 + \beta_0\gamma_0 + \beta_1\gamma_1 + \beta_2\gamma_2 - \beta_3\gamma_3 + \eta\xi,$$

where  $h^{(i)}$  are the Cartan currents of three  $\hat{sl}(2)$  subalgebras in  $\hat{D}(2|1; \alpha)$ . We further note that the cohomology of  $\mathcal{Q}$  also contain the family of stress–energy tensors that depends on the parameter  $j$  and which has the form

$$\tilde{T}_{(j)} = \mathcal{T} + \partial B_1C_1 + \partial B_2C_2 + (2j-3)B_3\partial C_3$$

$$+ 2(j-1)\partial B_3C_3 + (j-1)\beta_0\partial\gamma_0 + j\partial\beta_0\gamma_0$$

$$+ (j-2)\beta_1\partial\gamma_1 + (j-1)\partial\beta_1\gamma_1 + (j-2)\beta_2\partial\gamma_2$$

$$+ (j-1)\partial\beta_2\gamma_2 + (1-j)\beta_3\partial\gamma_3 + (2-j)\partial\beta_3\gamma_3$$

$$+ (j-2)\eta\partial\xi + (j-1)\partial\eta\xi + \partial h^{(1)}$$

$$+ \partial h^{(2)} + 2(j-1)\partial h^{(3)}.$$

The only combination that commutes with  $\tilde{H}$  and which is independent of  $j$  is given by

$$\hat{T} = \tilde{T}_{(j)} - \frac{1}{2(1+2\kappa_3)}\tilde{H}\tilde{H} - \frac{4(j-1)\kappa_3 + 2j-3}{2(1+2\kappa_3)}\partial\tilde{H}. \quad (5)$$

The central charge of this stress–energy tensor can be represented as

$$\hat{c} = \frac{3(1-2\kappa_1)(1-2\kappa_2)}{1+2\kappa_3}. \quad (6)$$

If the parameters are identified as  $1/\kappa_1 = k_1 + 2$ ,  $1/\kappa_2 = k_2 + 2$ , and  $1/\kappa_3 = -k_1 - k_2 - 4$ , it coincides with the central charge of  $\hat{sl}(2)_{k_1} \oplus \hat{sl}(2)_{k_2}/\hat{sl}(2)_{k_1+k_2}$  coset theory.

In order to demonstrate that, in addition to the Virasoro algebra generated by the operator  $\hat{T}$ , the cohomology of  $\mathcal{Q}$  contain a  $W$  algebra that commutes with  $\mathcal{H}_0$ , we note that the decomposition  $\mathcal{Q} = \mathcal{Q}^{(0)} + \mathcal{Q}^{(1)} + \mathcal{Q}^{(2)}$ , which follows from Eqs. (3) and (4), corresponds to that filtration on the BRST complex with respect to which  $\mathcal{Q}^{(i)}$  lowers the index by  $i$ , so that we have  $(\mathcal{Q}^{(0)})^2 = 0$ ,  $\mathcal{Q}^{(0)}\mathcal{Q}^{(1)} + \mathcal{Q}^{(1)}\mathcal{Q}^{(0)} = 0$ , and  $(\mathcal{Q}^{(1)})^2 + \mathcal{Q}^{(0)}\mathcal{Q}^{(2)} + \mathcal{Q}^{(2)}\mathcal{Q}^{(0)} = 0$ . This makes it possible to use the relevant spectral sequence. The cohomology of  $\mathcal{Q}^{(0)}$  in zero ghost number are generated by  $\eta\xi$  and by three other currents:

$$\hat{h}^{(i)} = h^{(i)} + B_i C_i + \frac{1}{2} \sum_{j=0}^3 (-1)^{\delta_{i,j}} \beta_j \gamma_j, \quad i = 1, 2, 3.$$

A key observation is that terms appearing in  $\mathcal{Q}^{(1)}$  act on the cohomology of  $\mathcal{Q}^{(0)}$  as vertex operators; that is,

$$\begin{aligned} & \gamma_1 \eta \\ = & \exp \left\{ \int \left( \frac{1}{\kappa_1} \hat{h}^{(1)} - \frac{1}{\kappa_2} \hat{h}^{(2)} - \left( \frac{1}{\kappa_3} + 2 \right) \hat{h}^{(3)} + \tilde{H} \right) \right\}, \\ & \gamma_2 \eta \\ = & \exp \left\{ \int \left( -\frac{1}{\kappa_1} \hat{h}^{(1)} + \frac{1}{\kappa_2} \hat{h}^{(2)} - \left( \frac{1}{\kappa_3} + 2 \right) \hat{h}^{(3)} + \tilde{H} \right) \right\}, \\ & \gamma_3 \xi \\ = & \exp \left\{ \int \left( -\frac{1}{\kappa_1} \hat{h}^{(1)} - \frac{1}{\kappa_2} \hat{h}^{(2)} + \left( \frac{1}{\kappa_3} + 2 \right) \hat{h}^{(3)} - \tilde{H} \right) \right\}. \end{aligned}$$

Denoting by  $X_a$ ,  $a = 1, 2, 3$ , the exponents appearing in these formulas, we find the operator products  $X_1(z)X_2(w) = (1/\kappa_3 + 1)\log(z-w)$ ,  $X_1(z)X_3(w) = (1/\kappa_2 - 1)\log(z-w)$ , and  $X_2(z)X_3(w) = (1/\kappa_1 - 1)\log(z-w)$ . Defining the scalar product in the space of currents as the coefficient of the logarithm, we obtain  $\langle X_1, X_2 \rangle + \langle X_1, X_3 \rangle + \langle X_2, X_3 \rangle = -1$ . In addition, it can easily be shown that  $\langle X_a, X_a \rangle = 1 \forall a = 1, 2, 3$ .

Thus, we see that, in the three-boson space representing that part of zero term in the spectral sequence which is complementary to  $\tilde{H}$ , three operators  $\oint \gamma_1 \eta$ ,  $\oint \gamma_2 \eta$ , and  $\oint \gamma_3 \xi$  determine a  $W$  algebra as their commutant. This  $W$  algebra contains the Virasoro algebra generated by the operator in (5) with the central charge (6). Following [4], we can show that, at general values

of the parameters, it is precisely this  $W$  algebra multiplied by  $\mathcal{H}_0$  that is the cohomology of  $\mathcal{Q}$  (in particular, the differential of  $\mathcal{Q}^{(2)}$  is trivial on the first term of the spectral sequence). Thereby, the result of the Hamiltonian reduction is a  $W$  algebra specified as the commutant of three fermionic screenings.

### 3. $\mathcal{WD}(2|1; \alpha)$ , screenings, and quantum groups.

In order to study this commutant, what was obtained above will now be formulated in a more invariant form. There have arisen operators that are expressed in terms of three free fields  $\boldsymbol{\varphi} = \{\varphi_1, \varphi_2, \varphi_3\}$  as  $\sigma_i = \oint e^{\mathbf{a}_i \cdot \boldsymbol{\varphi}}$ , where the vectors  $\mathbf{a}_i$  satisfy the conditions  $\mathbf{a}_i \cdot \mathbf{a}_i = 1$  and  $\mathbf{a}_1 \cdot \mathbf{a}_2 + \mathbf{a}_1 \cdot \mathbf{a}_3 + \mathbf{a}_2 \cdot \mathbf{a}_3 = -1$ . These three fermionic screenings generate the nilpotent subalgebra of the  $\mathcal{U}_q D(2|1; \alpha)$  quantum group. By definition, their commutant is the  $W$  algebra  $\mathcal{WD}(2|1; \alpha)$ . It depends on two parameters  $k_1$  and  $k_2$  that can be specified by setting

$$\begin{aligned} \mathbf{a}_1 \cdot \mathbf{a}_2 &= k_2 + 1, & \mathbf{a}_1 \cdot \mathbf{a}_3 &= k_1 + 1, \\ \mathbf{a}_2 \cdot \mathbf{a}_3 &= -3 - k_1 - k_2. \end{aligned}$$

The central charge of the  $W$  algebra is then equal to the central charge of the coset on the right-hand side of (1). Along with  $\mathcal{WD}(2|1; \alpha)$ , we will therefore use the notation  $\mathcal{WD}_{2|1}(k_1, k_2)$ .

Further, each pair of fermionic screenings  $\{\sigma_i, \sigma_j\}$ ,  $i \neq j$ , determines the nilpotent subalgebra in the  $\mathcal{U}_q sl(2|1)$  quantum group. Thereby, the commutant of these two screenings in the relevant two-boson subspace is the  $W$  algebra  $\mathcal{W}sl(2|1)$ . But this algebra commutes with the third, bosonic, screening, which has the form of the product of a current and an exponential. Since the algebra  $\mathcal{WD}(2|1; \alpha)$  is the intersection of three algebras of the form  $\mathcal{W}sl(2|1) \otimes$  (Heisenberg), its commutant involves three bosonic screening ( $1 \leq i < j \leq 3$ ); that is,

$$\rho_{ij} = \oint R_{ij}, \quad R_{ij} = J_{ij} e^{\mathbf{r}_{ij} \cdot \boldsymbol{\varphi}}, \quad \mathbf{r}_{ij} = \frac{\mathbf{a}_i + \mathbf{a}_j}{(\mathbf{a}_i \cdot \mathbf{a}_j) + 1},$$

where  $J_{ij}$  is a linear combination of  $\mathbf{a}_i \cdot \partial \boldsymbol{\varphi}$  and  $\mathbf{a}_j \cdot \partial \boldsymbol{\varphi}$ . From the conditions imposed on  $\mathbf{a}_i$  it follows that each two operators from the set  $\rho_{12}$ ,  $\rho_{13}$ , and  $\rho_{23}$  commute and that each operator  $\rho_{ij}$  commutes with  $\sigma_1$ ,  $\sigma_2$ , and  $\sigma_3$ .

The operators  $\rho_{12}$ ,  $\rho_{13}$ , and  $\rho_{23}$  are upper-triangle generators in the  $\mathcal{U}_{q_a} sl(2)$  quantum groups ( $a = 1, 2, 3$ )

with relevant quantum-group parameters  $q_a = e^{\pi i \kappa_a}$ , where

$$\kappa_1 = \frac{2}{k_2 + 2}, \quad \kappa_2 = \frac{2}{k_1 + 2}, \quad \kappa_3 = \frac{-2}{k_1 + k_2 + 2}.$$

Thus, the  $W$  algebra  $\mathcal{WD}(2|1; \alpha)$  commutes with two mutually commuting quantum groups  $\mathcal{U}_q D(2|1; \alpha)$  and  $\mathcal{U}_{q_1} sl(2) \otimes \mathcal{U}_{q_2} sl(2) \otimes \mathcal{U}_{q_3} sl(2)$ . Of these, the second

is used to prove that  ${}^{\mathcal{W}}D_{2|1}(k_1, k_2)$  is the  $W$  algebra of the relevant coset theory.

**4.  ${}^{\mathcal{W}}D_{2|1}(k_1, k_2)$  is the algebra of a coset theory.**

We recall that the conformal theory specified by  $\hat{sl}(2) \oplus \hat{sl}(2)/\hat{sl}(2)$  coset [8] can be defined within the BRST approach [9–11] as the relative semi-infinite cohomology

$$H^{\infty/2}(\hat{sl}(2)_{-4}, sl(2); \underset{(k_1)}{\text{Vac}} \otimes \underset{(k_2)}{\text{Vac}} \otimes \underset{(k_3)}{\text{Vac}})$$

of the complex

$$\hat{sl}(2)_{k_1} \oplus \hat{sl}(2)_{k_2} \oplus \hat{sl}(2)_{k_3} \oplus (\text{ghosts})$$

$$\text{at } k_1 + k_2 + k_3 = -4,$$

where the ghosts are given by three systems of free fermions, while the differential is constructed in a standard way for the diagonally embedded  $\hat{sl}(2)$  algebra of level  $(-4)$  [5–7]. At general values of  $k_1$  and  $k_2$ , the cohomology of this complex are concentrated in zero ghost number, and this gives local fields (descendants of the vacuum) of the coset theory being considered.

The algebra of the coset vertex operators contains

$\bigoplus_{m,n,l} H^{\infty/2}(\hat{sl}(2), sl(2); \mathcal{M}_m \otimes \mathcal{M}_n \otimes \mathcal{M}_l)$ , where  $\mathcal{M}_l$  are Weyl modules. This makes it possible to characterize the coset by the following property: for any  $i = 1, 2, 3$ , the product of the coset and the  $\hat{sl}(2)$  algebra of level  $-k_i - 4$  dual to  $k_i$  admits a vertex-operator extension (v.-o. e.) to the product of the other two  $\hat{sl}(2)_{k_i}$  algebras; for example,

$$\begin{aligned} & {}^{\mathcal{W}}D_{2|1}(k_1, k_2) \otimes \mathcal{U}\hat{sl}(2)_{-k_1-4} \\ & \xrightarrow{\text{v.-o.e.}} \mathcal{U}\hat{sl}(2)_{k_2} \otimes \mathcal{U}\hat{sl}(2)_{k_3} \end{aligned} \quad (7)$$

where, by  $\mathcal{U}$ , one can mean the vacuum representation. This vertex-operator extension is constructed by contracting the coset vertex operators and the  $\hat{sl}(2)_{-k_1-4}$  vertex operators with respect to the quantum-group index, the contraction in question being induced by taking the monodromy-free elements in each term:

$$\begin{aligned} & \bigoplus_{n \geq 0} H^{\infty/2}(\hat{sl}(2), sl(2); \mathcal{M}_n \otimes \underset{(k_2)}{\text{Vac}} \otimes \underset{(k_3)}{\text{Vac}}) \otimes \mathcal{M}_n \\ & \xrightarrow{\sim} \underset{(k_2)}{\text{Vac}} \otimes \underset{(k_3)}{\text{Vac}}. \end{aligned}$$

The property in (7) characterizes  ${}^{\mathcal{W}}D_{2|1}(k_1, k_2)$  as a coset, since  $\hat{sl}(2)_{-k_1-4}$  is then diagonally embedded in  $\hat{sl}(2)_{k_2} \oplus \hat{sl}(2)_{k_3}$ , where  $k_1 + k_2 + k_3 = -4$ ; hence,

$\hat{sl}(2)_{-4}$  is diagonally embedded in the right-hand side of the vertex-operator extension

$$\begin{aligned} & {}^{\mathcal{W}}D_{2|1}(k_1, k_2) \otimes \mathcal{U}\hat{sl}(2)_{-k_1-4} \otimes \mathcal{U}\hat{sl}(2)_{k_1} \\ & \longrightarrow \mathcal{U}\hat{sl}(2)_{k_1} \otimes \mathcal{U}\hat{sl}(2)_{k_2} \otimes \mathcal{U}\hat{sl}(2)_{k_3}. \end{aligned}$$

In accordance with the definition, the relative semi-infinite cohomology of the right-hand side then reproduce the coset; on the left-hand side,  $H^{\infty/2}(\hat{sl}(2)_{-4}, sl(2))$  is calculated as  $\mathbb{C}$  on  $\mathcal{U}\hat{sl}(2)_{-k_1-4} \otimes \mathcal{U}\hat{sl}(2)_{k_1}$ , whereby one obtains  ${}^{\mathcal{W}}D_{2|1}(k_1, k_2)$ .

Replacing  $k_1$  by  $k_3 = -k_1 - k_2 - 4$ , we thus construct the required vertex-operator extension:

$$\begin{aligned} & {}^{\mathcal{W}}D_{2|1}(k_1, k_2) \otimes \mathcal{U}sl(2)_{k_1+k_2} \\ & \xrightarrow{\text{v.-o.e.}} \mathcal{U}\hat{sl}(2)_{k_1} \otimes \mathcal{U}\hat{sl}(2)_{k_2}. \end{aligned} \quad (8)$$

Let  $\mathbb{C}_{\kappa}^n$  be an  $n$ -dimensional module over the  $\mathcal{U}_q sl(2)$  quantum group, where  $q = e^{\pi i \kappa}$ . The operators

$$\begin{aligned} \Psi_{212} &= e^{-\frac{1}{2}(\mathbf{r}_{12} + \mathbf{r}_{23}) \cdot \boldsymbol{\varphi}}, & \Psi_{122} &= e^{-\frac{1}{2}(\mathbf{r}_{13} + \mathbf{r}_{23}) \cdot \boldsymbol{\varphi}}, \\ \Upsilon_{113} &= \mathbf{a}_1 \cdot \partial \boldsymbol{\varphi} e^{-\mathbf{r}_{23} \cdot \boldsymbol{\varphi}} \end{aligned}$$

are the highest weight vectors in the representations of the  $\mathcal{U}_{q_1} sl(2) \otimes \mathcal{U}_{q_2} sl(2) \otimes \mathcal{U}_{q_3} sl(2)$  quantum group, the dimensions of these representations being indicated by the indices [these are singlets with respect to the  $\mathcal{U}_q D(2|1; \alpha)$ ]. We express this as follows:

$$\begin{aligned} \Psi_{212}(z) &\in \left( \mathbb{C}^2_{\frac{2}{k_2+2}} \otimes \mathbb{C}^2_{\frac{2}{k_1+k_2+2}} \right)(z), \\ \Psi_{122}(z) &\in \left( \mathbb{C}^2_{\frac{2}{k_1+2}} \otimes \mathbb{C}^2_{\frac{2}{k_1+k_2+2}} \right)(z), \\ \Upsilon_{113}(z) &\in \mathbb{C}^3_{\frac{2}{k_1+k_2+2}}(z). \end{aligned}$$

The operator  $\Upsilon_{113}$ , which is a three-dimensional representation of  $\mathcal{U}_{q^{-1}} sl(2)$  at  $q = e^{2\pi i/(k_1+k_2+2)}$ , can be contracted with the spin-1 vertex operator  $\Phi_1(k_1+k_2)$  for the  $\hat{sl}(2)_{k_1+k_2}$  algebra. This vertex operator is a three-dimensional representation of  $\mathcal{U}_{q^{-1}} sl(2)$ . We represent this fact as  $\Phi_1(k_1+k_2)(z) = \mathbb{C}^3(z) \otimes \mathbb{C}_q^3$ , where the first factor  $\mathbb{C}^3$  is a triplet with respect to the horizontal  $sl(2)$  subalgebra. The contraction in the quantum-group index is given by taking the quantum-group singlet  $w_3 \in \mathbb{C}_q^3 \otimes \mathbb{C}_{q^{-1}}^3$ . The result is then a local field,

$$\underbrace{\mathbb{C}^3(z) \otimes \mathbb{C}^2_{\frac{2}{k_1+k_2+2}}}_{\Phi_1(k_1+k_2)(z)} \otimes \underbrace{\mathbb{C}^3_{\frac{-2}{k_1+k_2+2}}(z)}_{\Upsilon_{113}(z)} \ni \mathbb{C}^3(z) \otimes w_3,$$

that is a three-dimensional representation of the  $sl(2)$  subalgebra in  $\hat{sl}(2)_{k_1+k_2}$ . In this representation, we choose the basis  $J_*^+(z)$ ,  $J_{\text{diag}}^0(z)$ , and  $J_*^-(z)$ , where  $J_*^+(z)$  corresponds to the highest weight vector. Suppose that  $J_{\text{diag}}^{\pm,0}(z)$  are currents of the  $\hat{sl}(2)_{k_1+k_2}$  algebra. The currents

$$J_1^{\pm,0} = \frac{1}{k_1+k_2}(k_1 J_{\text{diag}}^{\pm,0} + J_*^{\pm,0}),$$

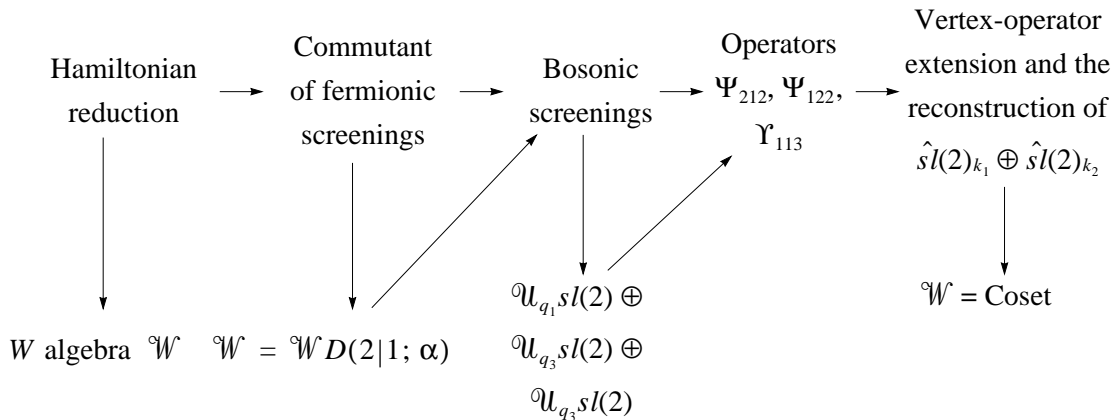
$$J_2^{\pm,0} = \frac{1}{k_1+k_2}(k_1 J_{\text{diag}}^{\pm,0} - J_*^{\pm,0})$$

then satisfy the relevant  $\hat{sl}(2)_{k_i}$  algebra. [Here, the space generated by the currents  $J_*^{\pm,0}$  is identified with that representation of  $\hat{sl}(2)_{k_1+k_2}$  which is generated by

$$\underbrace{\mathbb{C}^2(z) \otimes \mathbb{C}^2_{\frac{2}{k_1+k_2+2}}}_{\Phi_{1/2}(k_1+k_2)(z)} \otimes \underbrace{\mathbb{C}^2_{\frac{2}{k_2+2}}(z) \otimes \mathbb{C}^2_{\frac{-2}{k_1+k_2+2}}}_{\Psi_{212}(z)} \ni \mathbb{C}^2(z) \otimes \mathbb{C}^2_{\frac{2}{k_2+2}} \otimes w_2,$$

where  $w_2$  is a monodromy-free element and  $\mathbb{C}^2(z) \otimes \mathbb{C}^2_q$  is the spin-1/2 vertex operator  $\Phi_{1/2}(k_2)(z)$  for  $\hat{sl}(2)_{k_2}$ . For  $\hat{sl}(2)_{k_1}$ , a similar construction is valid, but use is made of  $\Psi_{122}$  in that case.

In conclusion, we schematically summarize basic steps in the proof of the statements in (1) and (2):



We also note that, since a partial Hamiltonian reduction of the  $\hat{D}(2|1; \alpha)$  algebra leads to the (nonlinear)  $N = 4$  superconformal algebra [1], there arises the interesting question of the relation of this algebra to the coset via a secondary Hamiltonian reduction [12].

the currents  $k_2 J_1^{\pm,0}(z) - k_1 J_2^{\pm,0}(z)$  in  $\hat{sl}(2)_{k_1} \oplus \hat{sl}(2)_{k_2}$ . Thus, the extension in (8) has been derived, whence it follows that there is the homomorphism

$$\mathcal{W}D_{2|1}(k_1, k_2) \rightarrow H^{\infty/2}(\hat{sl}(2)_{-4}, sl(2); \text{Vac}_{(k_1)} \otimes \text{Vac}_{(k_2)} \otimes \text{Vac}_{(k_3)}),$$

which is in fact an isomorphism.

The vertex operators for  $\hat{sl}(2)_{k_1} \oplus \hat{sl}(2)_{k_2}$  can be constructed in a similar way. Let  $\Phi_{1/2}(k)(z) = \mathbb{C}^2(z) \otimes \mathbb{C}^2_{2/(k+2)}$  be the spin-1/2 vertex operator for  $\hat{sl}(2)_k$ . Here,  $\mathbb{C}^2_{2/(k+2)}$  is a two-dimensional representation of  $\mathcal{U}_q sl(2)$  with quantum-group parameter  $q = e^{2\pi i/(k+2)}$ , while the first factor  $\mathbb{C}^2$  is an  $sl(2)$  doublet. By using the duality of quantum-group representations on  $\Phi_{1/2}(k_1+k_2)$  and  $\Psi_{212}$ , we arrive at

We are indebted to A. Taormina for enlightening comments on  $N = 4$  algebras and for information about the studies devoted to the reduction  $\hat{D}(2|1; \alpha) \rightarrow (N = 4)$ . We gratefully acknowledge the hospitality extended to us at the Fields Institute, where part of this study was performed.

This work was supported in part by the Russian Foundation for Basic Research (project no. 01-01-00906) and by the Foundation for the Promotion of Russian Science.

#### REFERENCES

1. K. Ito and J. O. Madsen, *Phys. Lett. B* **283**, 223 (1992); K. Ito, J. O. Madsen, and J. L. Petersen, *Nucl. Phys. B* **398**, 425 (1993); *Phys. Lett. B* **292**, 298 (1992).
2. P. Bowcock, B. L. Feigin, A. M. Semikhatov, and A. Taormina, *Commun. Math. Phys.* **214**, 495 (2000).
3. V. G. Kač, *Commun. Math. Phys.* **53**, 31 (1977); J. F. Cornwell, *Group Theory in Physics* (Academic, New York, 1989), Vol. 3.
4. B. Feigin and E. Frenkel, *Int. J. Math. Phys. A* **7** (Supplement 1A), 197 (1992).
5. B. L. Feigin, *Usp. Mat. Nauk* **39** (2), 195 (1984).
6. I. Frenkel, H. Garland, and G. J. Zuckerman, *Proc. Natl. Acad. Sci. USA* **83**, 8446 (1986).
7. S. Hwang, *Commun. Math. Phys.* **194**, 591 (1998).
8. P. Goddard, A. Kent, and D. Olive, *Phys. Lett. B* **152B**, 88 (1985).
9. K. Gawędzki and A. Kupiainen, *Phys. Lett. B* **215**, 119 (1988); *Nucl. Phys. B* **320**, 625 (1989).
10. D. Karabali and H. Schnitzer, *Nucl. Phys. B* **329**, 649 (1990).
11. S. Hwang and H. Rhedin, *Nucl. Phys. B* **406**, 165 (1993).
12. J. O. Madsen and E. Ragoucy, *Commun. Math. Phys.* **185**, 509 (1997).

*Translated by A. Isaakyan*

# Beam Focusing upon the Reflection from Crystals and Multilayer Periodic Structures with Variable Period

A. V. Andreev

Moscow State University, Vorob'evy gory, Moscow, 119899 Russia

e-mail: andreev@sr1.phys.msu.su

Received June 6, 2001

The focusing properties of crystals and multilayer structures with variable period are demonstrated for the symmetric and asymmetrical Bragg reflection geometries. The focusing efficiency is examined. © 2001 MAIK "Nauka/Interperiodica".

PACS numbers: 41.50.+h

**1.** The considerable progress achieved in recent years in X-ray microscopy is associated with the development of new X-ray-optical focusing elements such as Bragg–Fresnel and hollow spherical lenses, Fresnel zone plates, and kinoform structures, etc. [1–2]. Capillary focusing systems are successfully utilized in X-ray microdiagnostics.

Recently [4], we have suggested an X-ray microscope that is based on the use of schemes with highly asymmetrical X-ray diffraction in crystals. Our experiments demonstrated the possibility of obtaining 50- to 100-fold enlarged images of objects with sizes of several tens of microns. The main reason hampering the extension of this scheme to the submicron range is that the image undergoes diffraction spreading on the way from the object to the reflecting crystal. Indeed, when using a radiation with the wavelength  $\lambda = 1 \text{ \AA}$ , the diffraction length for an object of size  $d = 1 \text{ }\mu\text{m}$  is  $l_d = d^2/\lambda = 1 \text{ cm}$ , leading to substantial restrictions in practical use of this method in X-ray microscopy schemes.

In this work, a new method of focusing X-ray beams is proposed, which is based on the use of crystals or single-domain periodic structures (multilayer X-ray mirrors, photonic crystals, etc.) with variable period. Calculations show that the enlargement for an object can be achieved with submicron resolution. The method is based on the use of strong spatial dispersion at the edges of the Bragg reflection region. In crystals with variable period, the width of this region depends on the deformation profile. This opens up wide possibilities of controlling the dispersion properties of such crystals and allows the fabrication of focusing optical systems. The use of a spatiotemporal analogy allows this principle to be naturally extended to the compression of phase-modulated pulses. Recently, we have demonstrated that femtosecond laser pulses can be compressed in one-dimensional photonic crystals [5].

**2.** To calculate the reflectivity of a crystal or multilayer structure with weakly varying period (in our case,  $\Delta d/d \leq 10^{-2}$ ), one can use the well-known system of equations for the dynamical two-beam diffraction in a crystal with one-dimensional deformation profile  $\mathbf{u}(z)$  [6]

$$\begin{aligned} \frac{dE_0}{dz} &= -\frac{i\kappa}{2\gamma_0}(\chi_0 E_0 + \chi_{\bar{h}} E_f), \\ \frac{dE_h}{dz} &= \frac{i\kappa}{2\gamma_h} \left[ \left( \chi_0 - \alpha - i\mathbf{H} \frac{d\mathbf{u}}{dz} \right) E_h + \chi_h E_0 \right], \end{aligned} \quad (1)$$

where  $E_{0,h}$  are the amplitudes of the incident and the diffracted waves in the crystal, respectively;  $\gamma_{0,h} = \sin\theta_{0,h}$ ;  $\theta_{0,h}$  are the angles between, respectively, the wave vector of the incident  $\mathbf{\kappa}_0$  and the diffracted  $\mathbf{\kappa}_h = \mathbf{\kappa}_0 + \mathbf{H}_h$  wave and the entrance face of the crystal;  $\mathbf{H}_h$  is the reciprocal lattice vector;  $\chi_{0,h}$  are the Fourier components of the crystal polarizability; and  $\alpha(\theta_0) = (\kappa^2 - \kappa_h^2)/\kappa^2 = 4\sin\theta_B[\sin(\theta_0 + \psi) - \sin\theta_B]$  is the detuning parameter determining the deflection of the angle of incidence  $\theta_0$  from the Bragg diffraction angle  $\theta_{0B} = \theta_B - \psi$ , where  $\sin\theta_B = H/2\kappa$  and the angle  $\psi$  stands for the slope of reflecting planes with respect to the entrance face of the crystal.

Let the exponential deformation profile  $\mathbf{u}(z) = \mathbf{u}_0 \exp(-z/l)$  be formed in a medium. In this case, the reflectivity amplitude is given by the expression

$$\begin{aligned} r(\theta_0) &= \sqrt{\frac{\gamma_h}{\gamma_0}} \left| \frac{E_h}{E_0} \right| \\ &= -\frac{4\chi_0}{\kappa l} \sqrt{\frac{\gamma_0 \gamma_h}{\chi_{\bar{h}} \chi_h}} \left[ a + \frac{ay \cdot {}_1F_1(1+a, 1+b, y)}{b \cdot {}_1F_1(a, b, y)} \right], \end{aligned} \quad (2)$$

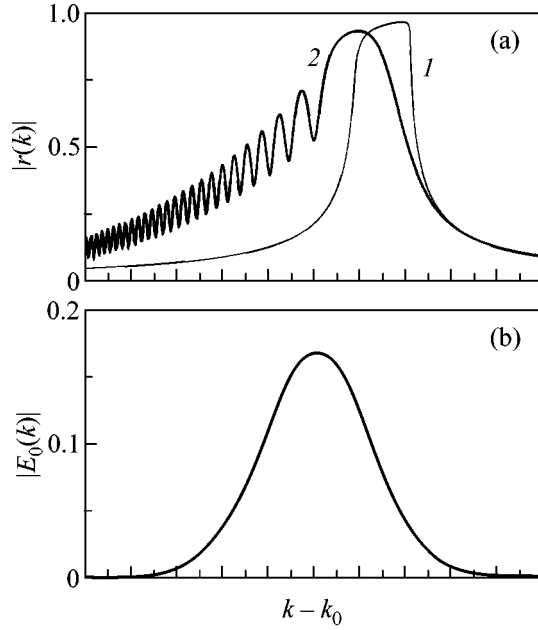


**Fig. 1.** (a) Angular profiles of reflectivity amplitude for the (curve 1) ideal and (curve 2) strained crystals and (b) angular profile of a beam incident on the crystal.

where  ${}_1F_1(a, b, y)$  is the hypergeometric function of parameters

$$a = -i\frac{\kappa l}{4} \left[ \left( \frac{1}{\gamma_0} + \frac{1}{\gamma_h} \right) \chi_0 + \frac{\alpha}{\gamma_h} - \beta \right. \\ \left. - \sqrt{\left( \left( \frac{1}{\gamma_0} + \frac{1}{\gamma_h} \right) \chi_0 + \frac{\alpha}{\gamma_h} - \beta \right)^2 - \frac{4\chi_{\bar{h}}\chi_h}{\gamma_0\gamma_h}} \right], \quad (3)$$

$$b = 1 + i\frac{\kappa l}{2} \sqrt{\left( \left( \frac{1}{\gamma_0} + \frac{1}{\gamma_h} \right) \chi_0 + \frac{\alpha}{\gamma_h} - \beta \right)^2 - \frac{4\chi_{\bar{h}}\chi_h}{\gamma_0\gamma_h}},$$

$$y = i2\kappa u_0 \sin\theta_B \cos\psi = i\beta.$$

Since the actual crystal boundary coincides with the  $z = u_0$  plane, it is convenient to introduce the coordinate  $z' = z - u_0$ . In this case, the displacement vector is determined by the expression  $\mathbf{u}(z') = \mathbf{u}_0 \exp(-z'/l) - \mathbf{u}_0$ . Figure 1a compares the reflectivity amplitude profiles for the  $\text{CuK}_\alpha$  radiation symmetrically reflected from the (111) planes of an ideal (curve 1) and strained (curve 2) germanium crystal with an exponential deformation profile for  $l = 17 \mu\text{m}$  and  $\Delta d/d = 3 \times 10^{-3}$ . Figure 1b shows the angular profile of an incident Gaussian beam formed by a  $0.5\text{-}\mu\text{m}$ -wide slit placed at a distance of 4 cm from the reflection region. This profile will be used below in the calculation of focusing efficiency in the symmetric case. One can see that the angular width of the incident beam exceeds the angular width of the reflection region for the ideal crystal and is comparable with the reflection width for the strained crystal.

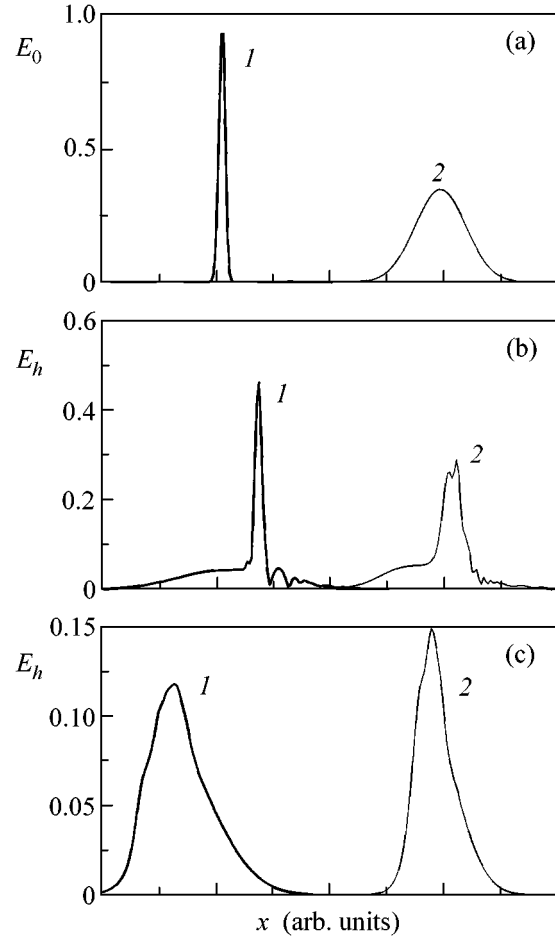


**Fig. 2.** Spatial profiles of (a) incident and (b, c) reflected beams. Curves 1 are for the  $z = h$  plane and curves 2 are for the  $z = 0$  plane.

**3.** Let us consider the reflection from a semi-infinite crystal with the deformation profile indicated above. Let the crystal occupy the  $z \leq 0$  region. If the spatial profile of incident beam has the form  $E_0(x, h)$  in the  $z = h$  plane, the profile of the reflected beam is determined by the expression

$$E_h(x, z) = \int E_0(v + H \sin\psi) r(v + H \sin\psi) \\ \times \exp[iv x + i\sqrt{\kappa^2 - v^2} z] dv, \quad (4)$$

where

$$E_0(k) = \frac{1}{2\pi} \int E_0(x, h) \exp(-ikx + i\sqrt{\kappa^2 - k^2} h) dx.$$

In the quasi-optics approximation, the linear dimension of the reflected beam in the case of symmetric Bragg reflection depends on the distance  $z$  as

$$a(z) = \sqrt{\left( a_0^2 + \frac{1}{a_0^2} \right) \left( \frac{z}{\kappa \sin\theta_0} - \frac{\partial^2 \Phi}{\partial k^2} - \frac{\partial^2 \Phi_0}{\partial k} \right)^2}, \quad (5)$$

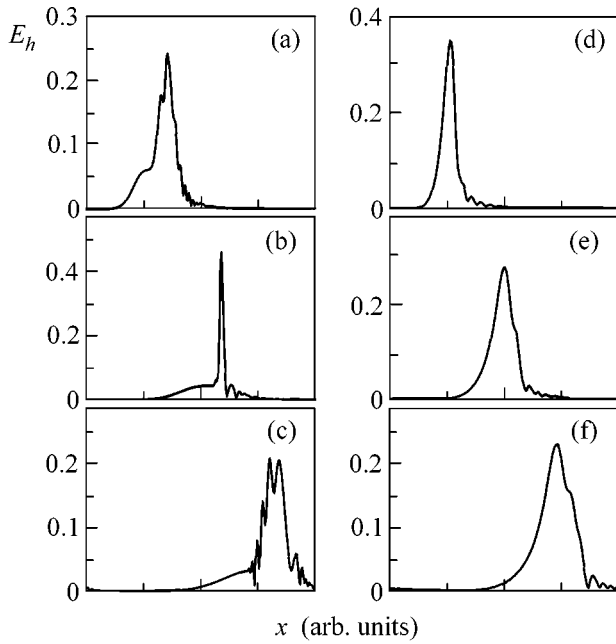


**Fig. 3.** Spatial profiles of reflected beam in the  $z =$  (a, d)  $h/2$ , (b, e)  $h$ , and (c, f)  $3h/2$  planes for the (a, b, c) strained and (d, e, f) ideal crystals.

where  $\varphi$  is the reflectivity phase  $\{r(k) = |r(k)|\exp[i\varphi(k)]\}$  and  $\varphi_0(k)$  is the phase of the Fourier transform spectrum of the incident beam at the crystal surface ( $z = 0$ ). For example, in the case of a Gaussian incident beam,  $E_0(x, z = h) = E_0 \exp[-x^2/2a^2 + ik_0x]$ , one has  $\partial^2\varphi_0/\partial k^2 = h/\kappa \sin\theta_0$ . Consequently, if  $\partial^2\varphi/\partial k^2 > 0$ , then the reflected beam will be focused in the  $z = z_0(\partial^2\varphi(k_0)/\partial k^2)\kappa \sin\theta_0 - h$  plane. For the reflection from the ideal semi-infinite crystal,  $\partial^2\varphi/\partial k^2 = -2(\sin\theta_B/\kappa \sqrt{\chi_{\bar{h}}\chi_h})^2$ , and, hence, beam focusing will not occur. For the strained crystal, the reflectivity phase oscillates widely. The oscillation period is inversely proportional to the thickness of a deformed layer and depends on the form of  $\mathbf{u}(z)$ . Consequently, by varying parameters of the deformed layer, one can easily create focusing conditions.

The profiles of the reflected beam, calculated numerically using Eqs. (1)–(4), are presented in Fig. 2. Figure 2a shows the spatial profile of the incident beam in the  $z = h$  (curve 1) and  $z = 0$  (curve 2) planes. One can see that, on the way from the beam-forming slit to the crystal surface, the incident beam undergoes strong diffraction spreading. Figures 2b and 2c show the profiles of the reflected beam in the  $z = h$  (curves 1) and  $z = 0$  (curves 2) planes for the angles of incidence  $(\theta_0 - \theta_B)/\text{Re}(\chi_0)$  equal to  $+7$  (b) and  $-1$  (c). One can see from these figures that, whereas for an angle of incidence  $\theta_0 = \theta_B + 7\text{Re}(\chi_0)$  (indicated by arrow 1 in Fig. 1) the wave is focused in the  $z = h$  plane, the wave reflected from the crystal undergoes diffraction spreading for  $\theta_0 = \theta_B - \text{Re}(\chi_0)$  (arrow 2 in Fig. 1). The dynamics of spatial focusing

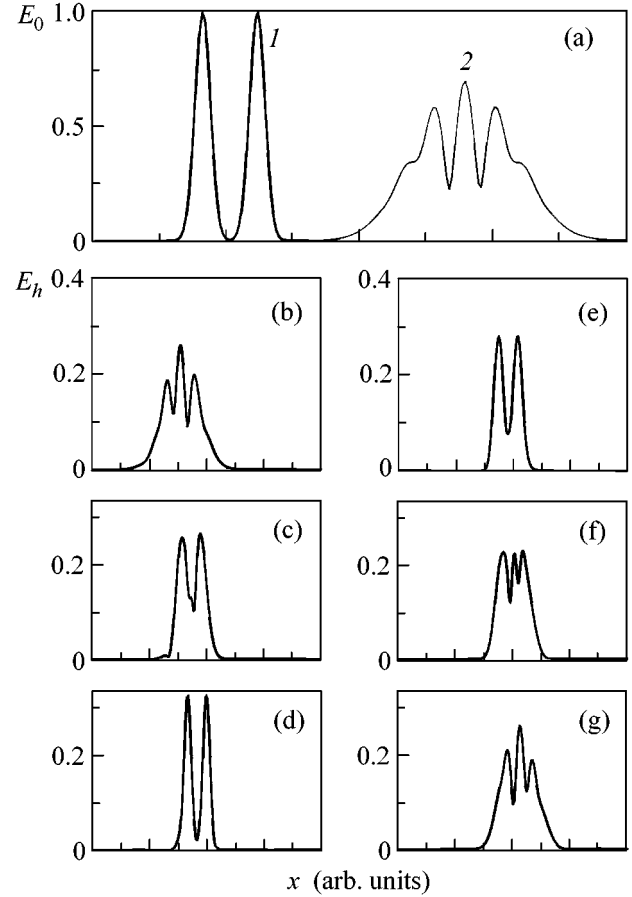


**Fig. 4.** Spatial profiles of (a) incident and (b–g) reflected beams. Incident beam in the (1)  $z = h$  and (2)  $z = 0$  planes. Profiles of reflected beam in the  $z =$  (b) 0, (c)  $0.25h_1$ , (d)  $0.4h_1$ , (e)  $0.5h_1$ , (f)  $0.6h_1$ , and (g)  $0.75h_1$  planes.

and diffraction spreading of the reflected wave is illustrated in Fig. 3. The curves in Figs. 3a–3c demonstrate the spatial profiles in the  $z = h/2$  (a),  $h$  (b), and  $3h/2$  (c) planes for a beam reflected from the strained crystal and the angle of incidence  $\theta_0 = \theta_B + 7\text{Re}(\chi_0)$ . The curves in Figs. 3d–3f show the spatial profiles in the same planes  $z = h/2$  (d),  $h$  (e), and  $3h/2$  (f) for a beam reflected from an ideal crystal and the angle of incidence  $\theta_0 = \theta_B + 3\text{Re}(\chi_0)$ . One can see that the wave reflected from the ideal crystal undergoes diffraction broadening as it moves away from the crystal. The wave reflected from the strained crystal is focused in the plane  $z = h$ , where the beam-forming slit is situated.

**4.** The strained crystals exhibit focusing properties in the asymmetrical reflection geometry as well. The results of numerical solution of Eqs. (1)–(4) for the reflection of the  $\text{CuK}\alpha$  radiation from the (111) planes of a strained germanium crystal with  $l = 8.5 \mu\text{m}$  and  $\Delta d/d = 1.2 \times 10^{-2}$  are presented in Fig. 4. The angle between the (111) planes and entrance face of the crystal was  $\psi = 9^\circ$ . The incident beam was formed by two

0.55- $\mu\text{m}$ -wide slits placed 2.7  $\mu\text{m}$  apart at a distance of 2.75 cm from the reflection region. The angle of incidence was  $\theta_0 = \theta_B + 15 \text{Re}(\chi_0)$ . Figure 4a shows the spatial profiles of the incident beam in the  $z = h$  (curve 1) and  $z = 0$  (curve 2) planes. One can see from this figure that the profile undergoes qualitative changes due to the diffraction on the way from the slit to the crystal surface. It is seen from the results of the preceding Section that in the case of asymmetrical reflection the Gaussian beam is focused in the  $z = h_1 = h \sin(\theta_0 + \psi) / \sin(\theta_0 - \psi)$  plane. However, it follows from Eqs. (4) and (5) that the focusing length depends on the spatial profile of the incident beam. The spatial profiles of the reflected beam at different distances from the crystal,  $z = 0$  (b),  $0.25h_1$  (c),  $0.4h_1$  (d),  $0.5h_1$  (e),  $0.6h_1$  (f), and  $0.75h_1$  (g), are shown in Fig. 4. One can see from this figure that the profile of the incident beam is completely restored at  $z = 0.4h_1$ . Taking into account the reflection asymmetry, we have an  $n$ -fold enlarged image of an object in this plane, where  $n = \sin(\theta_0 + \psi) / \sin(\theta_0 - \psi)$ .

5. The above analysis demonstrates that focusing optical systems can be fabricated from crystals or multilayer periodic structures with variable period. The ease of fabrication of these systems may be beneficial for their wide use in X-ray and ultraviolet microscopy

and astronomy, as well as in the design of new constructions for microprobes and high-power sources. These systems may also find use in the compression of femtosecond laser pulses.

This work was supported in part by the Russian Foundation for Basic Research (project no. 99-02-16093) and the program "Russian Universities."

#### REFERENCES

1. V. V. Aristov and A. I. Erko, *X-ray Optics* (Nauka, Moscow, 1991).
2. A. Snigirev, V. Kohn, I. Snigireva, and B. Lengler, *Nature* **384**, 49 (1996).
3. M. A. Kumakhov, *Proc. SPIE* **4155**, 2 (2000).
4. A. V. Andreev, V. E. Asadchikov, B. V. Mchedlishvili, *et al.*, *Pis'ma Zh. Éksp. Teor. Fiz.* **73**, 205 (2001) [*JETP Lett.* **73**, 184 (2001)].
5. A. V. Andreev, A. V. Balakin, D. Boucher, *et al.*, *Pis'ma Zh. Éksp. Teor. Fiz.* **71**, 539 (2000) [*JETP Lett.* **71**, 370 (2000)].
6. Z. G. Pinsker, *X-ray Crystal Optics* (Nauka, Moscow, 1982).

*Translated by V. Sakun*